AD-A014 142

NUMERICAL ANALYSIS OF PROJECTILE IMPACT AND DEEP PENETRATION INTO EARTH MEDIA

M. H. Wagner, et al

California Research and Technology, Incorporated

Prepared for:

Defense Nuclear Agency
Army Engineer Waterways Experiment Station

August 1975

DISTRIBUTED BY:

NTIS
National Technical Information Service
U. S. DEPARTMENT OF COMMERCE

ISCLAIMER NOTICE

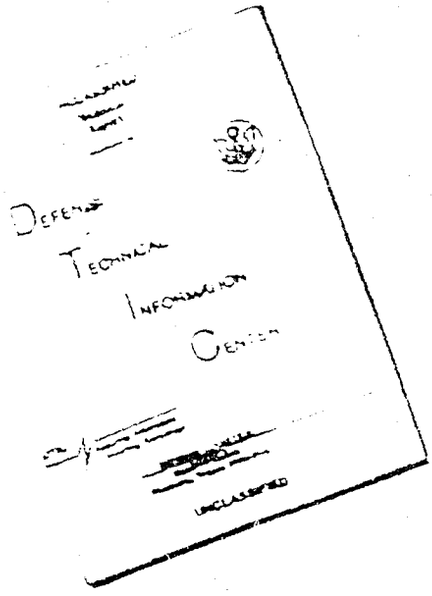

THIS DOCUMENT IS BEST QUALITY AVAILABLE. THE COPY FURNISHED TO DTIC CONTAINED A SIGNIFICANT NUMBER OF PAGES WHICH DO NOT REPRODUCE LEGIBLY.

REPRODUCED FROM
BEST AVAILABLE COPY

252067

Reproduced by
NATIONAL TECHNICAL
INFORMATION SERVICE
Springfield Va 22151

Unclassified

SECURITY CLASSIFICATION OF THIS PAGE (When Data Entered)

REPORT DOCUMENTATION PAGE

READ INSTRUCTIONS BEFORE COMPLETING FORM

1. REPORT NUMBER: Contract Report S-75-4
2. GOVT ACCESSION NO.:
3. RECIPIENT'S CATALOG NUMBER: ADA010 102

4. TITLE (and Subtitle): NUMERICAL ANALYSIS OF PROJECTILE IMPACT AND DEEP PENETRATION INTO EARTH MEDIA

5. TYPE OF REPORT & PERIOD COVERED: Final Report, 1 Dec 1973/30 Nov 1974

6. PERFORMING ORG. REPORT NUMBER: CRT 2630-1

7. AUTHOR(s): M. H. Wagner, R. N. Arenemnieen, W. [illegible]

8. CONTRACT OR GRANT NUMBER(s): DAAG39-74-C-0007

9. PERFORMING ORGANIZATION NAME AND ADDRESS: California Research & Technology, Inc., 6269 Variel Avenue, Suite [illegible], Woodland Hills, California 91364

10. PROGRAM ELEMENT, PROJECT, TASK AREA & WORK UNIT NUMBERS: [illegible] 5B263, Work Unit 15

11. CONTROLLING OFFICE NAME AND ADDRESS: Defense Nuclear Agency, Washington, D. C. 20305

12. REPORT DATE: August 197[illegible]

13. NUMBER OF PAGES:

14. MONITORING AGENCY NAME & ADDRESS (if different from Controlling Office): U. S. Army Engineer Waterways Experiment Station, Soils and Pavement Laboratory, P. O. Box 631, Vicksburg, Miss. 39180

15. SECURITY CLASS. (of this report): Unclassified

15a. DECLASSIFICATION/DOWNGRADING SCHEDULE:

16. DISTRIBUTION STATEMENT (of this Report): Approved for public release; distribution unlimited.

17. DISTRIBUTION STATEMENT (of the abstract entered in Block 20, if different from Report):

18. SUPPLEMENTARY NOTES:

DDC
RECEIVED
AUG 26 1975
B

19. KEY WORDS (Continue on reverse side if necessary and identify by block number):
Penetration
Terradynamics
Finite-difference code
Soil mechanics

20. ABSTRACT (Continue on reverse side if necessary and identify by block number):

A study was carried out to examine the utility, and some of the limitations, of using a finite-difference Lagrangian code to analyze relatively deep penetrations of projectiles into earth media. Numerical solutions were obtained for the normal impact of an 8-in. dia, [illegible]-lb steel ogival projectile at 2000 fps into a soil/shale layered target. Two types of analyses were performed. In the first, the soil response, penetration

DD FORM 1 JAN 73 1473 EDITION OF 1 NOV 65 IS OBSOLETE

Unclassified

SECURITY CLASSIFICATION OF THIS PAGE (When Data Entered)

dynamics, and projectile response were analyzed as one problem. The projectile was treated as an elastic-plastic, or deformable body, in order to determine the internal stress response. This computation was carried out for just the initial phase of penetration, until the nose was fully embedded in the soil. Problems were encountered with large numerical oscillations in the forces applied to the projectile due to the strongly hysteretic soil model and to severe distortion of computational cells in the fireball. These problems can be overcome, but this type of calculation would still be cumbersome and time consuming, due to the markedly different nature of the projectile response (primarily small, elastic strain) and of the soil response (severe plastic flow).

A more practical approach is to separately analyze the penetration dynamics and the projectile response. This can be done by first calculating the penetration of the projectile treated as a non deforming rigid body, thus determining the history of projectile acceleration, velocity, and depth, as well as the spatial and temporal distribution of forces acting on the body. These force distributions can then be used as boundary conditions in a separate analysis of the internal stress loads of the projectile.

In the second analysis, the projectile was treated as a rigid body, and its penetration to a depth of 22 ft was calculated. The average deceleration was 300 g's in the soil and 110 g's in the shale. The final velocity was 1984 fps. This is a more efficient approach, but it will still be very time consuming to calculate an entire penetration event in this manner. Fortunately, because of the quasi-steady state nature of penetration processes within a nominally homogeneous geologic layer, it is not necessary to calculate the entire penetration. The penetration dynamics and critical force loading conditions on the projectile can be determined with reasonable accuracy by analyzing just the initial embedment and those periods where the projectile is entering different geologic layers.

PREFACE

This report describes a research program to investigate the feasibility of the application of a two-dimensional finite-difference code for the prediction of projectile penetration into earth media. It was conducted for the U. S. Army Engineer Waterways Experiment Station (WES) by California Research and Technology, Inc. (CRT), under Contract DACA 39-74-C-0087. This program was sponsored by the Defense Nuclear Agency (DNA) under Subtask SB209, Work Unit 13, "Contract Support Studies of Ground Shock Propagation through Soils and Rock".

The principal investigator at CRT was M. H. Wagner. Technical advice and guidance were contributed by K. N. Kreyenhagen. W. S. Goerke performed the computer program coding and code development work. C. C. Turton and G. E. Eggum provided valuable assistance in formulation of the material models and data reduction, and in the computer production runs, respectively.

The penetrator specifications, site profile, and material properties were provided by WES.

The Contracting Officer's Representative was D. K. Butler of WES. The contract was monitored and coordinated with the overall DNA penetration program under DNA Subtask SB211, Work Unit 03, "Contract Support Studies of Projectile Penetration and Impact". A. J. Breithaupt was the Contracting Officer and Col. G. H. Hilt was the Director of WES during this contract investigation.

TABLE OF CONTENTS

		Page
SECTION I	INTRODUCTION AND SUMMARY	1
1.1	[illegible]	1
1.2	[illegible]	2
1.3	[illegible]	3
SECTION II	PROBLEM DESCRIPTION	6
2.1	[illegible]	6
2.2	[illegible]	6
SECTION III	COMPUTATIONAL METHOD	14
3.1	[illegible]	14
[illegible]	[illegible]	14
[illegible]	[illegible]	15
SECTION IV	PENETRATION OF ELASTIC-PLASTIC [illegible]	18
4.1	[illegible]	18
4.2	[illegible] Station Results	20
SECTION V	[illegible] SOLUTION	33
5.1	[illegible]	34
5.2	[illegible] Results	36
SECTION VI	COMPARISON OF DEFORMABLE-BODY [illegible]	53
SECTION VII	CONCLUSIONS AND RECOMMENDATIONS	62
7.1	[illegible]	62
7.2	[illegible]	63
7.3	[illegible]	64
REFERENCES		66
APPENDIX A	MATERIAL MODELS	67
APPENDIX B	DISPLACEMENT, VELOCITY, AND PRINCIPAL STRESS CONTOUR PLOTS — DEFORMABLE-BODY CASES	82
APPENDIX C	DISPLACEMENT, VELOCITY, AND PRINCIPAL STRESS CONTOUR PLOTS — RIGID-BODY CASES	105

Preceding page blank

SECTION 1

INTRODUCTION AND SUMMARY

1.1 BACKGROUND AND OBJECTIVES

A number of analytical and semi-empirical relationships have evolved over the years to predict projectile penetration into earth media. These can provide useful information about certain aspects of penetration, but in general, they are restricted in their applicability (relative to types of target media and the basic properties of such media), and they yield incomplete information about the forces acting on the projectile, and about the distribution of stresses within the projectile.

Finite-difference numerical methods have the potential for overcoming the limitations of purely analytical or semi-empirical approaches for the following reasons:

a. The dynamic mechanisms of target response and of projectile target interactions can be explicitly incorporated into the analysis.

b. The basic properties of target media (at actual or representative sites) can be incorporated into the analysis.

c. The analysis can yield time histories of (1) the force distribution applied to the projectile surface and the consequent projectile deceleration, velocity, and position, and (2) the stress distribution and deformations within the projectile and its internal components.

In the related area of armor penetration, finite-difference numerical techniques have been used, beginning in

1967, for analysis of penetration dynamics and interactions between shape factors, material properties, and impact parameters (e.g., Refs. 1 and 2). Thigpen[1] made the first application of these techniques to earth penetration analyses. Despite fairly gross [illegible] of both the projectile and target media, he was able to obtain penetration depths into tuff and limestone which were in reasonable agreement with experimental results. However, serious practical problems were evident, particularly with respect to the computer times required for solutions with adequate zoning to resolve stress gradients, deformation, and failure processes in the target medium, and to [illegible] realistic, non-solid, projectile designs.

The objectives of the current research have been to expose and explore some of the practical problems in applying 2-D finite-difference solutions to a broad class of earth penetration problems, and to examine the utility of this general approach by means of demonstration problems.

This work, which was primarily carried out during the first half of 1974, established some of the foundation for the subsequent penetration and projectile response analyses which are described in Refs. 4 and 5. To our knowledge, for example, the approach of treating the projectile as a rigid body in the numerical analysis of earth penetration dynamics was first utilized during this program. This is an efficient technique which makes it possible to first analyze the severe target distortion associated with penetration by the projectile, and then, if desired, to separately analyze the response of the projectile itself.

1.2 APPROACH

A representative but hypothetical earth penetration problem was chosen for analysis. It consisted of the normal incidence impact of an 8 in. dia, 602 lb steel ogival projectile at 2000 fps into a fairly soft target consisting of soil over shale.

An existing two dimensional finite difference Lagrangian code, WAVE-L, was used as the basic numerical technique. WAVE-L is based on the Hemp method.[1]

Two types of analyses of the projectile penetration were performed. In the first, the projectile was treated as an elastic-plastic, or deformable body. The stress response of the projectile and the deformation of the target medium during penetration were computed as a single, unified problem. This solution was carried out for the initial phase of penetration: i.e., until the projectile nose was fully embedded into the earth.

In the second analysis, the soil response and consequent forces acting on the projectile were computed as before using the regular elastic-plastic formulation of the WAVE-L code, but the projectile itself was assumed to be a rigid body. In typical earth penetration problems of interest, the projectile suffers only elastic strains, and these would not be expected to significantly interact with the severely-distorting target media or with the penetration processes. For purposes of analyzing the penetration dynamics and the forces applied to the projectile surface, it is therefore reasonable to assume that the projectile is a rigid body. This approach bypasses the detailed computation of the internal projectile response, thereby allowing a more rapid and efficient calculation of the penetration. This rigid body solution covered penetration through the soil layer and into the sahle, to a total depth of 22 ft.

1.5 SUMMARY OF RESULTS

Analysis of the penetration of the elastic plastic, or deformable-body projectile was carried out for 0.8 msec, or to a depth of 20 inches into the soil layer. The nominal cell size in the target for this solution was 1 x 1 inch. After penetrating about 6 inches, the average deceleration reached about 555 g's. This level persisted for the balance of the solution, indicating that interactions between the target soil and the first few inches of the nose tip essentially determined the penetration dynamics. The maximum stresses in the steel projectile occurred near the nosetip, which experienced about 5.5 kb, and in the connecting section between the nose and the body of the projectile, which experienced nearly 4 kb.

Large oscillations occurred in the force history applied to the deformable projectile due apparently to amplifying, synchronous interactions between the finite nature of the computational grid and the strongly hysteretic load-unload behavior given by the soil model. (A method for alleviating this problem was found during the rigid-body solution.) Despite this oscillation problem, the deformable-body penetration solution demonstrates the feasibility of obtaining a unified solution of projectile penetration and projectile response. However, this is a cumbersome and time-consuming approach. A more practical approach is to analyze the penetration dynamics and projectile response as separate problems. From an analysis of the penetration of a rigid projectile, the surface loading on the projectile surface can first be determined. This loading can then be used as a boundary condition for analysis of the response of the elastic-plastic projectile itself. This approach has been used in Ref. 5.

The rigid body penetration solution was carried out for 11.5 msec. During this time, the projectile penetrated

through 16 2/3 ft of soil and about 5 ft of shale. The nominal cell size in the target was 2 x 2 inches. The average deceleration level was about 390 g's in the soil and 440 g's in the shale. The discrepancy between decelerations in the soil layer from the deformable-body and rigid-body penetration solutions was probably due to the coarser zoning in the rigid-body case.

Large oscillations in the force history applied to the projectile also occurred in the rigid-body solution, but it was found that these were substantially alleviated by using a geometrically "predeformed" grid in the soil ahead of the projectile. This technique eliminated synchronous interactions and reduced the distortion of cells sliding out and around the nose tip. In strongly hysteretic target media, considerable care needs to be taken to realistically model the unloading and reloading behavior.

The rigid-body penetration solution demonstrates that finite-difference code solutions of deep penetrations are possible, although the cost for analyzing the complete penetrations of a high-velocity projectile into a soft earth target is likely to be high. Fortunately, it is not necessary to analyze the complete penetration in order to determine critical design conditions. In deep penetrations, the target response and penetration processes generally change only gradually with increasing depth within a homogeneous geologic layer. Under these circumstances, the penetration dynamics and the critical conditions of force loading on a projectile can be determined with reasonable accuracy by analyzing just the initial nose embedment period and the periods where the projectile nose is entering different geologic layers. This approach has been used in Reference 4.

SECTION II

PROBLEM DESCRIPTION

The conditions for the penetration solutions are summarized in Figure 1.

2.1 PENETRATOR

The projectile is shown in detail in Figure 2. It consists of a hollow cylindrical shell behind an ogival nose section. The projectile cavity contains a 293-lb steel ballast mass which is connected to the outer shell by concentric rings. The total weight is 602 lb, and the weight area (W/A) ratio is 12 psi.

For the deformable-body calculation, the steel projectile was treated as an elastic perfectly plastic material having the properties listed in Table 1. The equation of state and other details of the model for steel are contained in Appendix A.

For the rigid body calculation, the only information required to characterize the projectile was the specification of the outer contour and the total weight.

2.2 SITE

The hypothetical target site profile consisted of a 16 2/3 ft-thick layer of soil over shale. Sets of property curves for these media were provided by Waterways Experiment Station (WES). These curves were fit by the hysteretic, elastic ideally plastic material models which are

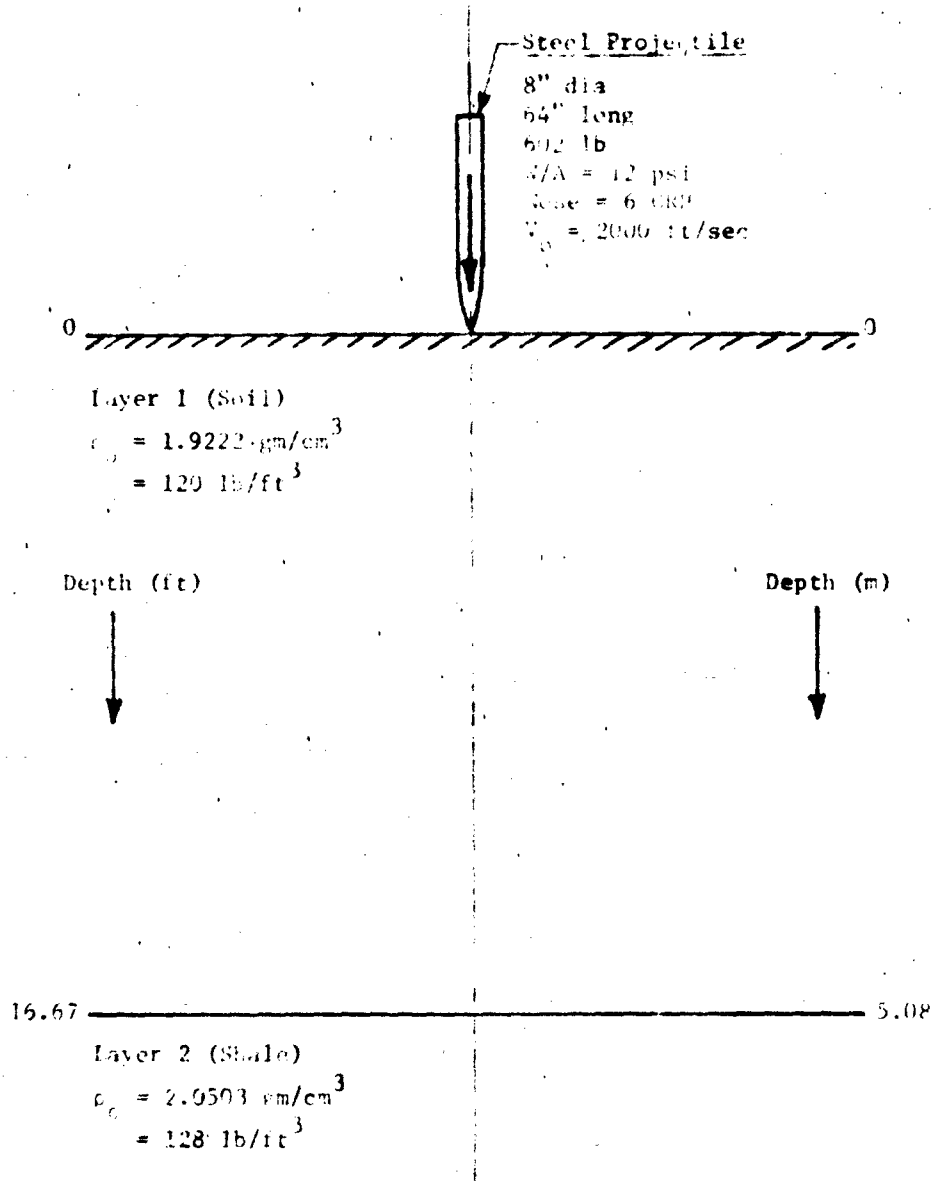

Figure 1. Overall Conditions for Numerical Solutions

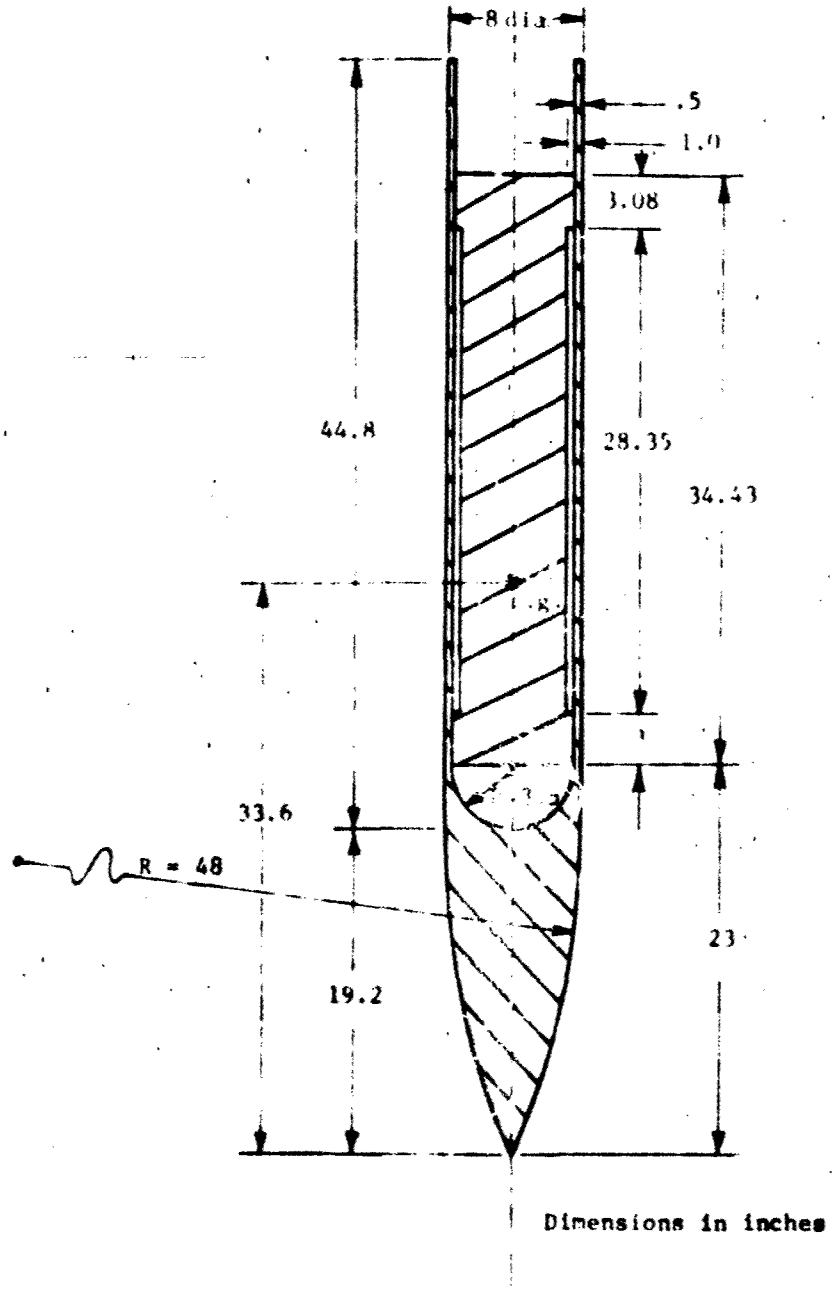

Figure 2. Penetrator Design

TABLE 1. SUMMARY OF MATERIAL PROPERTIES

	Projectile	Layer 1 0-16 2/3 ft	Layer 2 >16 2/3 ft
Material	Steel	Soil	Shale
Density, ρ_o, gm/cm^3	7.84	1.9222	2.0505
lb/ft^3	489	120	128
Initial values of:			
Bulk modulus, k_o, psi	2.345×10^7	4,237	83,180
Shear modulus, G_o, psi	1.204×10^7	2,542	20,000
Poisson's ratio, ν_o	.289	.25	.389
Dilatational wave velocity, c_o, fps	19,580	543	1,994
Unloading wave velocity from $\sigma_{z_{max}}$ = 15,000 psi, fps		6,656	6,846
Unconfined compressive strength, psi	50,000	59	564
Yield strength at P = 1000 psi, Y, psi	50,000	180	750

described in Appendix A. Figures 3 and 4 show show the uniaxial strain load-unload paths provided by WES, together with the fits given by the models.

The models are seen to follow the WES curves quite well, with the exception of the final portion of unloading in the strongly hysteretic Layer 1. Figure 5 shows the shear failure surfaces. (The upper plot gives the low pressure region in detail.)

Table 1 summarizes the site media properties.

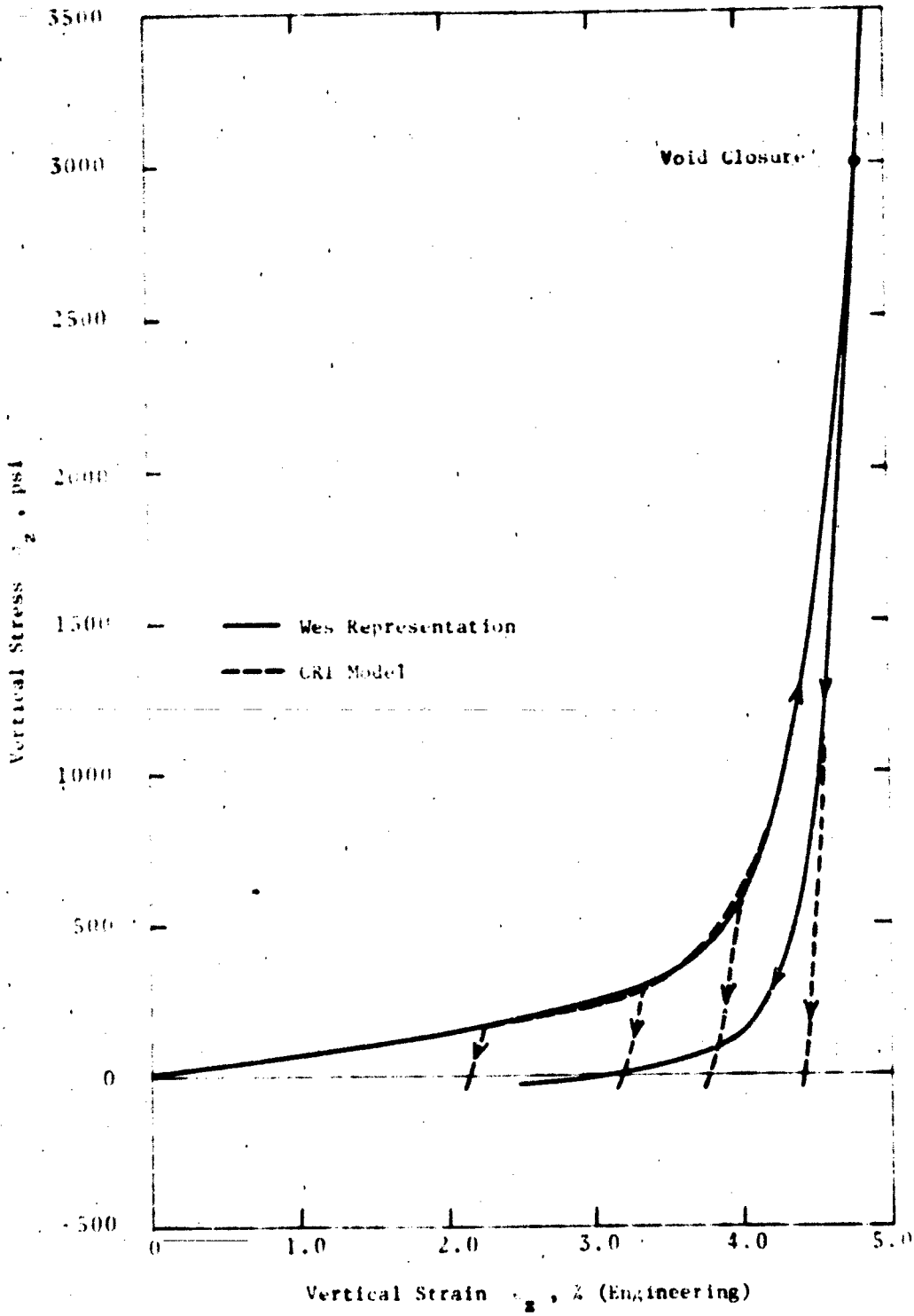

Figure 3. Uniaxial Strain Load-Unload Paths for Layer 1 (Soil)

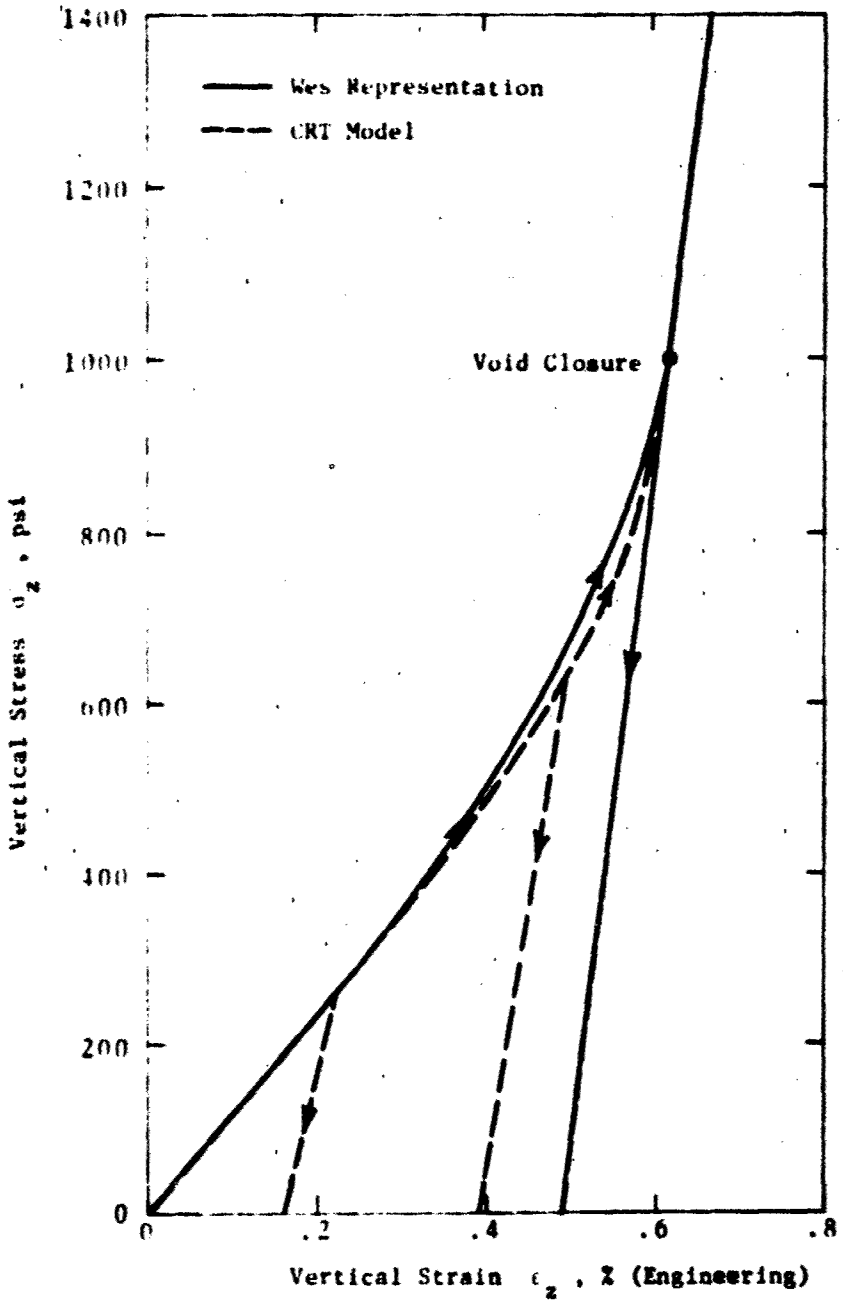

Figure 4. Uniaxial Strain Load-Unload Paths for Layer 2 (Shale)

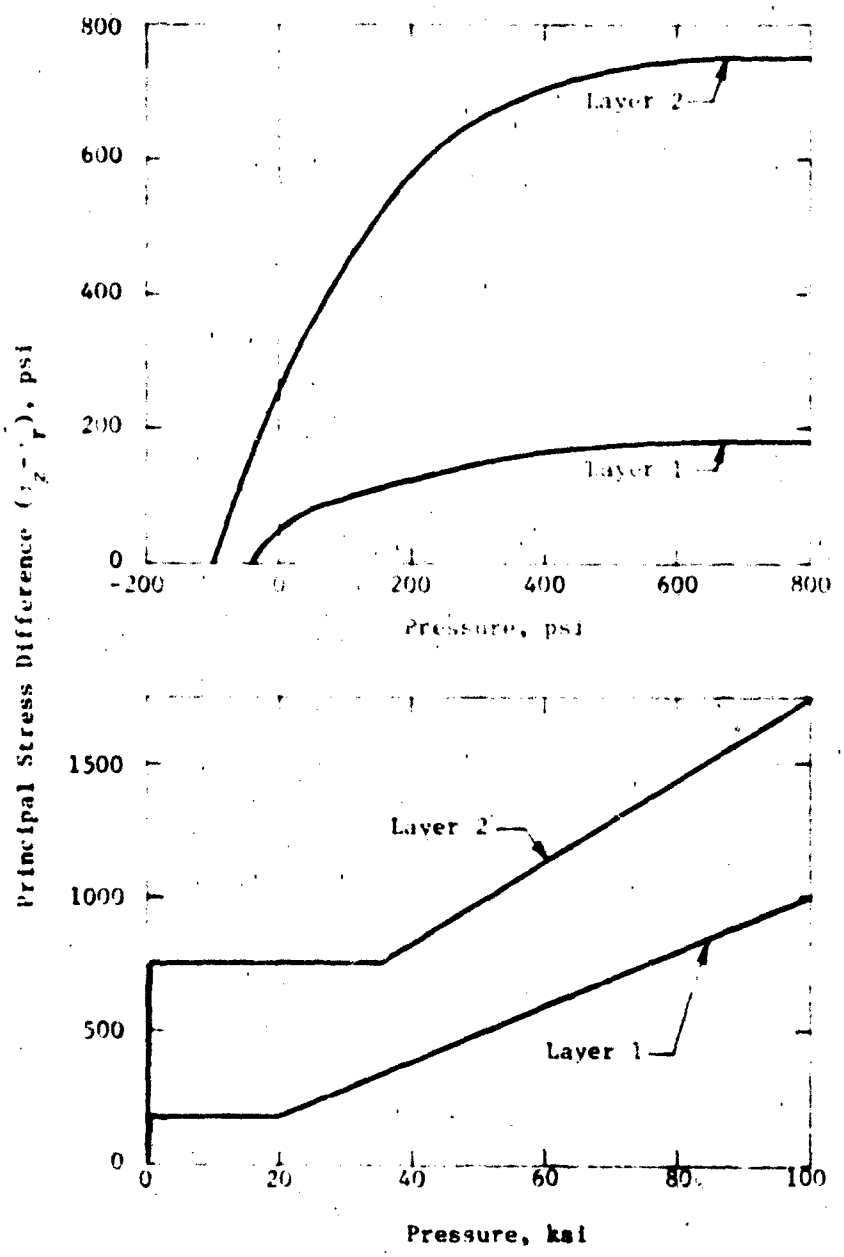

Figure 5. Shear Failure Surfaces for Layer 1 (Soil) and Layer 2 (Shale)

SECTION III

COMPUTATIONAL METHOD

3.1 WAVE-L CODE

The WAVE-L code was employed for these calculations. WAVE-L is a two-dimensional code which solves the equations of motion for elastic-plastic bodies by means of a finite-difference Lagrangian-cell technique. The mathematical formulation is basically the same as that described by Wilkins.[6] A sliding interface was used to allow penetration of the projectile through the computational grid. For these calculations, the projectile/target interface was assumed to be frictionless. A lithostatic field in the soil was generated by prescribing initially compressed soil states.

3.2 GRID DECOUPLING

The sliding interface formulation in WAVE-L includes the capability for dynamically decoupling or unlocking the grid points when a prescribed decoupling or failure criterion is met. In a penetration problem, decoupling permits the cells initially attached to the axis to flow around the advancing nose shape, sliding along the interface. In these calculations, decoupling occurred when either the generalized plastic strain, $\bar{\epsilon}^p$, in a cell adjacent to the axis, or the tensile stress, $-\sigma_n$, normal to the axis (slide line) exceeded critical values. Generalized plastic strain is defined[8] as

$$\bar{\epsilon}^p = \int \left(\frac{2}{3} de^p_{ij} de^p_{ij} \right)^{1/2}$$

and is a measure of the cumulative plastic deformation an element undergoes. $d\bar{\epsilon}^p$ is always ≥ 0, and thus $\bar{\epsilon}^p$ monotonically increases as any type of plastic strain is experienced.

The critical generalized plastic strain and tensile stress values used for Layer 1 and Layer 2 were:

	$\bar{\epsilon}^p_c$	σ_{n_c}
Layer 1 (soil)	.07	40 psi
Layer 2 (shale)	.013	120 psi

During high-velocity penetration, the soil flowing around the nose often separates from the projectile before reaching the tangency point of the nose and cylindrical body. In these calculations, separation of a point could occur when the stress normal to the projectile was no longer compressive; i.e., $\sigma_n < 0$. When this criterion is met, the point is moved as a free surface point and may subsequently collide with the penetrator, in which case it again becomes attached to the projectile. (Closing of the void would generally be expected during the final stages of deep penetration.)

3.3 COMPUTATION OF STRESSES ACTING ON PROJECTILE

The projectile contour is defined by a series of boundary points spaced along its periphery. (In an elastic-plastic, or deformable projectile, these boundary points are corners of the cells used to describe the projectile.) The projectile surface line constitutes a slide line,

Stresses are transmitted across the slide line in accordance with a friction rule. For both of the present calculations, the surface was assumed to be frictionless, so only normal stresses were transmitted across the slide line. The normal stress applied to each surface segment of the projectile is determined as follows: Referring to the example shown in the sketch below, the stress components in a direction normal to the projectile surface segment 2-3, are computed at the centroids a and b of the target cells which are in contact with the projectile surface segment. (In a Lagrangian code, stresses are cell-centered quantities.) By linear interpolation, the stress

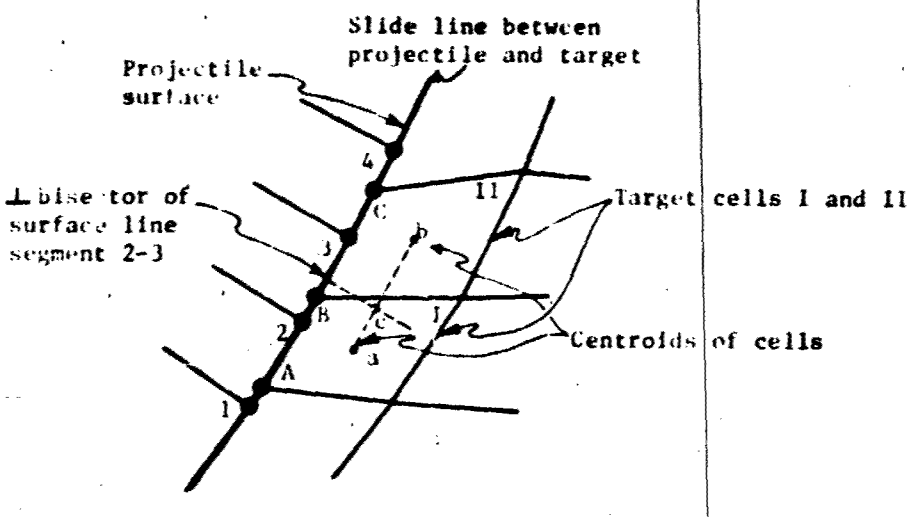

is determined at point c, which is the intersection of a-b with the perpendicular bisector of the projectile surface segment 2-3. The component of stress at c which is normal to 2-3 is then applied all along 2-3.

An alternative method would be to apply to projectile surface segment 2-3 the stress calculated for cell I over segment 2-B and the stress for cell II over segment B-3. This method becomes more inaccurate, however, when the target cells become severly distorted.

SECTION IV

PENETRATION OF ELASTIC PLASTIC (DEFORMABLE) PROJECTILE

In this solution, the penetration processes in the target soil and the response of the projectile were simultaneously analyzed for the interval from impact until the nose was fully embedded.

4.1 GRID DESIGN

The computational grid for analyzing the elastic-plastic, or deformable-body penetration is shown in Figure 6. (The plot shows a complete cross-section of the axisymmetric problem. The actual grid contained only cells on one side of the axis.) The nominal zone size of the projectile was .5 inch in the radial direction (i.e., 8 cells across the radius) and 1.0 inch in the vertical direction. In the body of the projectile, the vertical zone dimension was gradually increased to a maximum of 1.7 in. at the rear of the projectile. There were about 300 cells in the projectile.

In the target medium, uniform 1 x 1 in. cells were used out to 16 in. radius, and down to 20-in. depth. Beyond this region, the radial and vertical cell dimensions gradually increased in a 2% geometric series. The overall grid extended to 26-in. radius and 38-in. depth, using about 900 cells for the target. (Because of the high compressibility and low wave velocity in soil Layer 1, the presence of the boundaries was not felt by the projectile during the 0.8-msec duration of this calculation.)

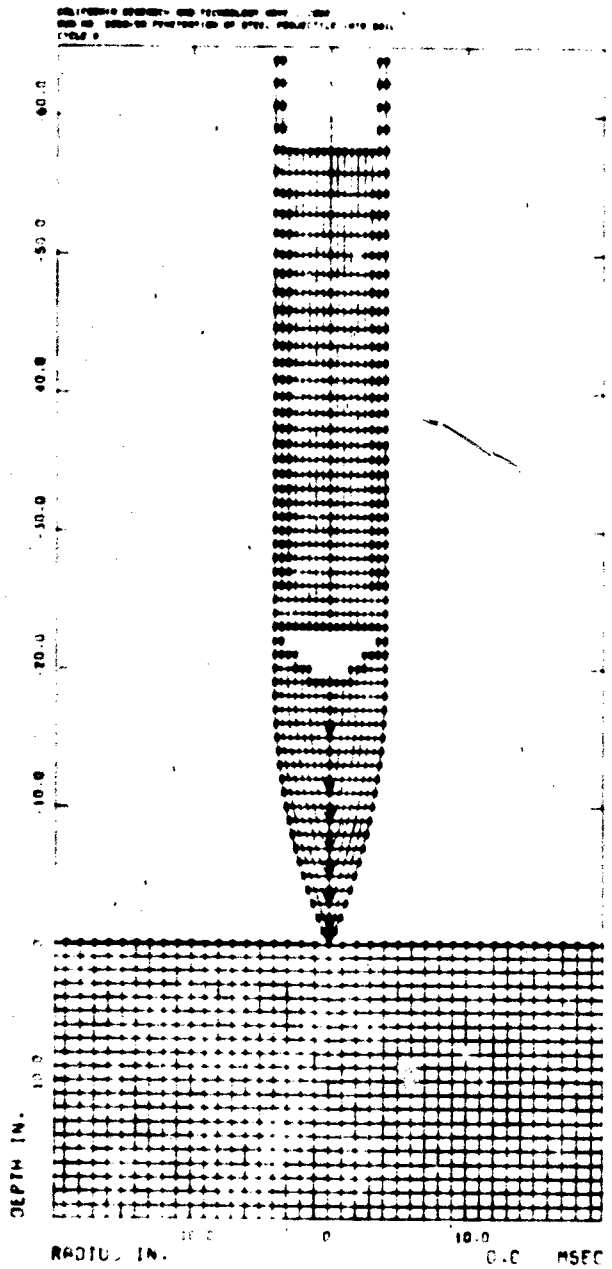

Figure 6. Initial Grid Configuration for Deformable Body Solution

The K-line running along the penetrator contour and along the axis of the target was specified as a slide line. As the penetrator impinges into the target, this dual line defines the penetrator soil interface and allows slippage and/or separation to occur.

The lattice points along the axis were initially coupled, and the projectile tip and the corresponding soil point were locked together. Thus, before the soil point at the surface could move out along the projectile nose surface, it had to decouple by having the associated soil cell fail according to the decoupling criterion described in Section III. Furthermore, since the points were initially locked together, the initial velocity of the soil point was equal to the projectile velocity. This produced an unrealistically high initial stress near the impact point. While the high stress decayed rapidly and probably did not significantly affect the overall solution, it was subsequently decided that it would be more realistic to have the nose and soil point at the origin initially decoupled and to assign zero initial velocity to the soil point. This procedure was used in the rigid-body penetration solution described in Section V.

4.2 DEFORMABLE PROJECTILE SOLUTION RESULTS

The deformable-projectile penetration solution was carried out until the nose was completely buried, with the tip at about 20 inches depth. This took 0.837 msec. The computational grid, particle velocity field, and principal stress field at this time are shown in Figures 7 to 9.

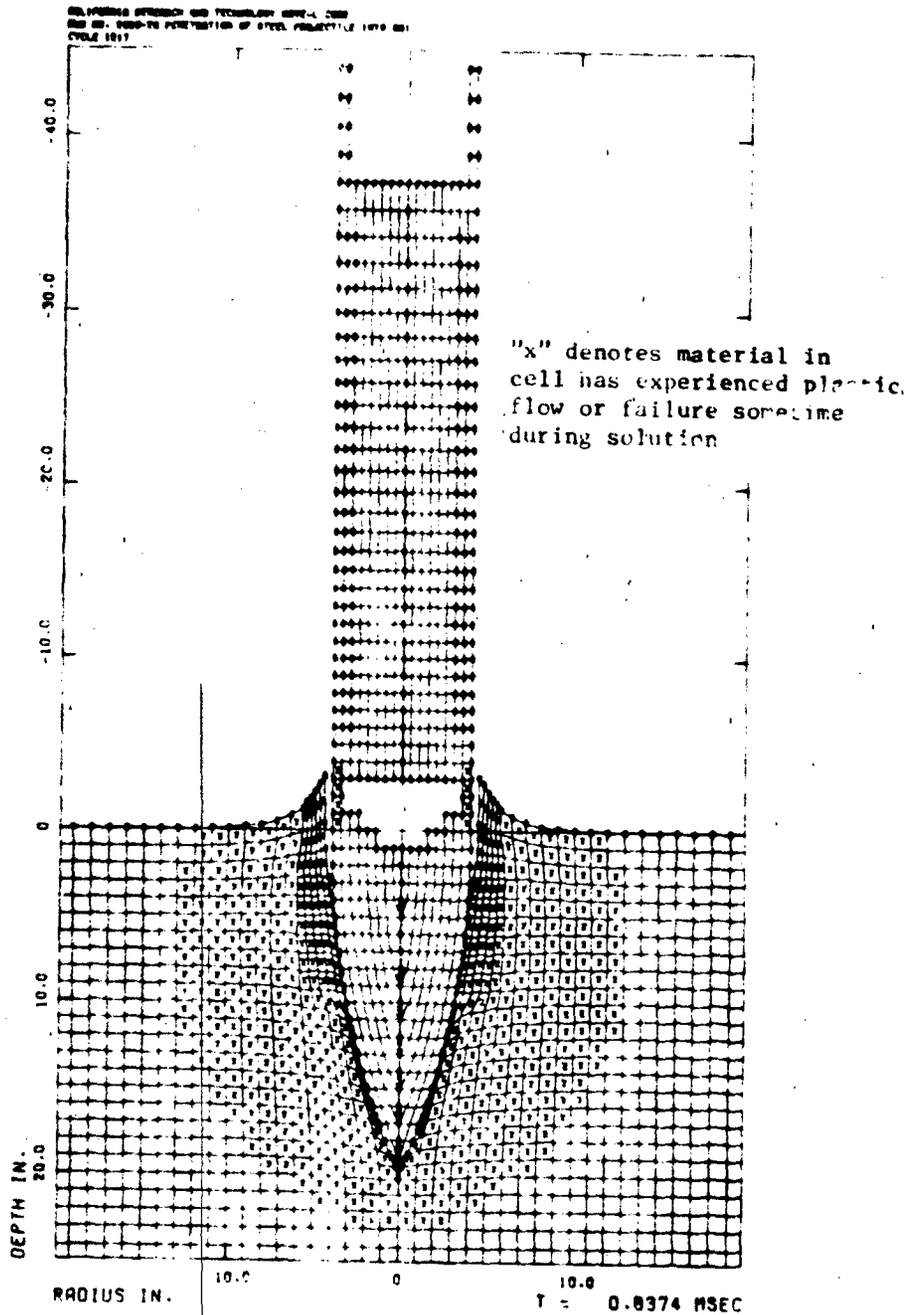

Figure 7. Grid Configuration at End of Deformable-Body Solution, Projectile Nose at 20 in. Depth

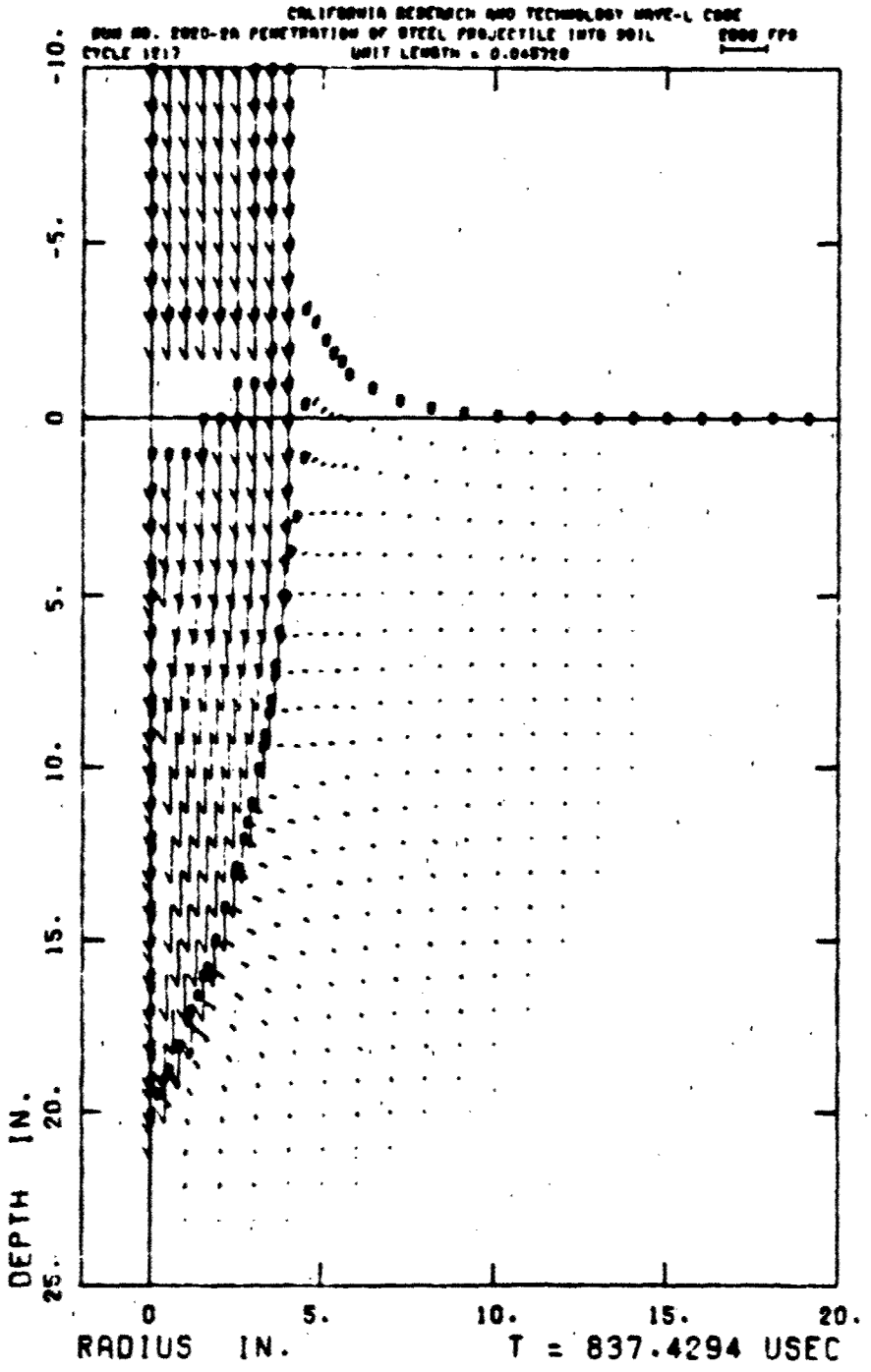

Figure 8. Particle Velocity Field at End of Deformable-Body Solution, Projectile Nose at 20 in. Depth

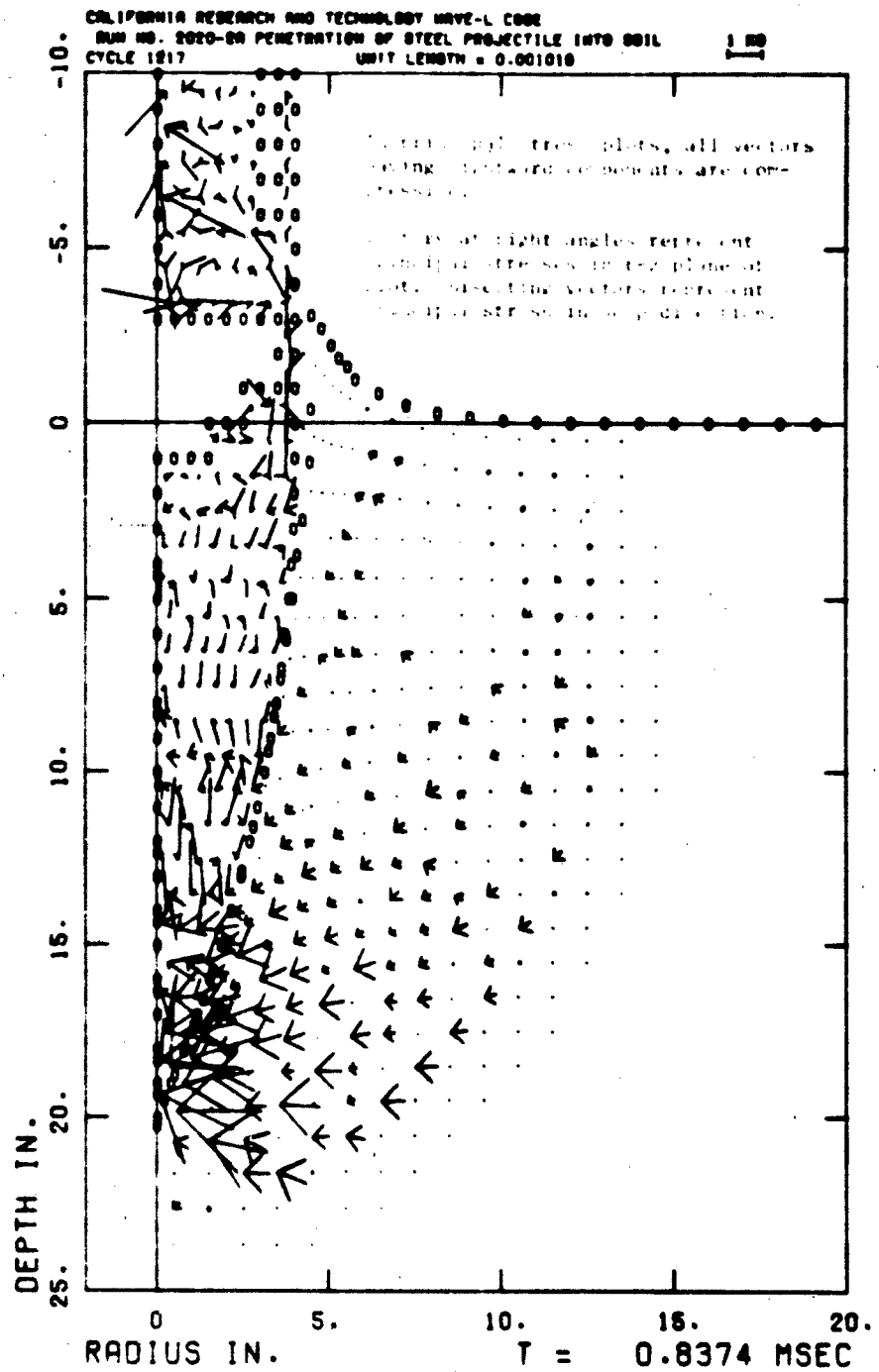

Figure 9. Principal Stress Field at End of Deformable-Body Solution, Projectile Nose at 20 in. Depth

In the Lagrangian grid (Figure 7), the symbol "x" in a cell indicates that material in that cell has experienced plastic flow or failure at some time during the solution. A volume of the soil extending outward to about 3 projectile radii and ahead of the nose tip about 1 radius has failed. The projectile response was entirely elastic, except for slight plastic deformation ($\bar{\epsilon}^p \simeq .35\%$) in the thin annular section connecting the nose with the body.

A series of the field plots obtained from this solution as the projectile entered the soil is given in Appendix B.

The dynamics of the overall projectile are summarized in Figures 10 to 12, which show time histories of the total axial force applied to the projectile, and resulting average deceleration and velocity, and depth of penetration. After about .3 msec, corresponding to 6 inches of penetration, the average acceleration level had reached about 585 g's. This level persisted until the end of the solution, despite the fact that separation between the soil and projectile surface did not occur until about .56 msec when the nose tip was at about 11 inches depth. This indicates that axial forces applied by the soil to the first 6 inches of the nose tip were of predominate importance to the projectile dynamics of the problem.

The large oscillations which are apparent in the force and acceleration histories in Figure 10 are due to interactions between the finite nature of the computational zoning and the strongly hysteretic character of the unloading model used to describe the Layer 1 soil. This problem will be discussed further in connection with the rigid-

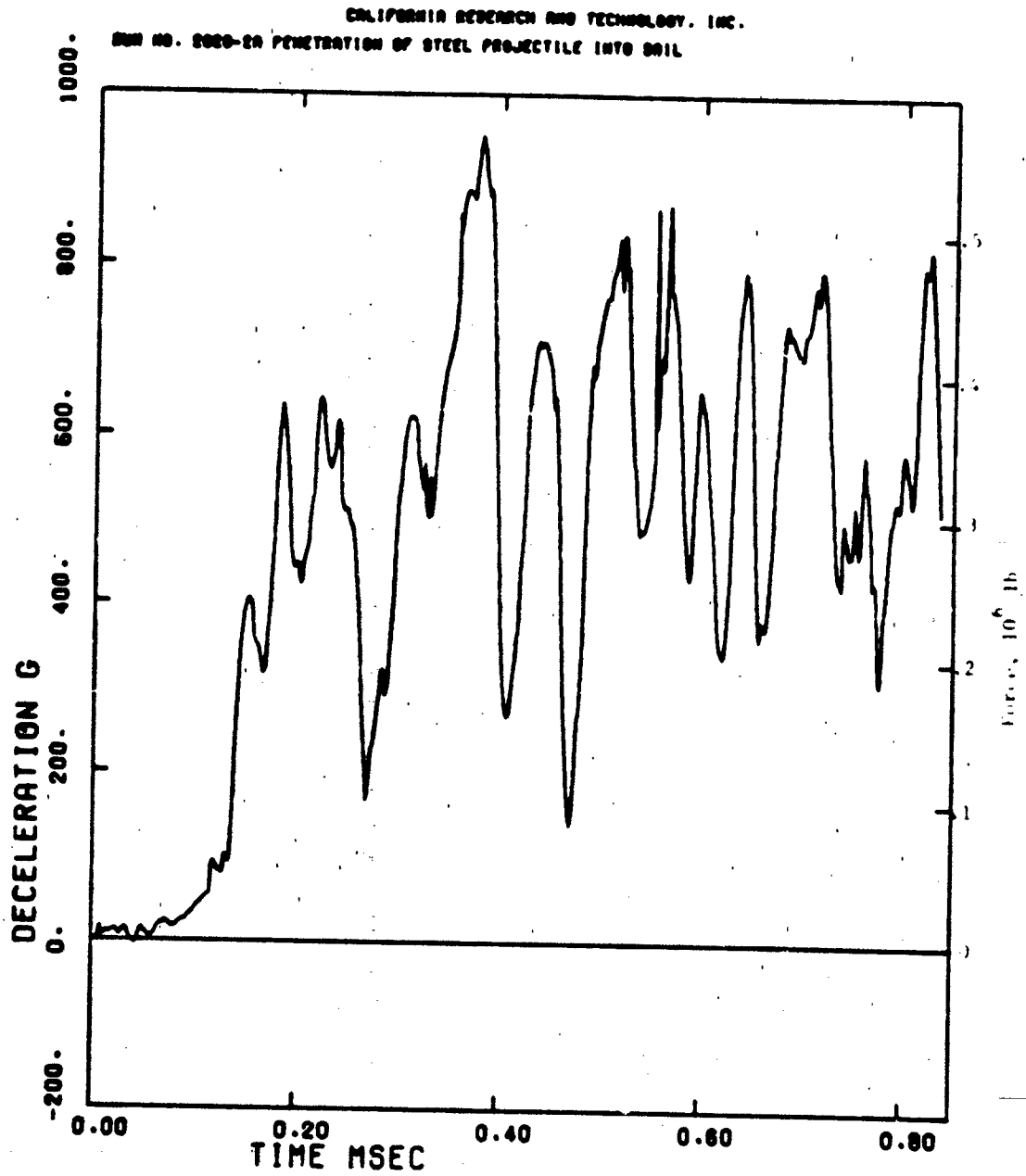

Figure 10. Axial force on Projectile and Deceleration of Projectile [illegible], Deformable-Body Solution

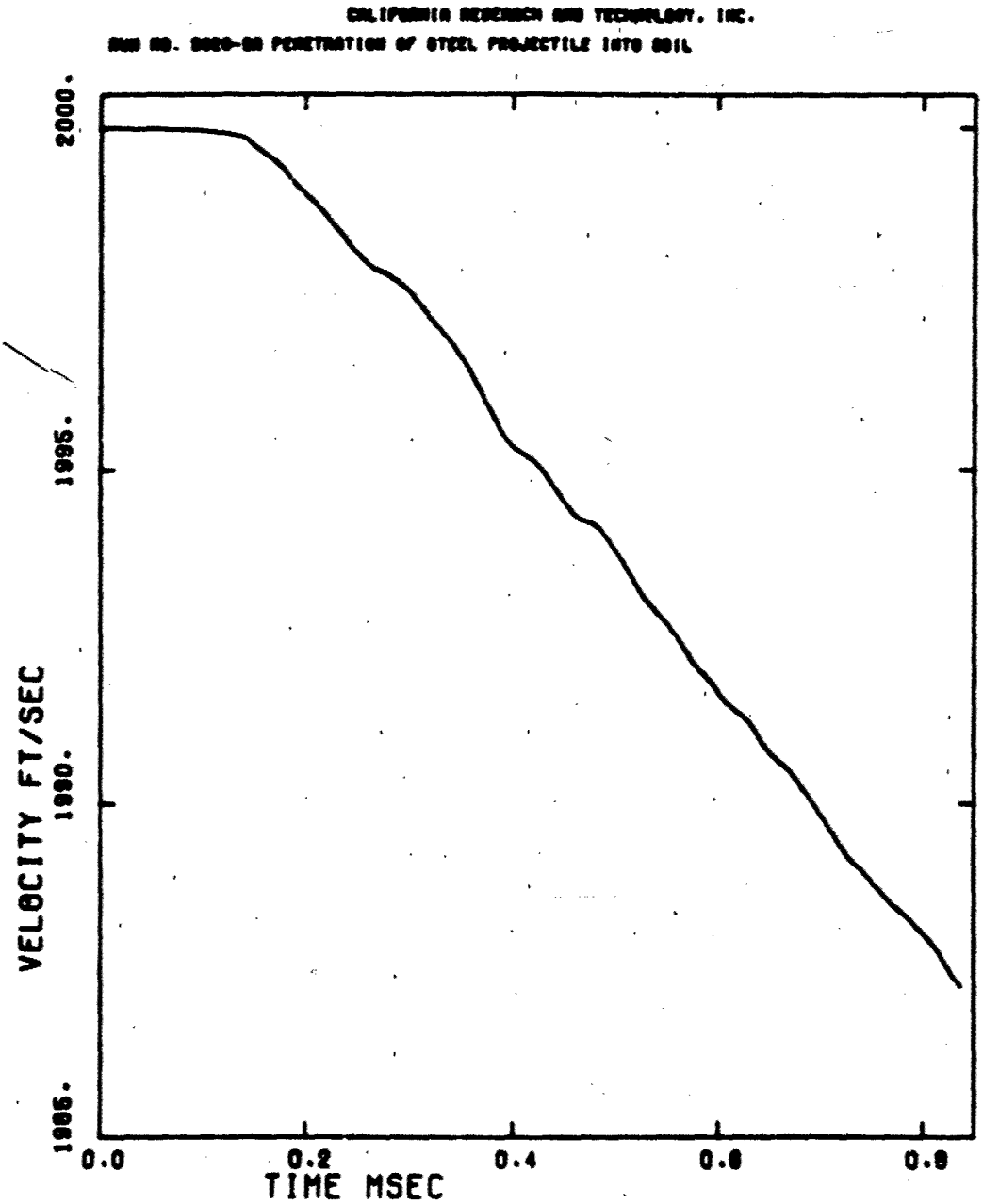

Figure 11. Projectile Velocity vs Time, Deformable-Body Solution

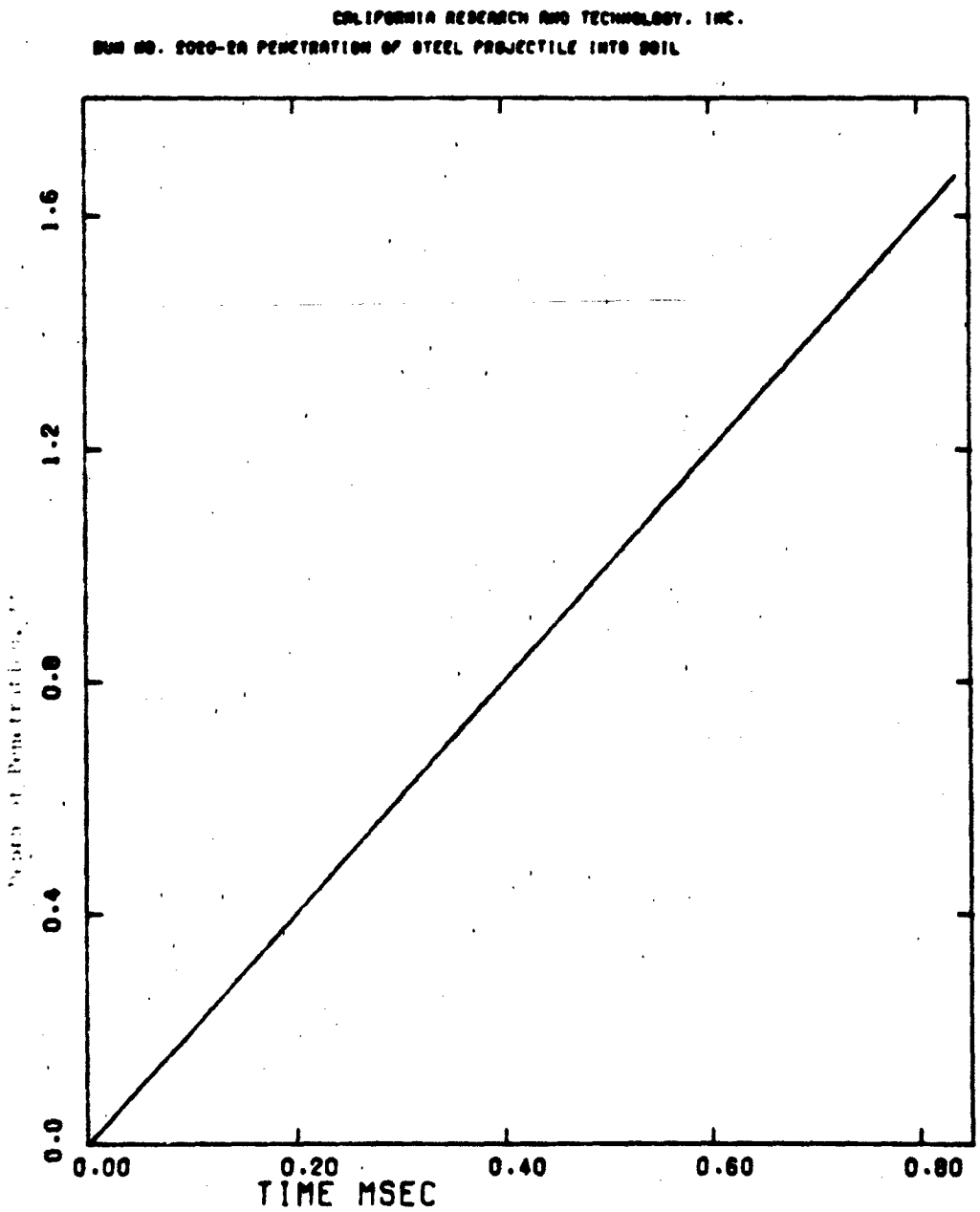

Figure 12. Depth of Penetration vs Time, Deformable-Body Solution

body solution in Section VI.

Figure 15 summarizes the peak compressive stresses experienced in the projectile near its surface (solid curve) and along its axis (dashed curve). The peak values are probably overstated due to the numerical oscillations in the surface loading on the projectile, but they show the location of critical stress regions in the projectile. The highest stresses are experienced in the first 4 inches of the nose tip and in the thin annular region connecting the nose with the body. Relatively modest compressive stress levels are seen in the wall of the projectile. Some tension is experienced near the axis of the projectile, as is shown by the vectors having leftward components in Figure 9.

Figures 14 and 15 show mean normal stress vs distance profiles just inside the projectile surface at a sequence of times after impact, i.e. $(\sigma_1+\sigma_2+\sigma_3)/3$ in the row of steel cells along the periphery of the projectile. The progression of increasing stress along the projectile is seen. All of the profiles after .1 msec show a sharp drop about 5 in. back from the nose tip. At later times, the mean normal stress peaks again in the narrow connection between the nose and body (near 20 inches). Figure 16 shows mean normal stress vs distance profiles along the projectile axis. Tension occurs at the leading surface of the slug. The decelerating force on the cylindrical slug is being applied only around its periphery. This produces tension in the unsupported front surface.

Stress, velocity and displacement histories were obtained at several stations in the soil and within the projectile. These are available to interested readers in unpublished form at WES.[9]

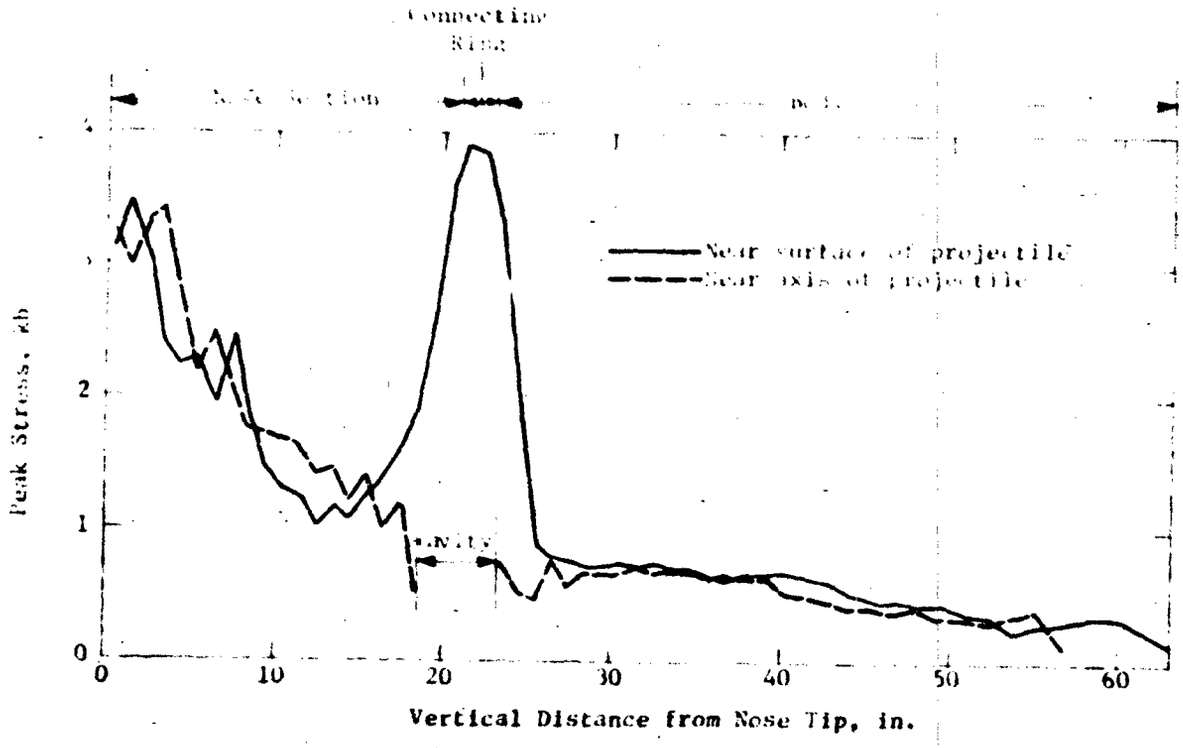

Figure 13. Peak Compressive Stresses Experienced in Projectile

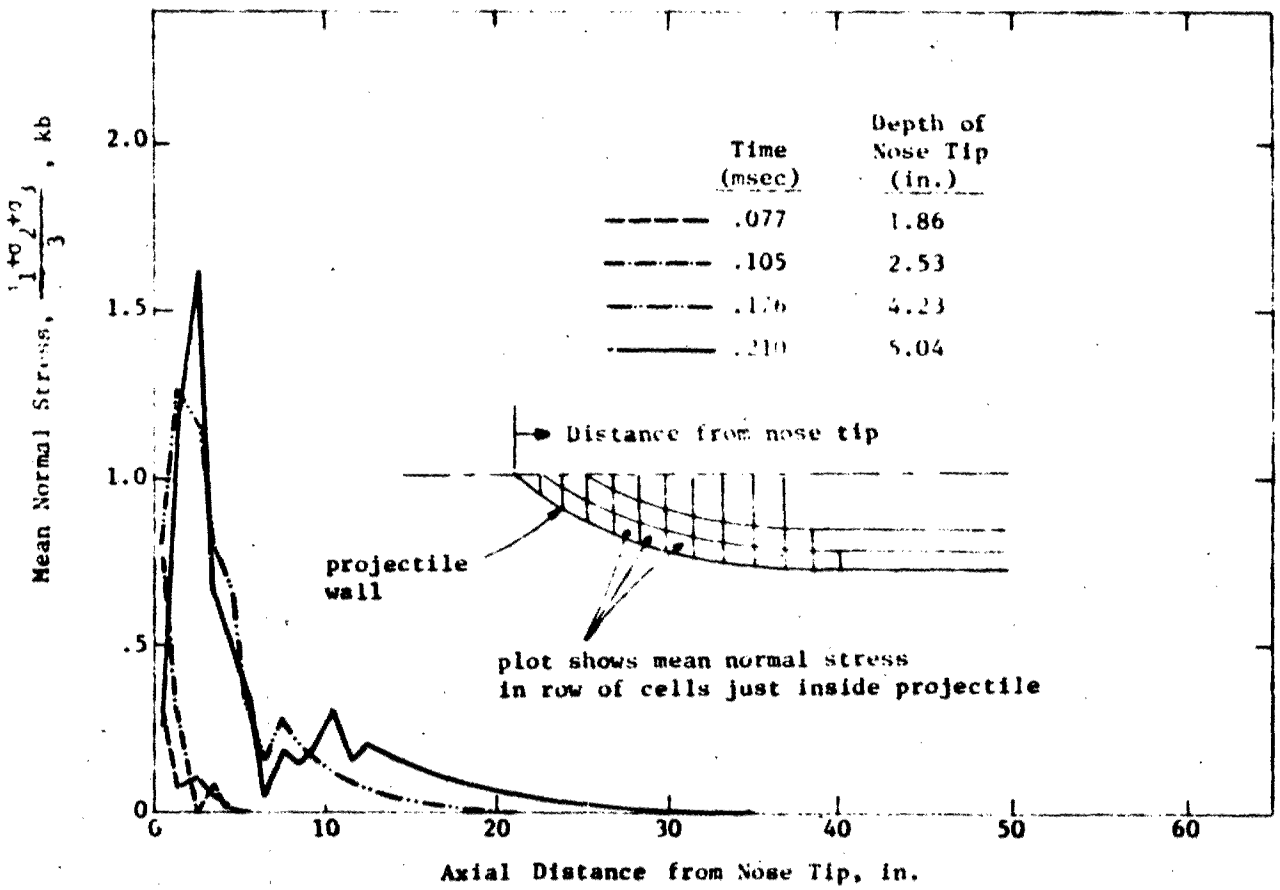

Figure 14. Early-Time Profiles of Mean Normal Stress Just Inside Projectile Wall

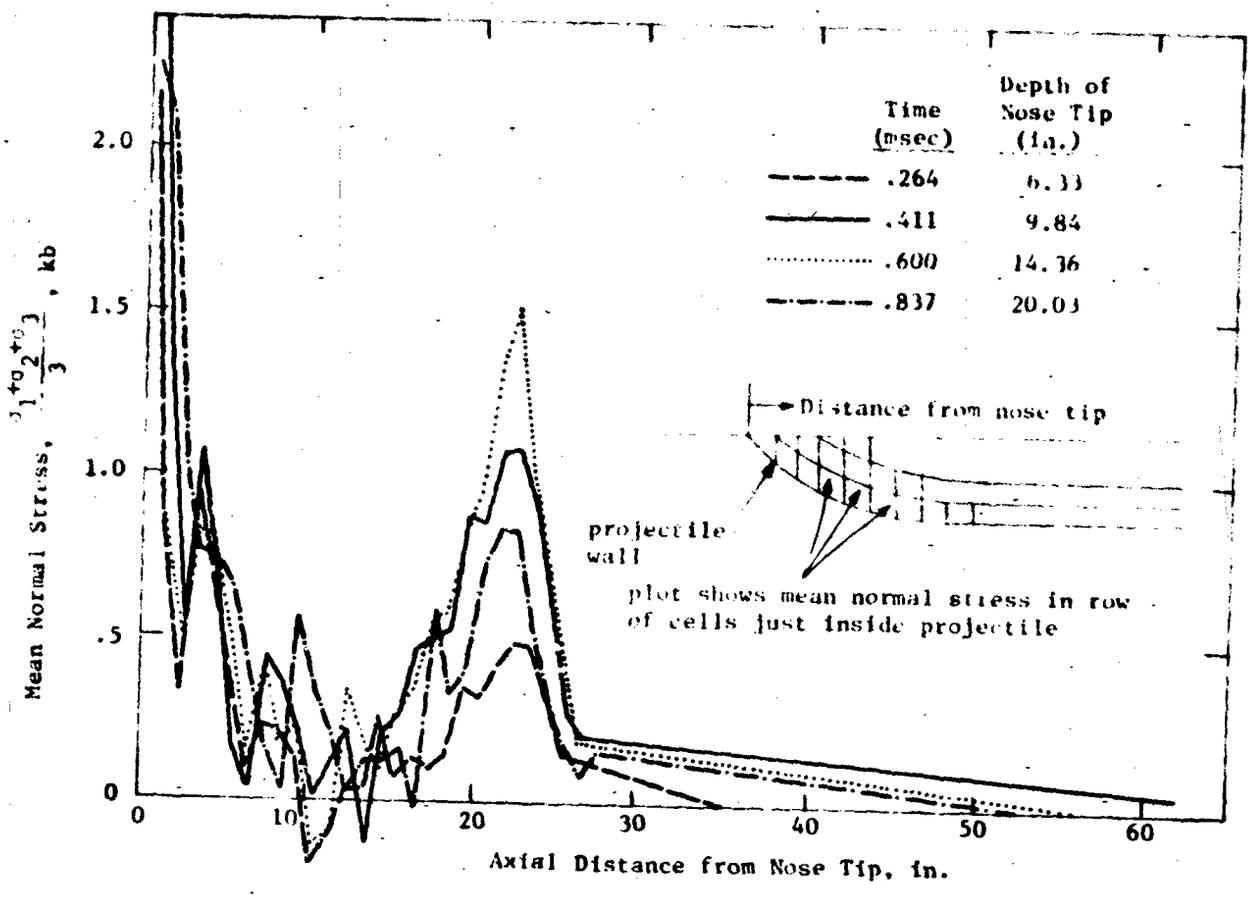

Figure 15. Later-Time Profiles of Mean Normal Stress Just Inside Projectile Wall

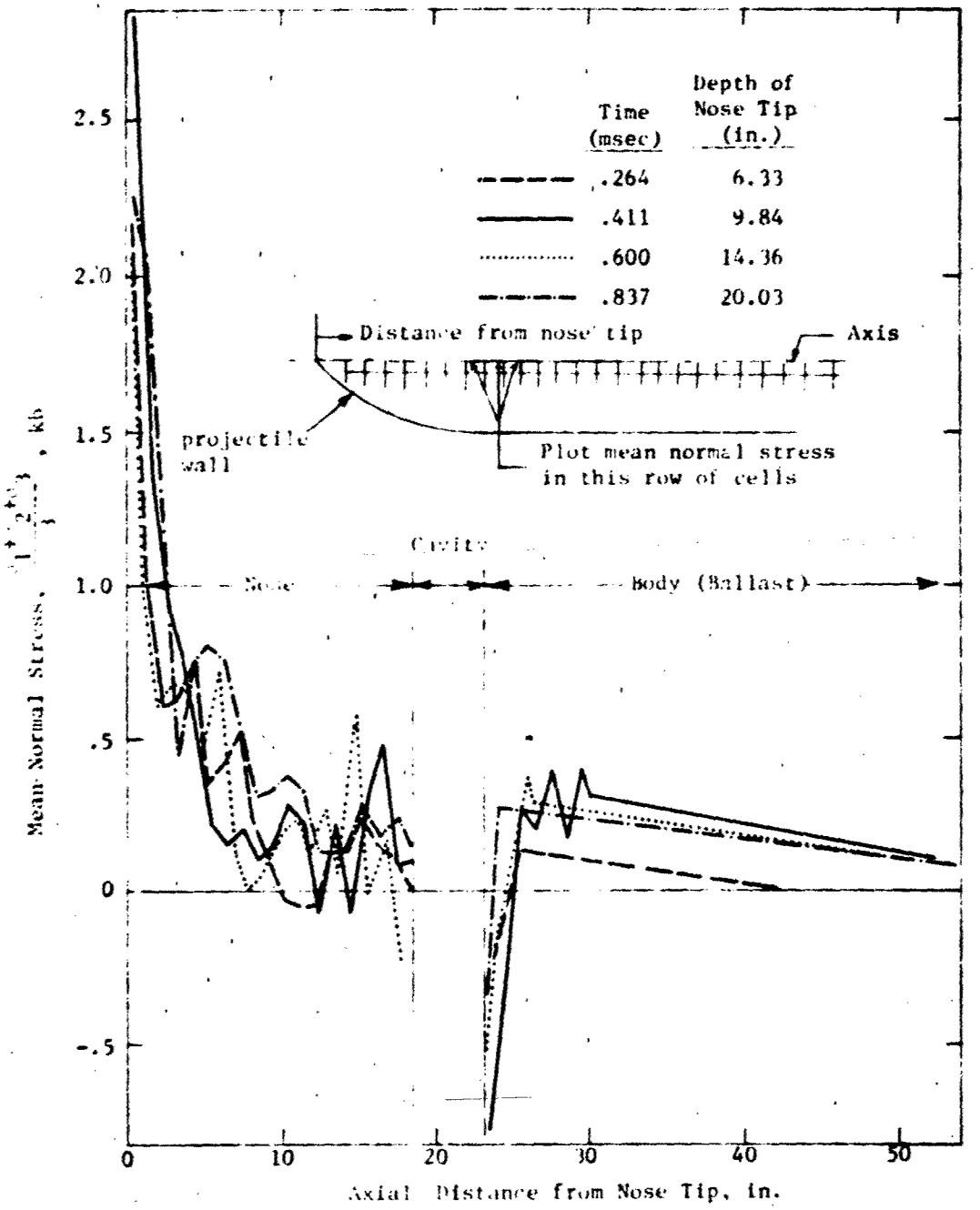

Figure 16. Mean Normal Stress Profiles Along Projectile Axis

SECTION V

RIGID-BODY SOLUTION

In a deep penetration, the target material undergoes large distortions, while the projectile does not generally undergo any significant plastic deformation. To analyze the long-time processes of deep projectile penetration, including the projectile response, with a complete elastic-plastic code solution would require an impractical amount of computer time. This situation can be alleviated by treating the projectile as a rigid body, while analyzing the soil response and consequent forces on the projectile surface using the regular elastic-plastic formulation of the code. The rigid-body assumption is justified so long as the projectile deformations are not large enough to significantly interact with the target response or penetration dynamics.

The advantage of this approach is seen in the following considerations. Computational time is determined by the total number of cells and by the numer of integration cycles in a solution (i.e., the total number of cell-cycles). The number of cycles is proportional to the reciprocal of the time step, which in turn is set by the time it takes the fastest wave (generally a dilatational or sound wave) to cross the smallest cell dimension; $\Delta t_{max} \propto (\frac{\Delta x}{c})_{min}$. By describing the projectile as a rigid body, the computational time can be reduced, since:

(i) Larger cells can be used (the small cells required to resolve details of the projectile response are no longer needed)

(2) Longer time steps can be used (both because of the larger cells, and because of the lower sound speeds usually associated with soft earth materials as contrasted to projectile materials).

Use of this approach does not preclude analysis of the interior response of the projectile. From the rigid-body solution, stress loading histories imposed on the projectile surface are determined. This information can then be used to "drive" a deformable body analysis of the stress wave response in the penetrator itself. This coupled technique has been successfully employed on another program.[5]

5.1 GRID DESIGN

The computational grid for the rigid-body solution is shown in Figure 17. The contour of the penetrator periphery was resolved with a total of 33 lattice points, spaced at 2 in. intervals. The computational grid in the target was divided into two principal regions, as shown in Figure 17. From the problem axis of symmetry out to a radius of 20 in., uniform zoning of 2 x 2-in. cells was used. Beyond 20-in. radius, the radial zone width was increased in 10% steps. The grid extended to a radius of 7 ft. In this outer region, the vertical zone width Δz also increased (with increasing depth) in 10% steps until it reached a maximum value of 10 z_0. This design for the outer region conserves computational cells, without significantly affecting the solution.

As in the deformable body case, the K-line running along the penetrator contour and along the axis of the target was a slide line. Another slide line was used along

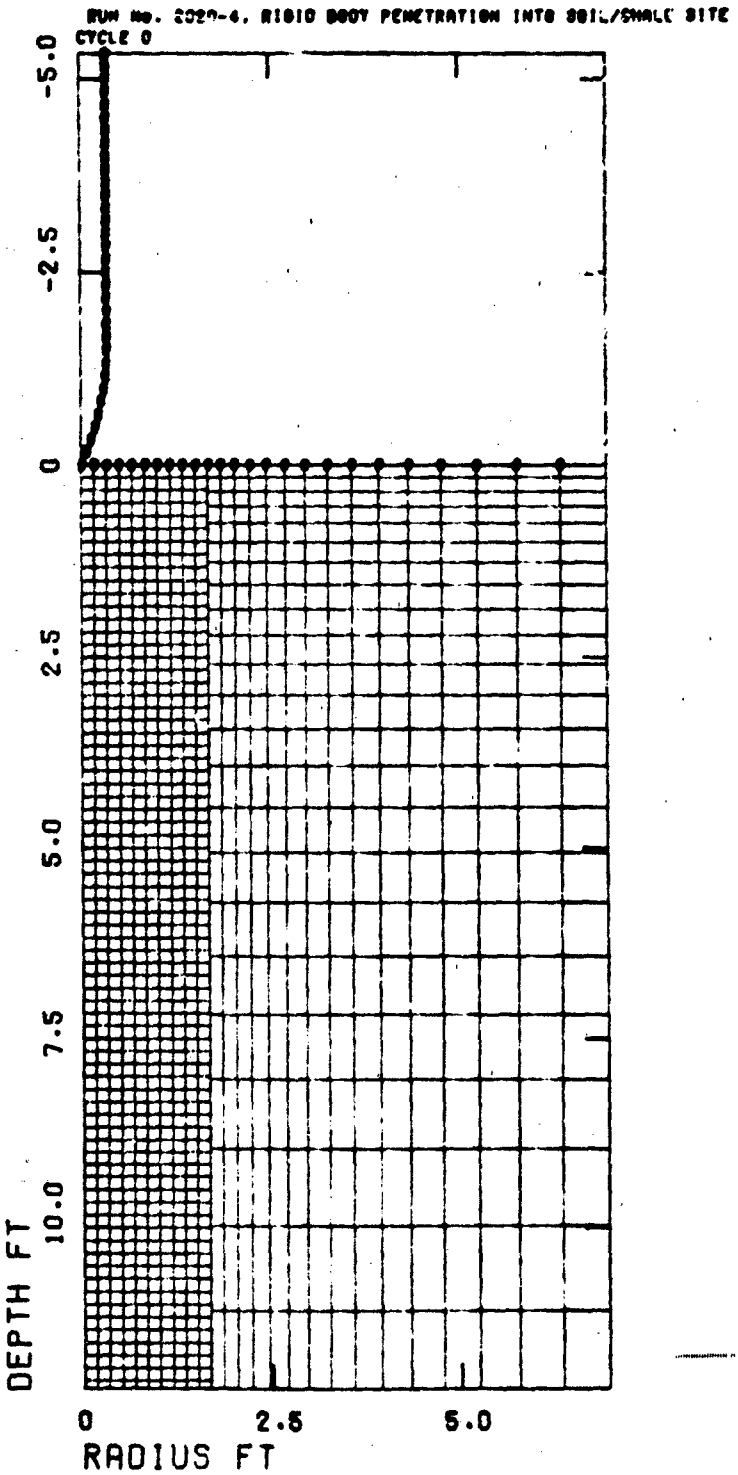

Figure 17. Initial Grid Configuration for Rigid-Body Solution

the boundary between the inner and outer grid regions in order to accommodate the differing alignment of the grids on both sides. No significant slippage occurs at this range. This type zoning has been used in Refs. 3 and 4.

As discussed in Section 4.1, the lattice points at the origin, corresponding to the projectile tip and the soil point at ground zero, were initially decoupled for this rigid body solution. All the soil points are thus initially at rest.

5.2 RIGID PROJECTILE SOLUTION RESULTS

Penetration of the rigid projectile was numerically analyzed through layer 1 (soil) and for about one projectile length into layer 2 (shale), to a total depth of 22.5 ft. The grid configuration at an intermediate penetration depth of 11.4 ft is shown in Figure 18. The "notches" in the open hole behind the projectile are due to periodic deletions of distorted cells after the projectile passes. Cells in this region no longer have any significant effect on the penetration process, and their removal improves computational efficiency.

At the point in the solution shown in Figure 18, the wave front in the ground had nearly reached the bottom of the initial computational grid at 12.2 ft. (Remember that the projectile velocity was supersonic relative to the dilatational wave velocity in the undisturbed soil.) To extend the grid without increasing the number of cells, a "rolling grid" process was used, wherein the material behind the projectile, from the surface down to 5.7 ft was deleted, and material was added below the initial grid,

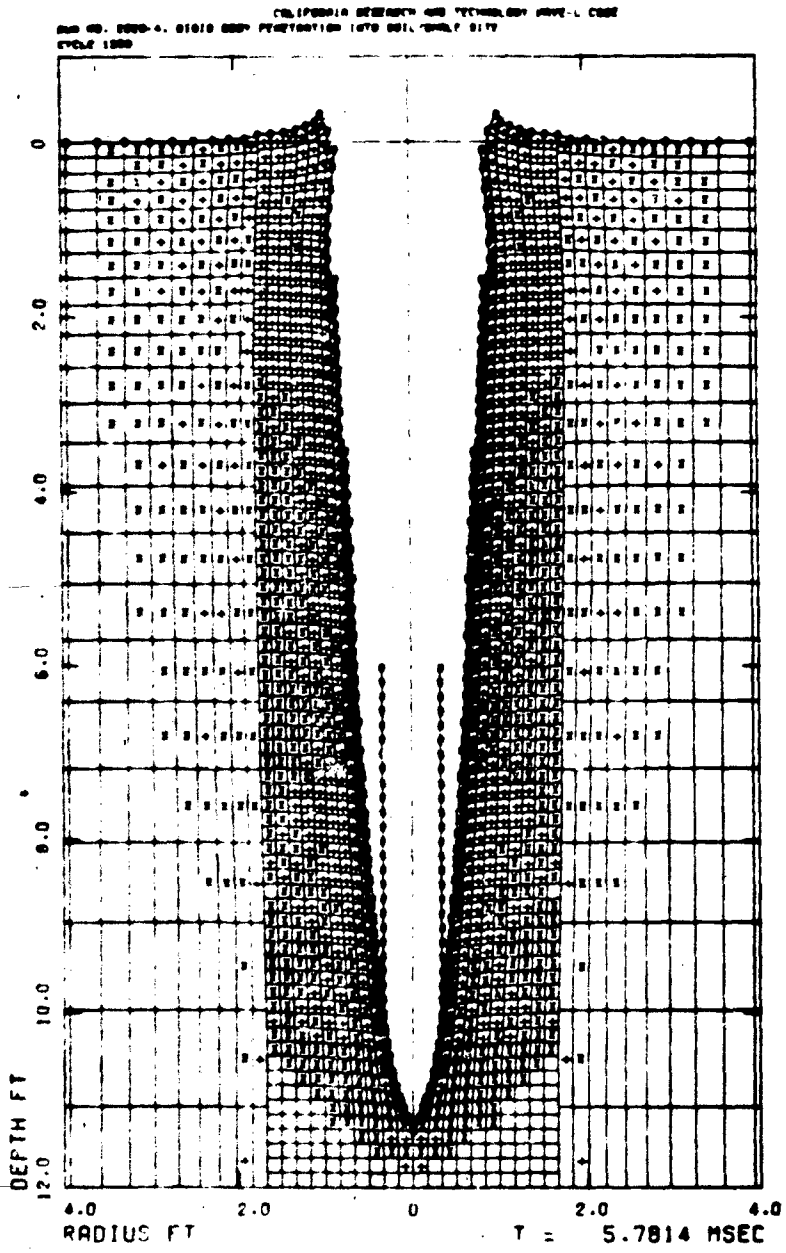

Figure 18. Grid Configuration with Projectile at 11.4 ft Depth - Before Rezone

extending it to a depth of 25.2 ft. (Later, the grid was extended again, to 26.5 ft depth.) Pre-deformation of the new grid, wherein the first two columns of cells next to the axis are canted slightly upward, was also introduced at this time. This predeformation improves the orthogonality of cells as they distort while flowing out and around the nose. The pre-deformation is geometric only. The initial physical state of material in the predeformed cells is the same as in normal cells. Figure 19 shows the grid at 12.4 ft penetration after the aforementioned alterations. Note that the grid canting began gradually starting at 1.2 ft depth, so as to avoid a discontinuity.

Figures 20, 21 and 22 show the grid configuration, particle velocity field, and principal stress field at the end of the solution at 11.0 msec, with the projectile nose at 22.5 ft depth. A series of field plots obtained at a sequence of times during the solution is contained in Appendix C.

Figure 23 shows the time histories of the total axial force applied to the projectile, and the resultant decelerations. Figure 24 shows axial force/deceleration vs depth of penetration. The discrete nature of the computational grid introduces oscillations in the force/acceleration traces. As the projectile cuts through the grid, it feels the effects of the load/unload cycle in each cell as that cell slides around the nose surface. In the present problem, the frequency with which the nose encountered new cells was about 12 kHz. This frequency is apparent in the force/acceleration histories in Figures

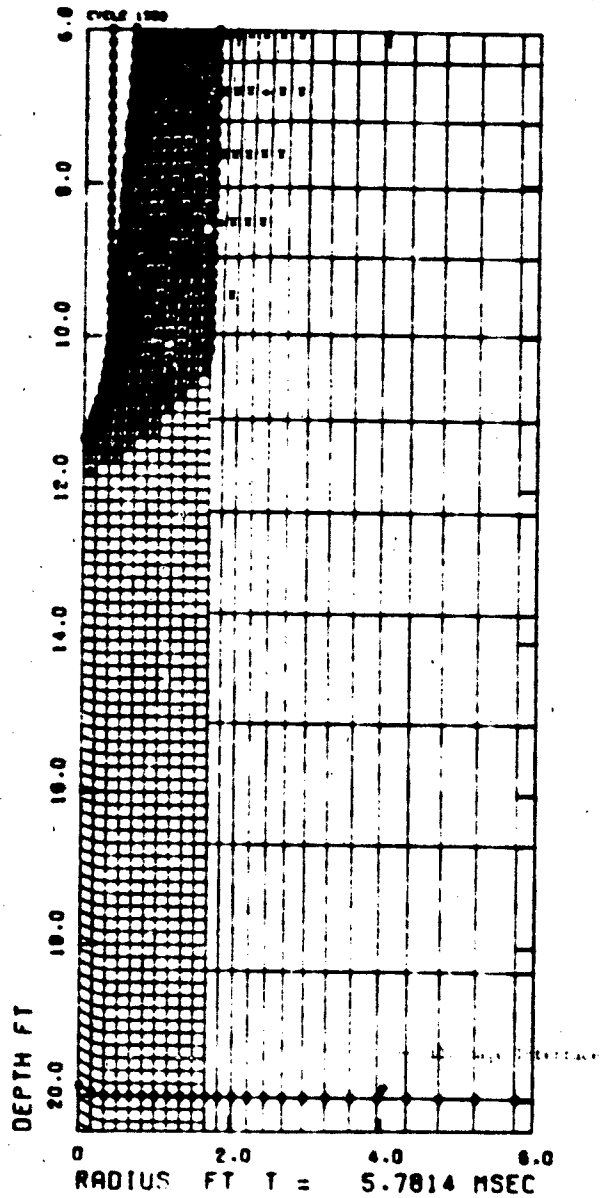

Figure 19. Grid Configuration with Projectile at 11.4 ft Depth - after Rezone

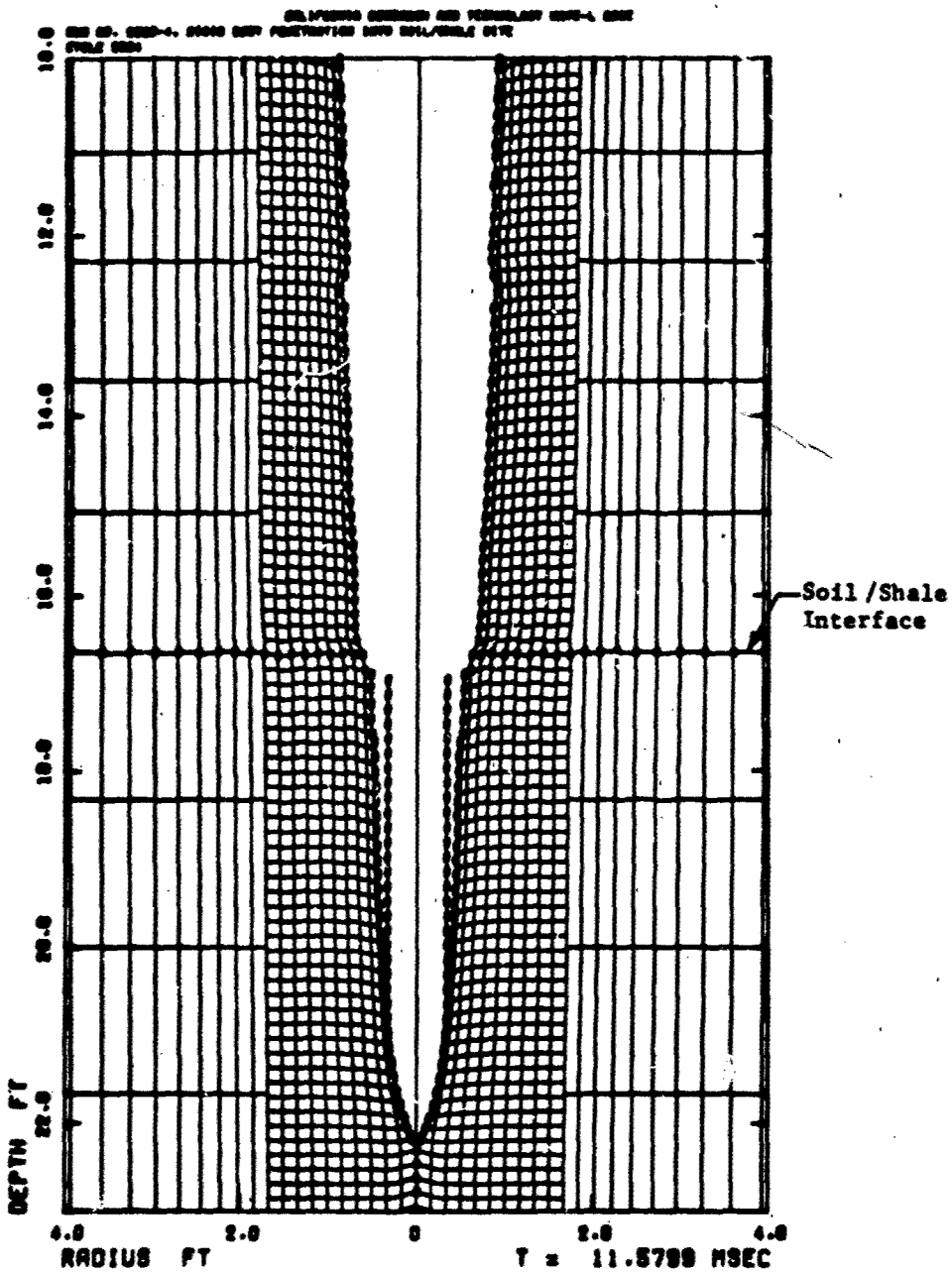

Figure 20. Grid Configuration at End of Rigid Body Solution, Projectile at 22.3 ft Depth

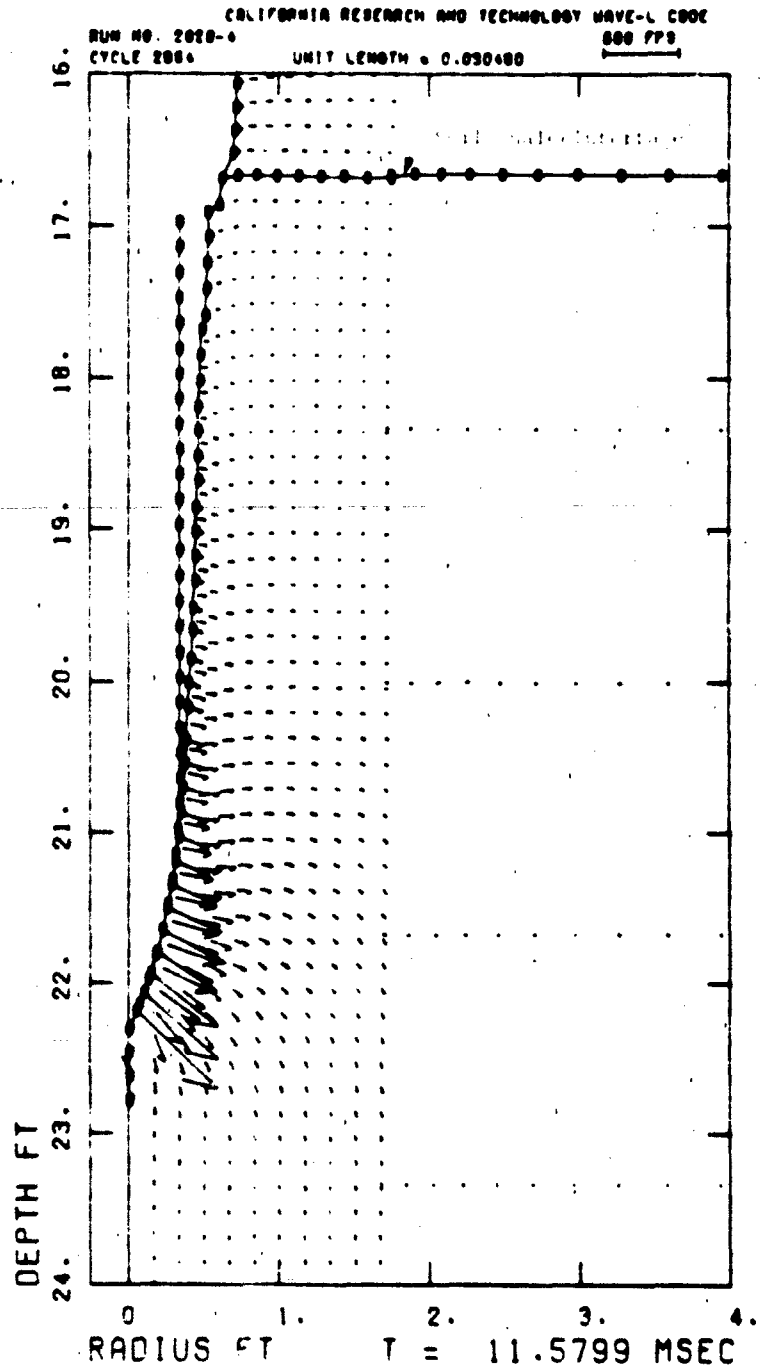

Figure 21. Particle Velocity Field at End of Rigid Body Motion, [illegible] at 22.5 ft Depth

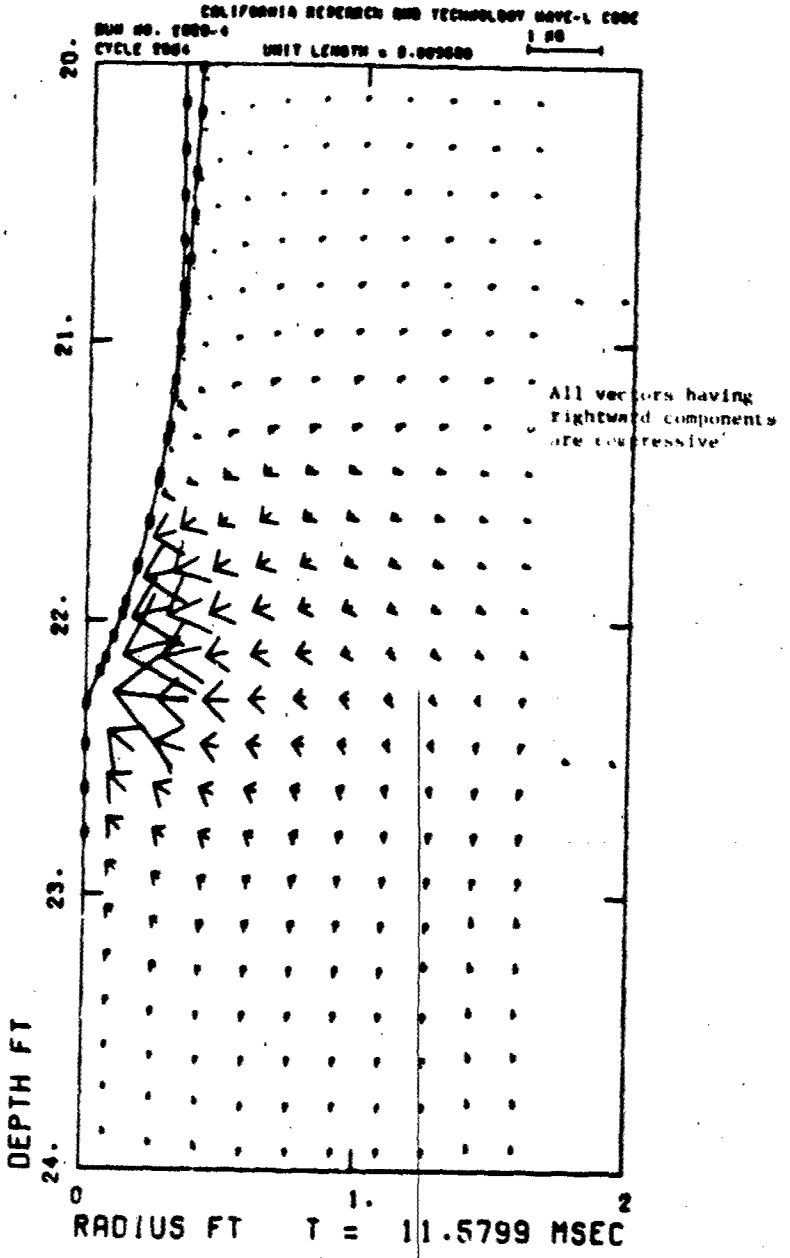

Figure 22. Principal Stress Field at End of Rigid Body Solution, Projectile at 22.3 ft Depth

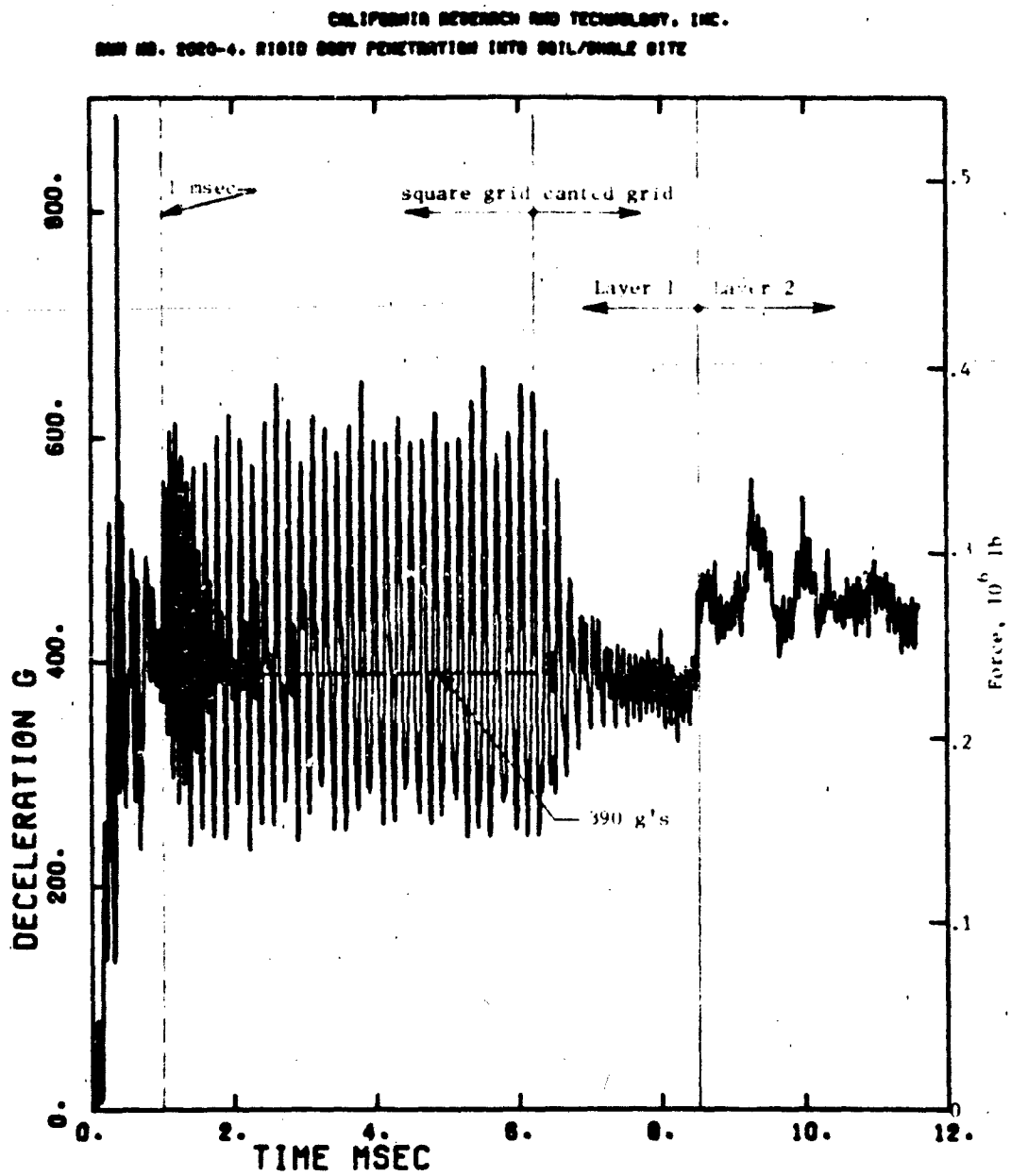

Figure 23. Axial Force on Penetrator and Deceleration of Projectile vs Time, Rigid Body Solution

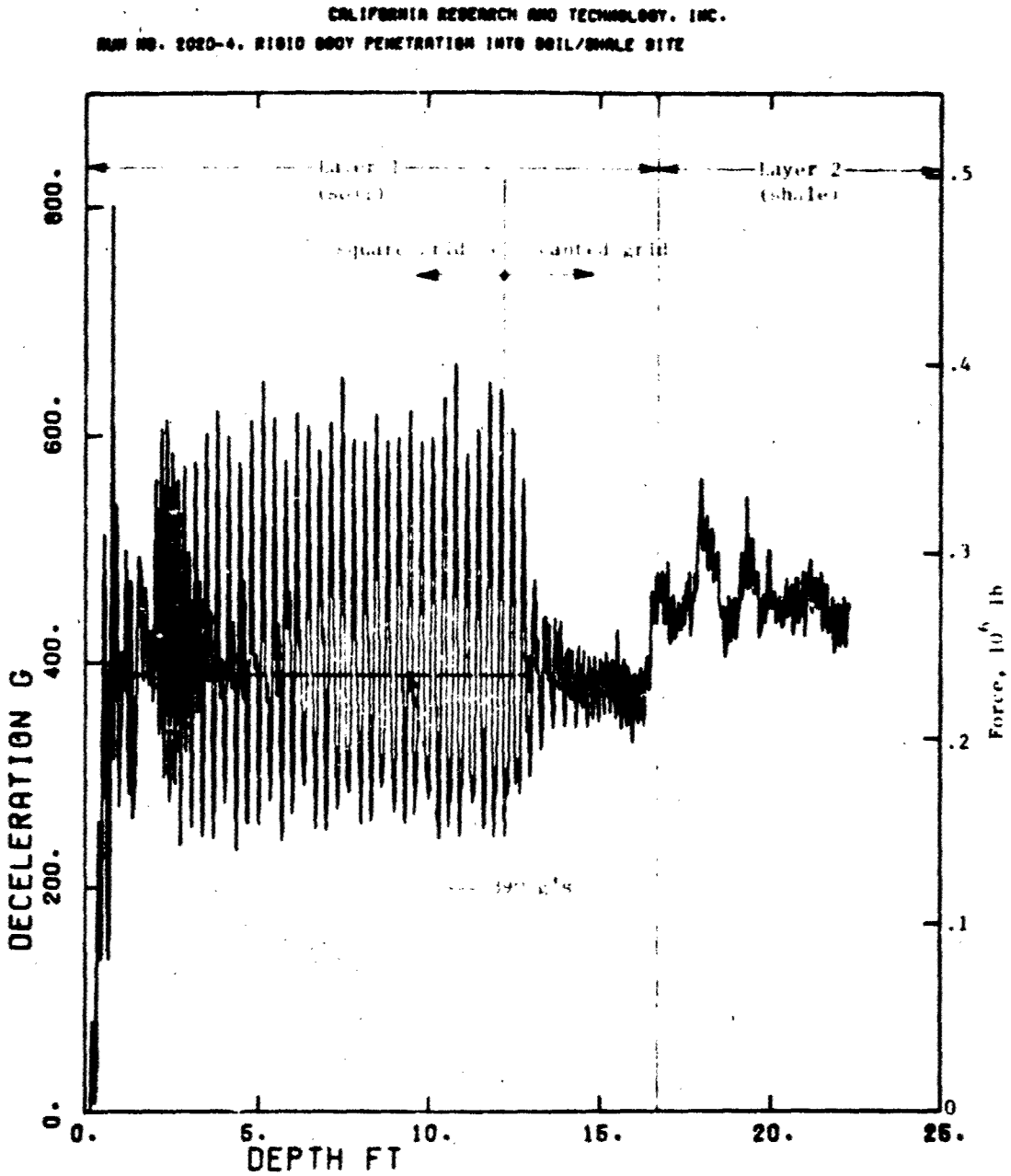

Figure 24. Axial Force on Penetrator and Acceleration of Penetrator vs Depth of Penetration

23 and 24 at early times and at times after about 7 msec (depths below about 13 ft).

In the region between about 1 and 6.5 msec (about 2-12 ft depth), regular, much more severe oscillations at about 6 kHz are seen. These were apparently due to synchronous, amplifying interactions between the discrete nature of the grid, the strongly hysteretic nature of the loading unloading-reloading cycle in the material model, and the gross distortions of the cells moving up the sides of the projectile. The initial loading wave velocity in the Layer 1 model was about 540 fps. Unloading (and reloading) always occurred at a much higher velocity; i.e., of the order of 6000-7000 fps. The gross distortion of cells moving out and around the nose caused large loading-unloading oscillations in the few cells which were applying significant axial forces to the nose. The pressure profiles in Figure 25 illustrate such oscillations.

For the reasons cited above, the oscillations in the solution between about 1 msec and 6.5 msec (2 ft and 12 ft in depth) are greatly exaggerated and should be disregarded. However, the average deceleration in this region (425 g's) should still be fairly realistic. And indeed it is seen in Figures 23 and 24 that the average deceleration level drops only about 10% (to about 390 g's) when the severe oscillations go away with the introduction of the predeformed, or canted grid. Is this drop due to the grid geometry change as such, or to the elimination of exaggerated forces in the synchronous oscillations? Apparently the latter: the grid canting was introduced in a very gradual fashion ahead of the projectile, and it required only the very slight

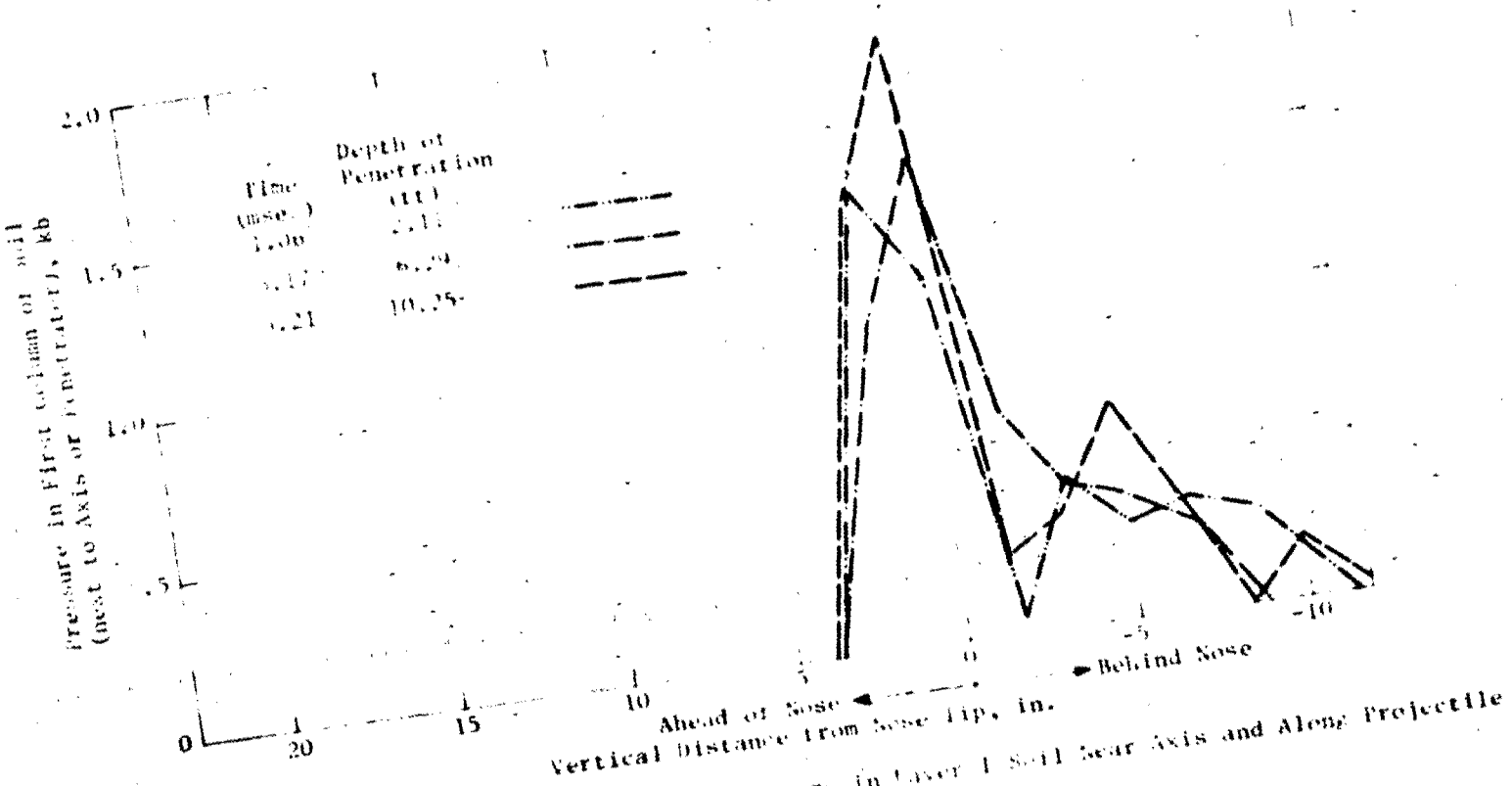

Figure 25. Representative Profiles of Pressure in Layer 1 Soil Near Axis and Along Projectile Surface - Normal Orthogonal Grid

change in grid geometry which occurred in the first few inches below 12.2 ft (see Figure 19) to eliminate the synchronous interactions. As soon as the severe oscillations were reduced, the average deceleration level dropped to 390 g's. We regard this as the more accurate indication of the deceleration level in Layer 1.

Figure 26 gives pressure profiles in Layer 1 (after introduction of the predeformed grid) and in Layer 2, and illustrates the smoother profiles which were obtained.

The average deceleration increased to about 440 g's in the Layer 2 shale. Figures 27 and 28 show the velocity and depth histories. (A constant deceleration of 390 g's was assumed between 2 ft and 12 ft depth.) Figure 29 shows the velocity vs depth. Energy partitioning between the projectile and target during the course of this solution is shown in Figure 30.

Stress, velocity, and displacement histories were obtained at several stations within the target media. These are available to interested readers in unpublished form at WES.

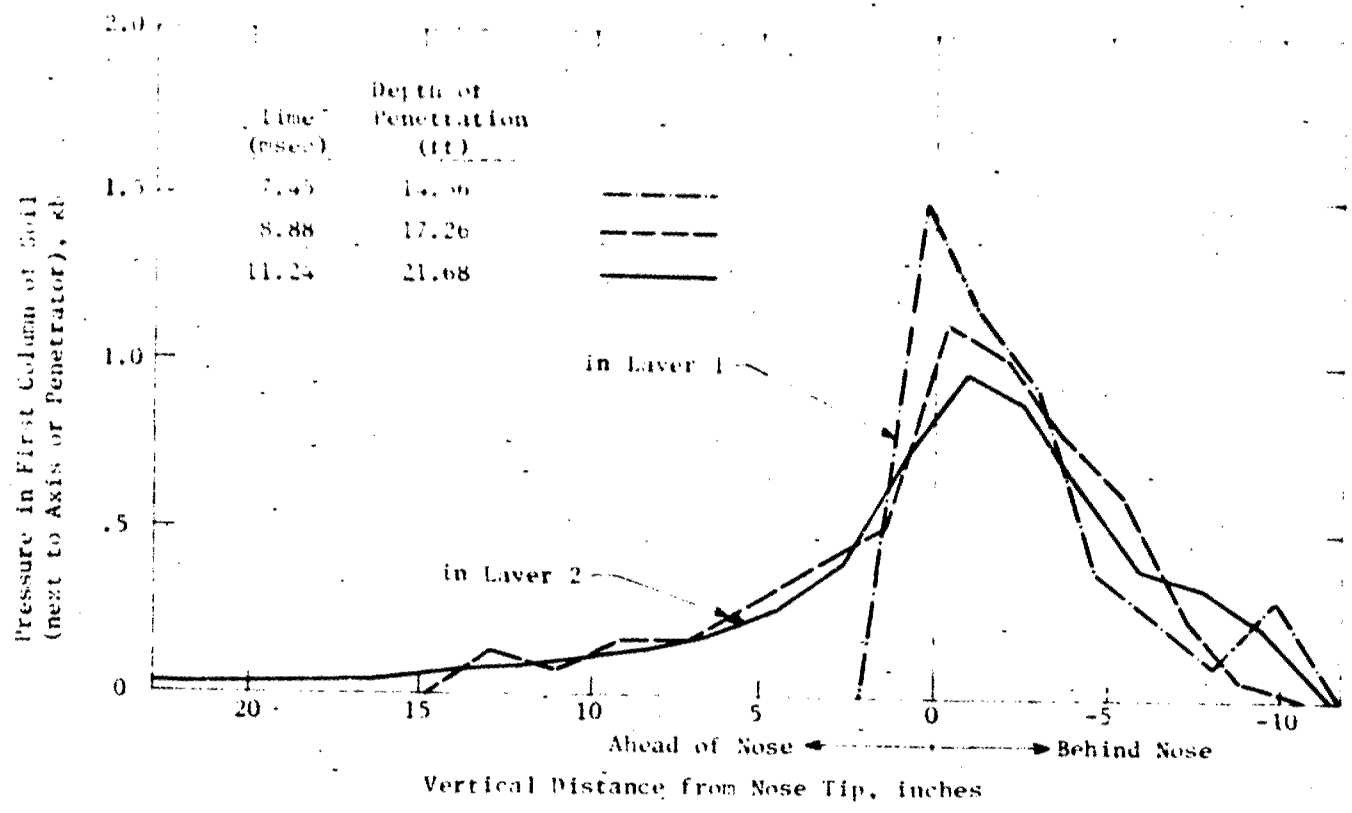

Figure 26. Representative Profiles of Pressure in Layer 1 Soil and in Layer 2 Shale Near Axis and Along Projectile Surface - Canted Grid

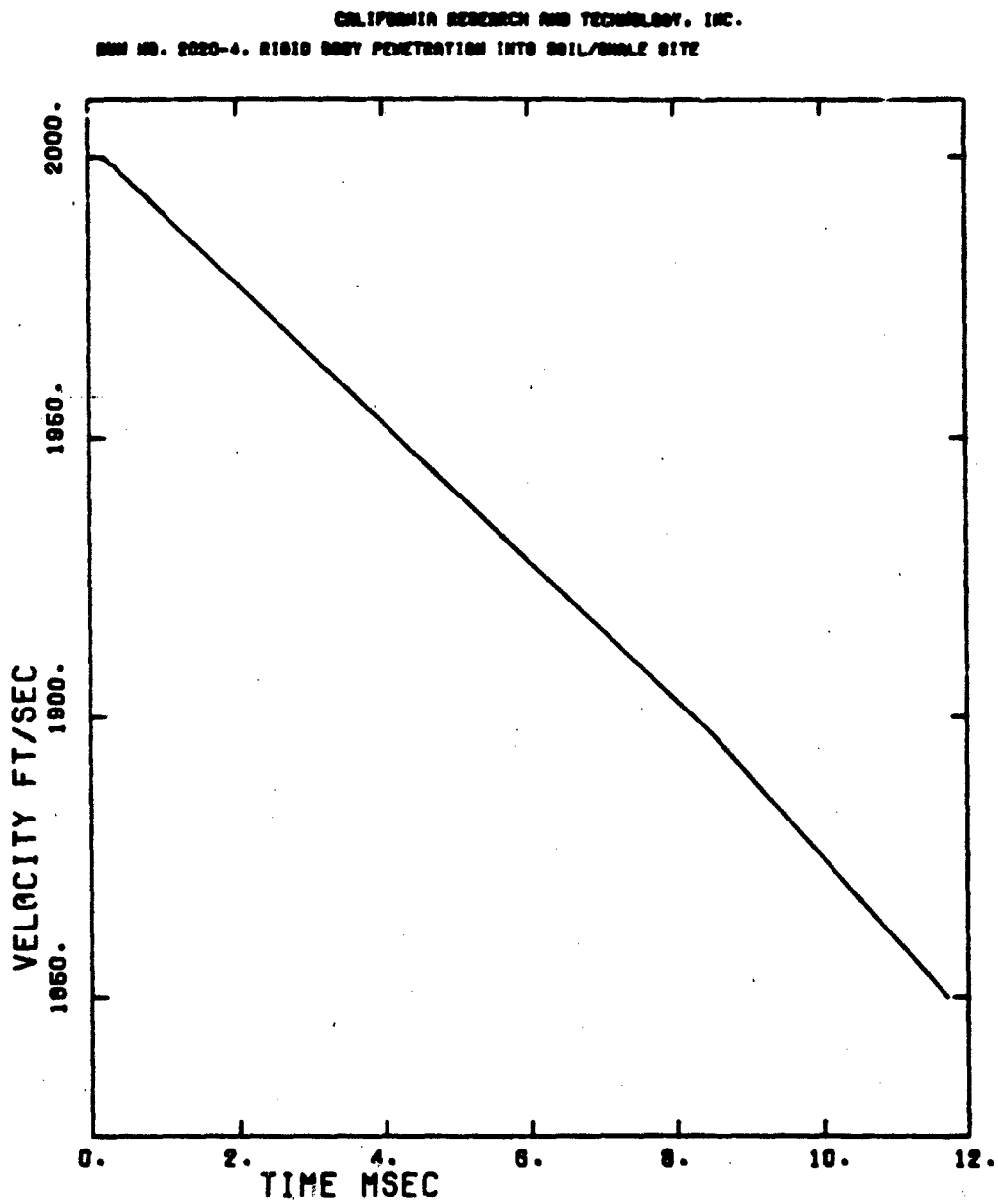

Figure 27. Penetrator Velocity vs Time, Rigid Body Solution

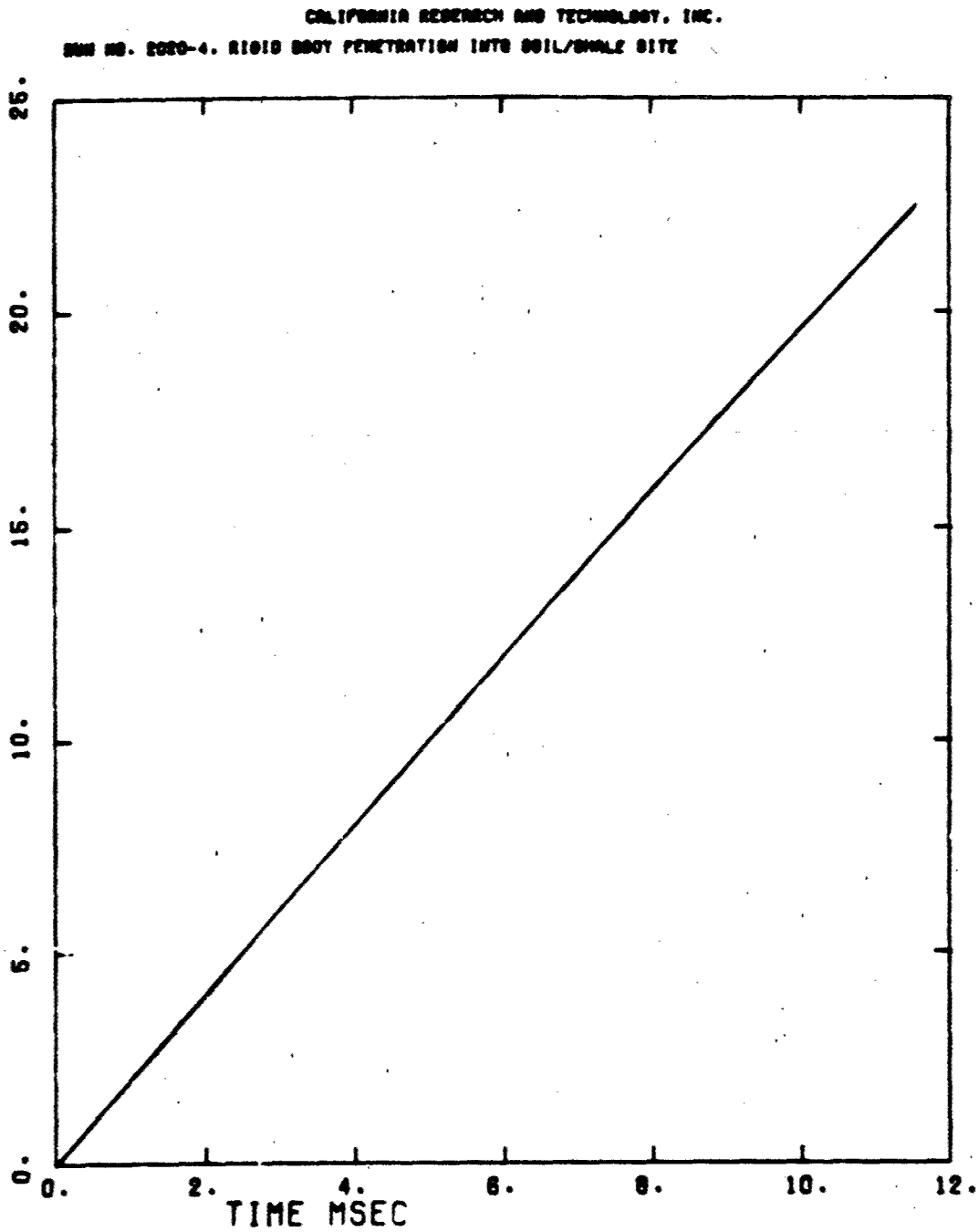
CALIFORNIA RESEARCH AND TECHNOLOGY, INC.
RUN NO. 2020-4. RIGID BODY PENETRATION INTO SOIL/SHALE SITE
25.
20.
15.
10.
5.
0.
0.
2.
4.
6.
8.
10.
12.
TIME MSEC

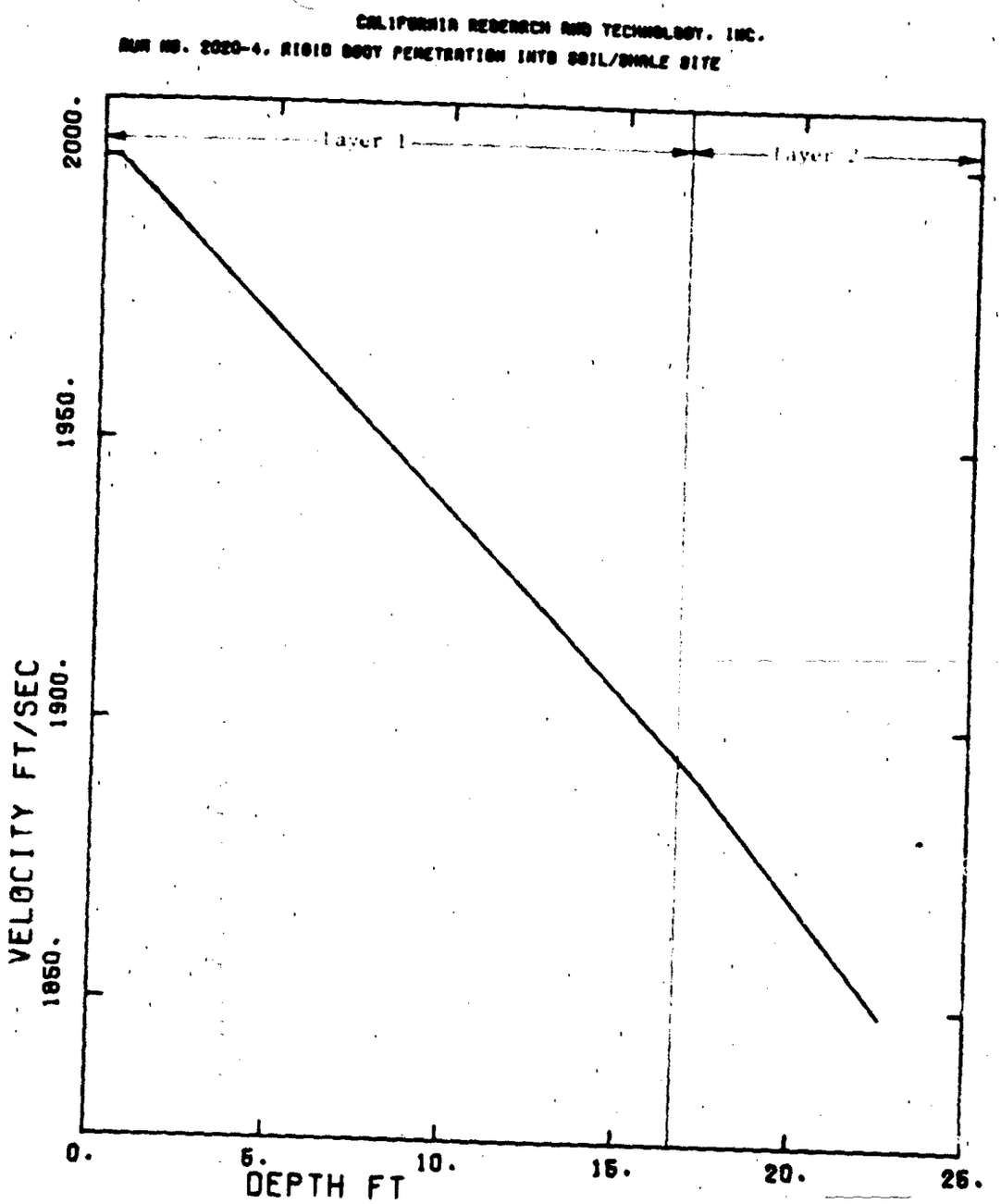

Figure 32. Penetrator Velocity vs Depth of Penetration

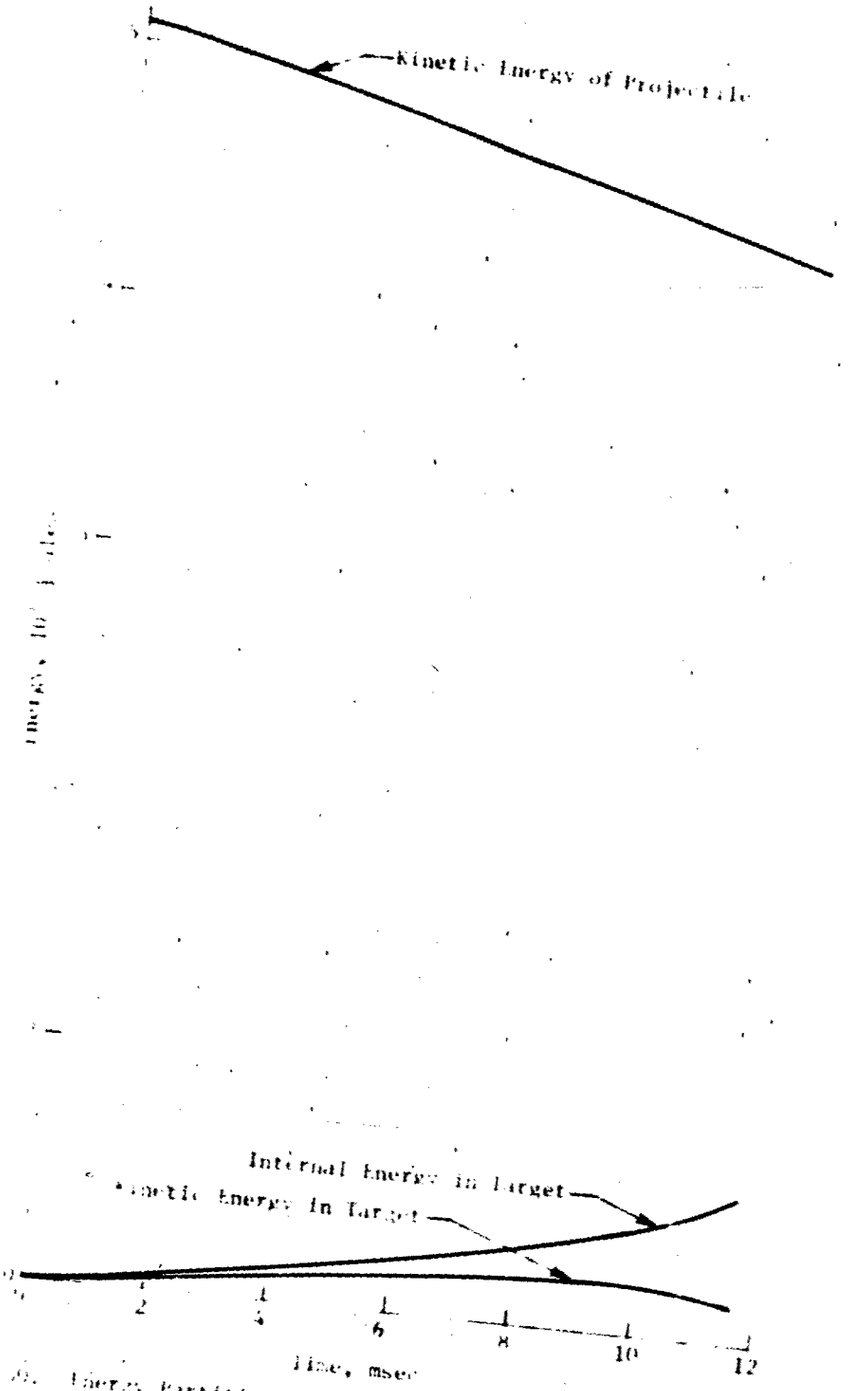

Figure 30. Energy Partition During Rigid Body Projectile Calculation

SECTION VI

COMPARISONS OF DEFORMABLE-BODY AND RIGID BODY PENETRATIONS

During the time interval covered by both solutions [illegible] the solutions for the deformable-body and rigid body penetrations can be compared. It should be kept in mind that different zoning was used in the two solutions. The basic zoning in the target in the deformable body analysis was 1 x 1 inch, while 2 x 2-inch cells were used in the rigid body solution.

Figure 51 compares the deceleration histories from the deformable-body and rigid body solutions. Both of these solutions suffered from the excessive distortion of cells moving up the penetrator nose, so the oscillations are large. The frequency of the oscillations in the deformable-body case is about twice that of the rigid-body case. This is consistent with the difference in basic cell sizes in the solutions.

The average level of acceleration is about 585 g's in the deformable case, as contrasted to about 400 g's in the rigid body case. Again, this can be attributed to zoning. Stress gradients in the soil near the nose were high. The reduced resolution in the deformable case thereby led to higher stresses being applied to the penetrator nose. Figure 52 compares typical radial stress gradients from the two solutions.

The penetrator velocity time histories from the two solutions are shown in Figure 53. At the end of the

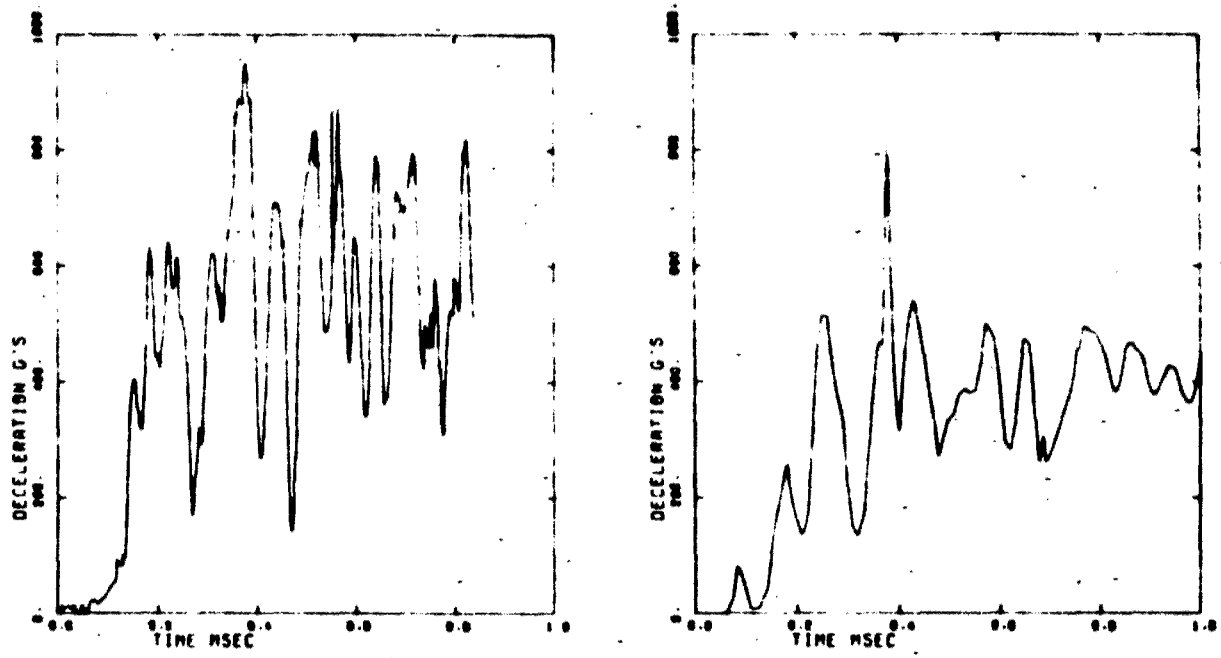

Deformable-Body Solution

Rigid-Body Solution

Figure 31. Comparison of Projectile Deceleration from Deformable-Body and Rigid-Body Solutions

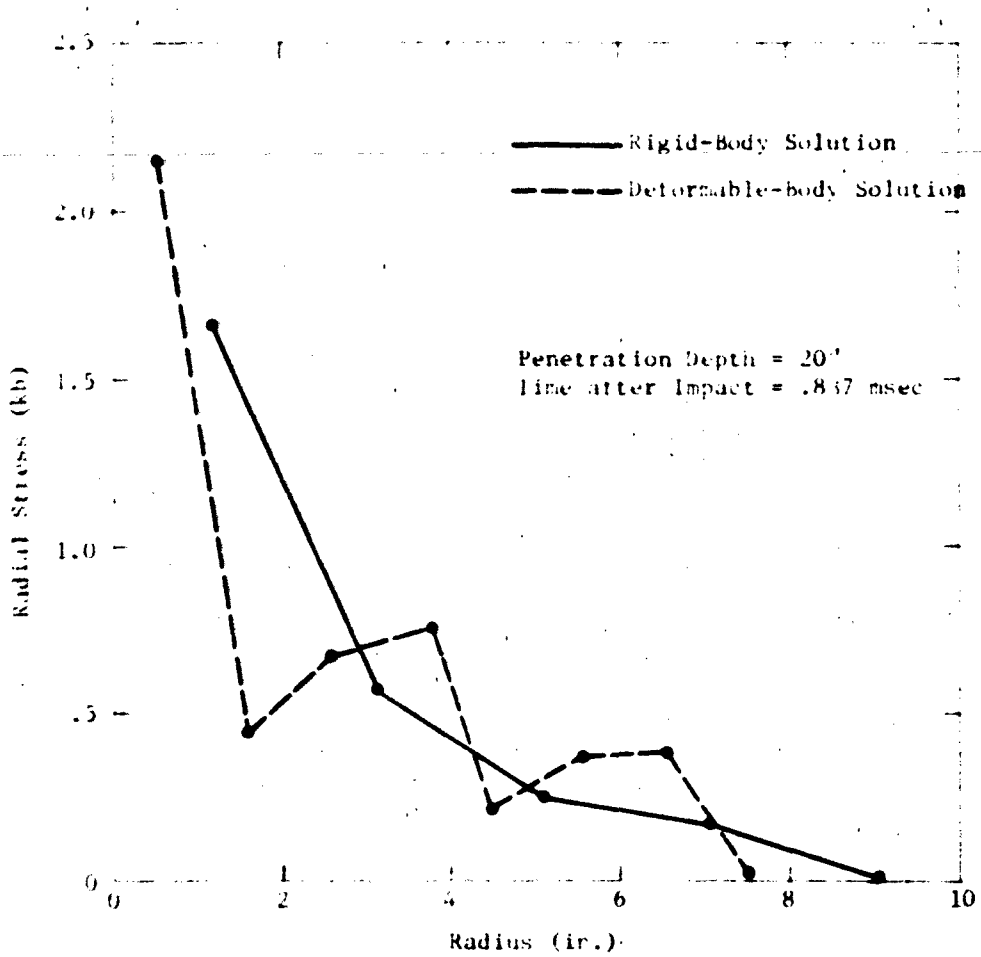

Figure 32. Comparison of Radial Stress Gradient at 20" Depth in Soil from Deformable-Body and Rigid-Body Solutions

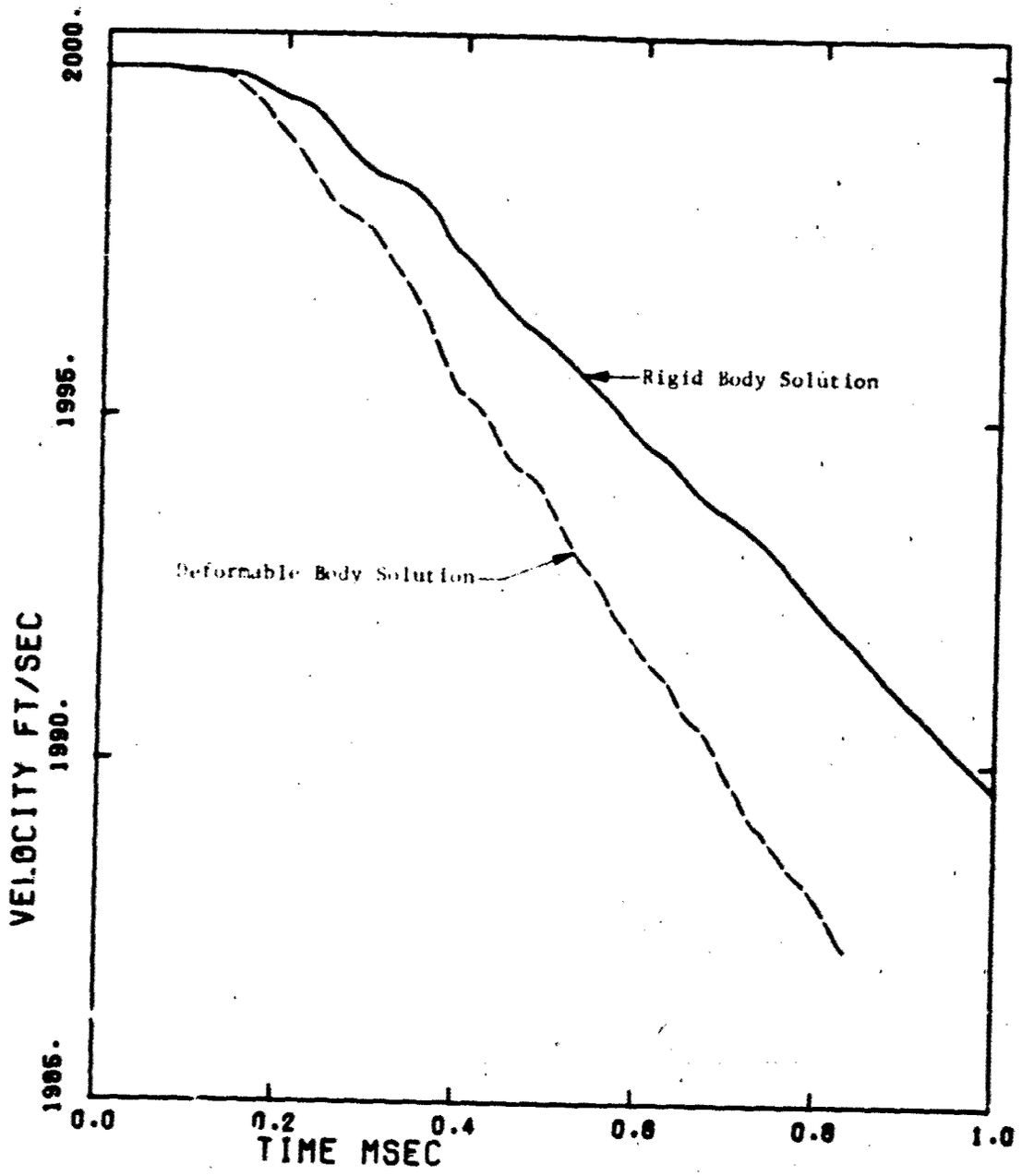

Figure 33. Comparison of Penetrator Velocity from Deformable Body and Rigid Body Solutions

deformable body solution (.84 msec), the difference in velocity was about 1.5 ft/s.

To compare the soil response, there were four time history stations positioned at the same locations in the two solutions. These were on the axis at depths of 10 and 20 in. and at 1-in. radii at the same depths. Figures 34 and 35 show comparisons of the velocity component traces for the stations at 10 in. depth. These show generally good agreement. Only a very limited comparison could be made for the station at 20 in. depth, due to the cutoff of the deformable body solution. These are shown in Figures 36 and 37.

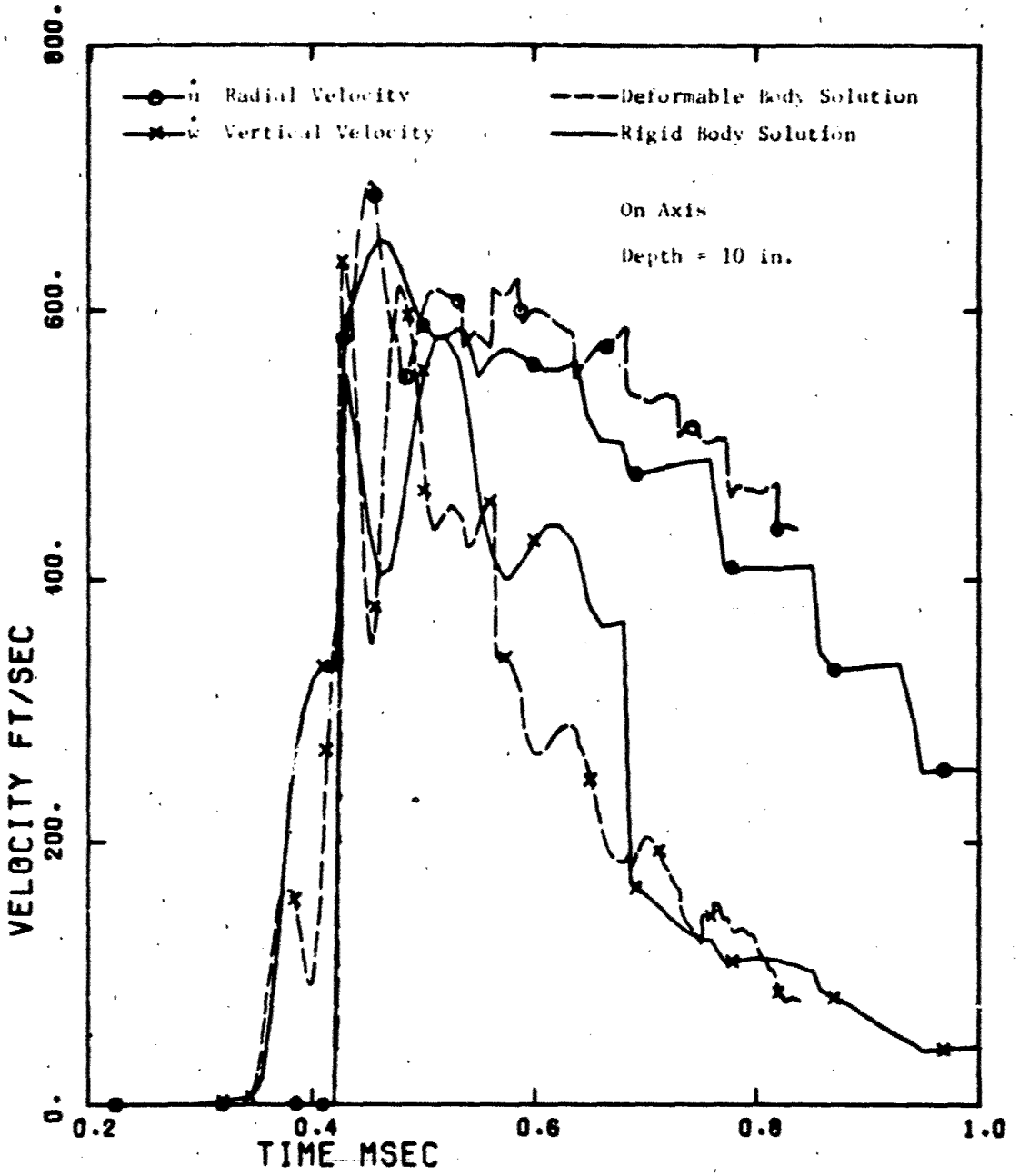

Figure 34. Comparison of Velocity Time Histories in Soil from Deformable Body and Rigid Body Solutions

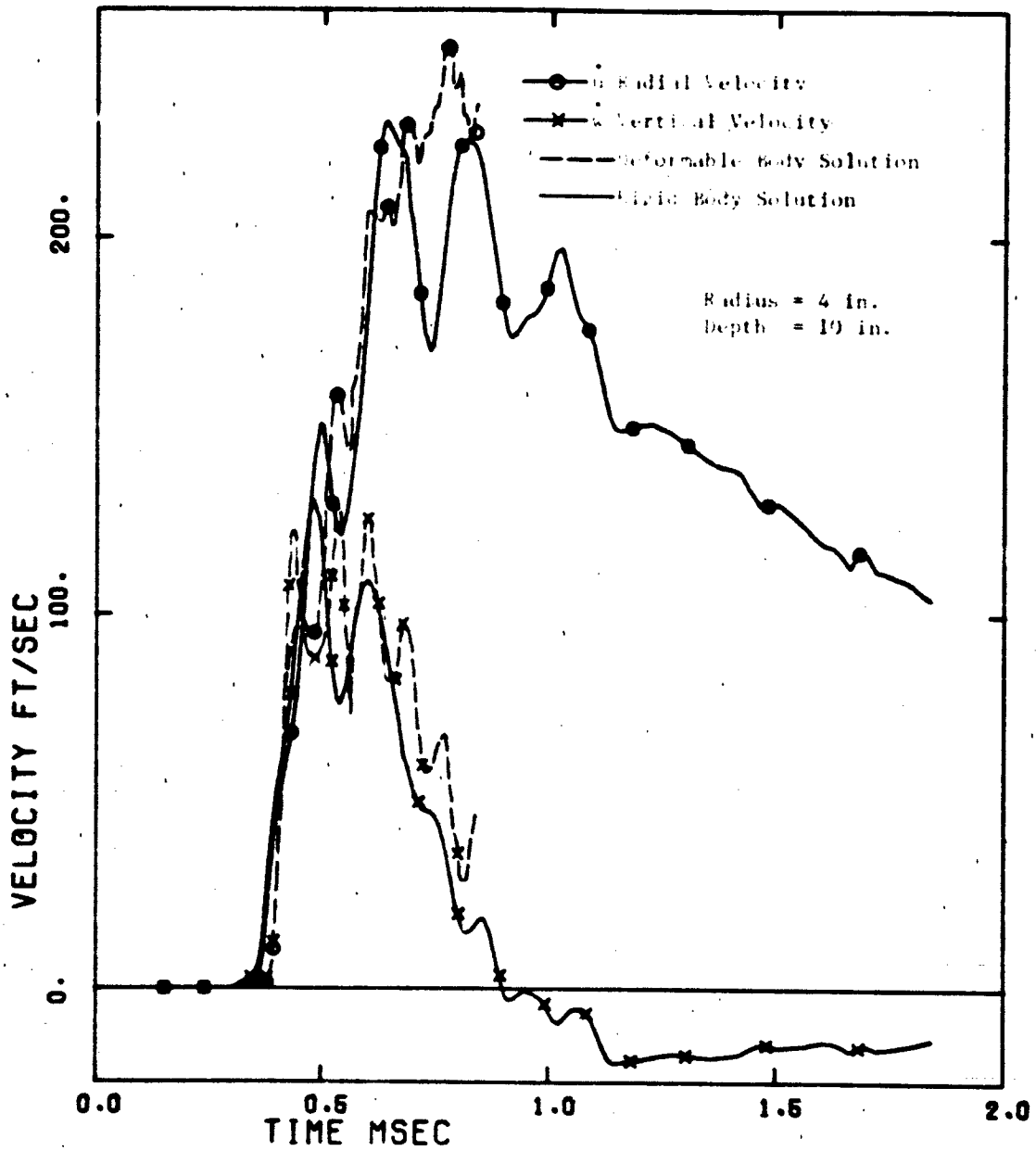

Figure 35. Comparison of Velocity Time Histories in Soil from Deformable Body and Rigid Body Solutions

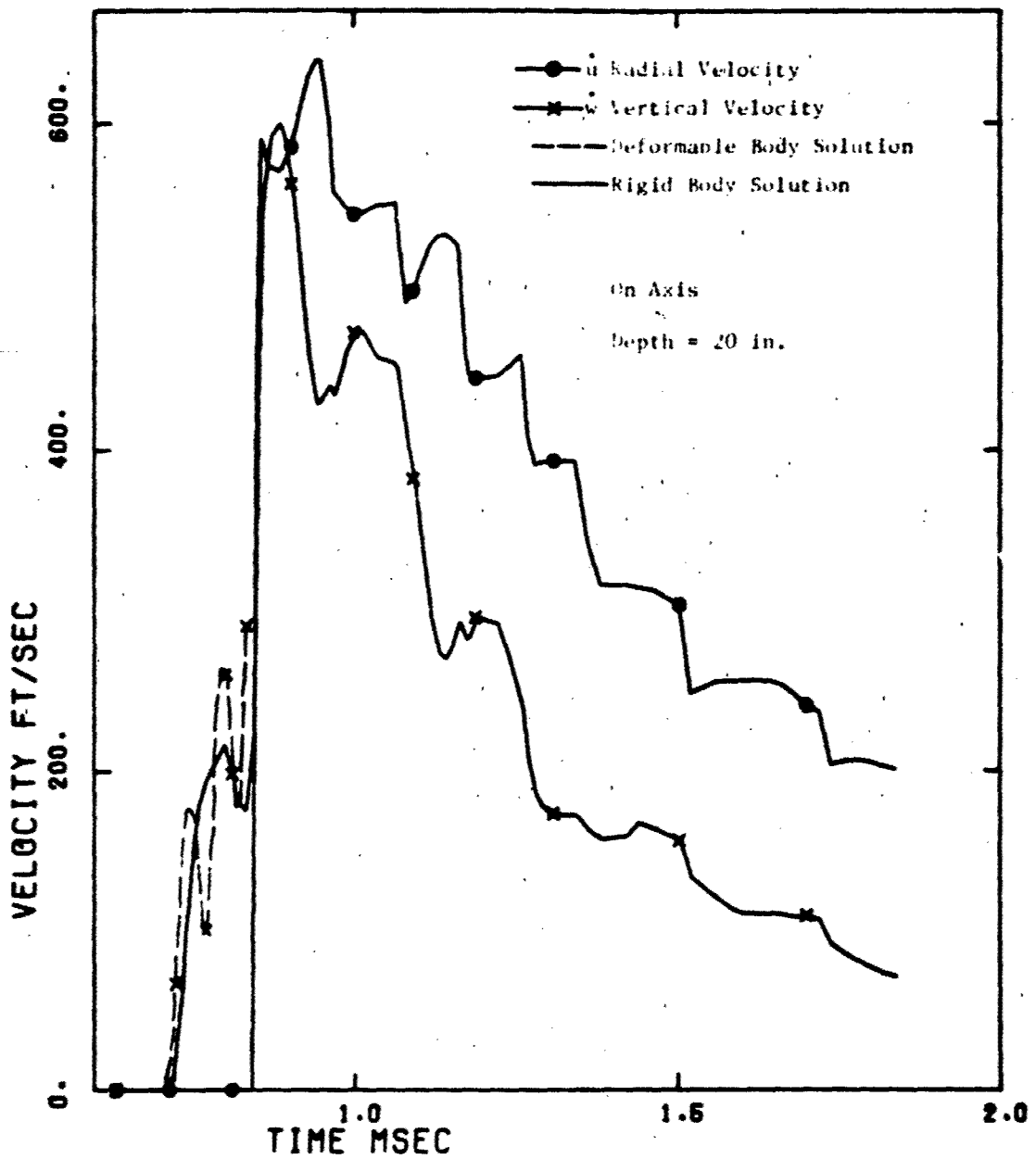

Figure 36. Comparison of Velocity Time Histories from Deformable Body and Rigid Body Solutions

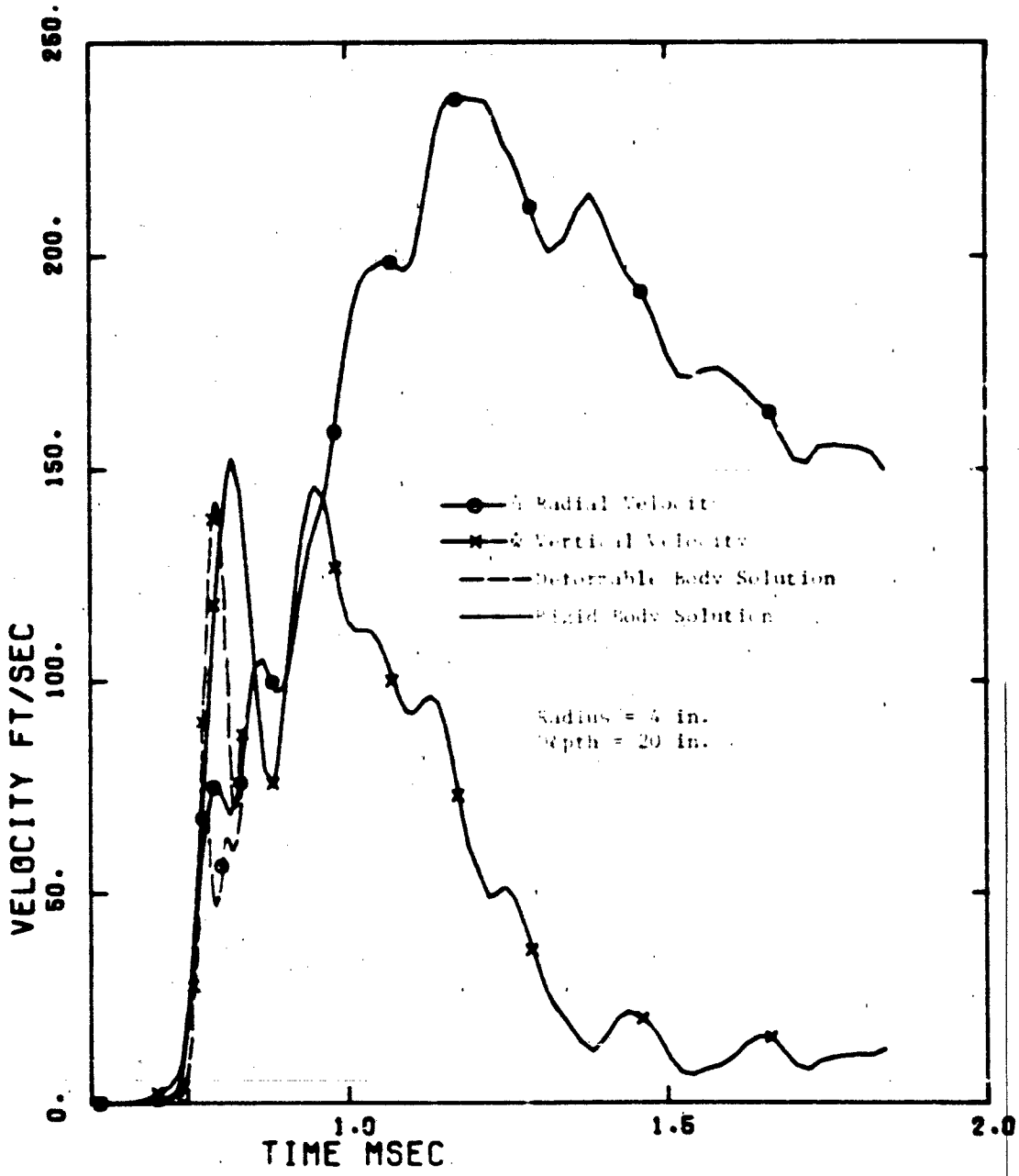

Figure 37. Comparison of Velocity Time Histories from Deformable Body and Rigid Body Solutions

SECTION VII

CONCLUSIONS AND RECOMMENDATIONS

The results of this study provide additional information with which to evaluate the role of finite-difference code calculations of earth penetration problems. The finite-difference approach appears to be very useful for analysis of certain aspects of these problems. It is unsuitable, or at least inefficient, for others.

7.1 RIGID BODY PENETRATIONS

Successful penetrator designs will generally experience only elastic deformations. (An exception might be a design with a sacrificial nose section.) It is therefore reasonable, and efficient, to analyze penetration by treating the projectile as a rigid body. Such analyses provide a practical method for:

- o Examining the interactions between projectile shape, basic target media properties, and impact velocity, (thereby providing analytical guidance for designing and evaluating improved projectile designs), and
- o Determining the external loading distributions on the projectile (thereby providing bases for analyzing the projectile response and internal design environment).

These types of analyses do not require computer solutions of complete deep penetration problems. They require only that the projectile travel far enough in a given

target medium to reach quasi-steady-state conditions. Such analyses should therefore be confined to those portions of a penetration event where the loading on the projectile is most severe, or where the loading changes significantly (e.g., during initial impact and embedment of the nose into the surface layer, and during passage between different geologic layers).

There are a number of improvements which should be made in the rigid body analysis technique. These include efficient rezoning procedures to correct grid distortion in the target medium near the penetrator surface, and the establishment of minimum zoning criteria to ensure reasonably accurate solutions. Both of these steps are being undertaken in a current program.

Because of the long computing times required, it is probably inefficient to use a finite-difference code to analyze complete deep penetration problems (i.e., from impact until the projectile comes to rest).

7.2 PROJECTILE RESPONSE

To analyze the response of the projectile, a solution of the penetration may be performed in which the projectile is treated as a deformable-body (such as was done in this study). However, finite-difference solutions of this type, in which the projectile deformation and the target deformation are treated [illegible], are time consuming due to the markedly different character of the projectile and target responses. Good spatial resolution is needed in the projectile in order to resolve structural details, and the wave speeds in typical projectile materials are relatively

high. These factors dictate small integration times steps. On the other hand, coarser spatial resolution and lower wave speed in the target media will normally permit much longer time steps.

Because of these differences in the integration time step and in the magnitudes of the distortions involved, it is more efficient to perform separate but coupled analyses of target penetration and of penetrator response. Thus, a rigid body analysis can first be performed of the penetration in the target media. From this rigid body solution, the penetration history and force loading, as they impose on the projectile surface, is determined. This information can then be used to drive a deformable body analysis of the stress wave response in the projectile itself.

Performing separate computations also allows the choice of taking either a finite-difference or a finite-element code analysis of the projectile response. As long as the strains are small and the material structure can be acceptably modeled, the finite element method may be more efficient.

7.2 NUMERICAL OSCILLATIONS

Severe numerical oscillations were experienced in the force applied to the projectile during the deformable body solution and during part of the rigid body solution. These are attributed to reinforcing synchronous interactions between the deformed finite computational grid and the strongly hysteretic nature of the soil model. This problem (which has been far less severe in other penetration analyses we have performed in less hysteretic media) was alleviated by

using a slightly canted, or pre-deformed grid. In strongly hysteretic media, considerable care needs to be taken in modeling the collapse of the porosity and the unloading behavior experienced in material moving around a projectile nose.

REFERENCES

1. M. L. Wilkins et al, "Progress Report on Light Armor Program", UCRL 50284, 1967

2a. M. H. Wagner, "Analytical Study of Penetration Mechanics", Rpt. 5030-2020-18, Shock Hydrodynamics, Inc., May 1969

2b. M. H. Wagner, "Analytical studies of Projectile Design and Performance", Rpt. 7384-06, Shock Hydrodynamics, Inc., August 1971

3. L. Thigpen, "Penetration of Projectiles into Continuous Earth Media", SC RR-72 0204, Sandia Laboratories, May 1972

4. M. H. Wagner, K. N. Kreyenhagen, and W. S. Goerke, "Numerical Analysis of DNA Earth Penetrator Experiment at DRES", DNA 3537F (CRT Report 2050-2), October 1974

5. Y. M. Ito, K. N. Kreyenhagen, G. L. Eggum, and W. S. Goerke, "Analysis of Dynamic Stresses Within a Terminal Delivery Vehicle During Penetration of a Hard Earth Target", CRT Report 2060-1 (in publication by WES)

6. M. L. Wilkins, "Calculation of Elastic-Plastic Flow", Lawrence Livermore Laboratory, UCRL-7322, Rev. 1, January 1969

7. D. S. Butler, U. S. Army Waterways Experiment Station, Vicksburg, Mississippi, personal communication

8. R. Hill, Mathematical Theory of Plasticity, Oxford, 1950

9. "Time Histories of Stresses, Velocities, and Displacements", (unpublished) Contract DACA39-74-C-0007, California Research & Technology, Inc., May 1975

APPENDIX A

MATERIAL MODELS

Material models for the two site layers were developed, based on the set of representative soil properties furnished by WES. Hysteretic elastic ideally plastic models using a Prandtl-Reuss (non-associated) flow rule were employed.

A non hysteretic elastic-perfectly plastic model was used for the steel projectile.

A.1 LAYER 1

A.1.1. Equation of State

The pressure is given by a Mie-Grüneisen equation:

$$P = F(\mu) + \Gamma \rho e$$

where e = specific internal energy

P = pressure

ρ = density

$\mu = \rho/\rho_0 - 1$

Γ = Grüneisen constant

The hydrostat, $F(\mu)$, is specified through a hysteretic model.

A.1.2 Loading Hydrostat

The loading hydrostat up to the point of void closure, μ_c, was fit from P vs μ data deduced from the loading curves of stress vs strain and stress difference vs

pressure. Beyond void closure, a well-behaved asymptotic-form is employed.

$$E = A\mu \qquad \mu \le 0$$

$$E = A\mu + B\left[\exp(\mu\alpha) - 1\right] \qquad 0 \le \mu \le \mu_c$$

$$E = E_c + K_{max}(\mu - \mu_c)$$

$$(K_{max} - K_c) * \left[1 - \exp\frac{\mu_c}{\mu^*}\right] \qquad \mu \ge \mu_c$$

The values of the constants are:

$A = 2.9211 \times 10^{-4}$ Mb	$K_{max} = .68946$ Mb
$B = 2.3003 \times 10^{-4}$ Mb	$\alpha = 302.27$
$E_c = 2.0659 \times 10^{-4}$ Mb	$\beta = 1.1$
$\gamma = 1.2$	$\mu_c = .0504$
$K_c = .046131$ Mb	$\mu^* = .25$
	$\rho = 1.9222$ gm/cm^3 (120 lb/ft^3)

A.1.3 Shear Modulus - Loading

The shear modulus function for loading was determined from a graphical assessment of the variation of Poisson's ratio along the unloading stress path (stress difference vs pressure) and the bulk modulus (as derived from the hydrostat equations). A maximum value equal to the unloading shear modulus was imposed to prevent energy generation.

$$G_{load} = \text{Min}\left[\frac{3B(1-2\nu)}{2(1+\nu)}, G_{unload}\right]$$

where

$$B = (\mu+1)\frac{dF_{load}}{d\mu}\left(\mu\right)$$

$$\nu = .5 - .25 \exp\left(\frac{-\mu}{.033}\right)$$

Initial values of the bulk modulus, the shear modulus, the constrained modulus, Poisson's ratio, and the dilatational sound speed from the model are:

B_o = 4,237 psi $\qquad \nu_o$ = .25

G_o = 2,542 psi $\qquad c_o$ = 542.6 ft/sec

M_o = 7,626 psi

A.1.4 Unloading Model

In the hysteretic region, $\mu<\mu_c$, a model giving a fan of constant slope P-μ unloading paths was used (slopes are a function of μ_{max}):

$$F = F_{max} + K(\mu-\mu_{max}) \qquad \mu_{max}<\mu_c$$

$$F = F_c + K_c(\mu-\mu_c) \qquad \mu_{max}\geq\mu_c$$

The unloading bulk modulus varied from a minimum of 100 ksi to a maximum of 702.8 ksi. (The maximum corresponds to the bulk modulus for loading at void closure.) The unloading bulk

modulus was made a function of the maximum compression, μ_{max}. A constant value for the unloading shear modulus was assumed. The initial Poisson's ratio for unloading was the same as for loading, $\nu_0 = .25$, giving $G_{unload} = 60$ ksi. In the first of the above equations, P_{max} is the hydrostat loading pressure corresponding to μ_{max} and K is a function given by:

$$K = \frac{B_1 + B_2 \exp(b\mu_{max}) - 1}{\mu_{max} + 1} \qquad \mu_{max} < \mu_c$$

The constants, as determined from the given unload paths, are:

$$B_1 = 6.8946 \times 10^{-3} \text{ Mb}$$

$$B_2 = 6.9416 \times 10^{-7} \text{ Mb}$$

$$b = 218.25$$

For $\mu > \mu_c$, unloading is assumed to be reversible (i.e., it follows the load path).

Hydrostatic tension is limited by imposing a minimum value of pressure: $P_{min} = 10$ psi.

A.1.5 Failure Surface

A yield function $Y(P)$ was fit to the failure envelope supplied, where $Y = \sqrt{3J_2}$ at failure. The functions derived are:

$$Y = 3.4473\times10^{-6} + .48564P - 2.7715\times10^{5}P^2 \qquad P<0$$

$$Y = 1.241\times10^{-5} - 1.757\times10^{6}(4.8263\times10^{-5} - P)^{2.015}$$

$$0 \le P \le 4.8263\times10^{-5}$$

$$Y = 1.241\times10^{-5} \qquad 4.8263\times10^{-5} \le P \le 1.3789\times10^{-3}$$

$$Y = 1.241\times10^{-5} + .01025\,(P - 1.3789\times10^{-3})$$

$$P \ge 1.3789\times10^{-3}$$

Here the units for Y and P are Mb. Plots of the failure surface are included in the following set of figures.

A.1.6 Comparative Results

Plots of stress vs strain, stress-difference vs pressure, and pressure vs volumetric strain for uniaxial strain load-unload paths computed with the model, along with the WES curves, are shown in Figure 3 in the text, and in Figures A-1 to A-3 in this appendix. Plots of the Hugoniot and hydrostat up to high pressures (50 kb) are shown in Figure A-4.

A.2 LAYER 2

Due to the anticipated low stress environment, the pressures for Layer 2 were taken directly from the hydrostat, with no energy contribution.

A.2.1 Loading Model

The following equations were deduced for the loading hydrostat:

$$P = a\mu \qquad \mu \le 0$$

$$P = a\mu + \frac{b}{c-\mu} + \frac{b}{c} \qquad 0 < \mu \le \mu_c$$

$$P = P_c + K_{max}(\mu - \mu_c) - (K_{max} - K_c)\mu^* \left[1 - \exp\frac{\mu_c - \mu}{\mu^*}\right] \qquad \mu > \mu_c$$

The values of the constants are:

$a = 5.7348 \times 10^{-5}$ Mb	$K_c = .048263$ Mb
$b = 1.37095 \times 10^{-8}$ Mb	$K_{max} = .689465$ Mb
$c = 6.75577 \times 10^{-5}$ Mb	$P_c = 5.7604 \times 10^{-5}$ Mb
$\mu^* = .23$	$\rho_o = 2.0503$ gm/cm^3 (128 lb/ft^3)
$\mu_c = .006188$	

The shear modulus for loading was specified to be constant at a value of 20 ksi.

Initial values of the bulk modulus, the constrained modulus, Poisson's ratio, and the dilatational sound speed from the model are:

$B_o = 83.18$ ksi	$\nu_o = .389$
$M_o = 109.8$ ksi	$c_o = 1{,}994$ ft/sec

A.2.2 Unloading Model

In the hysteretic region, $\mu < \mu_c$, a model giving a fan of constant slope P, unloading paths was used (slopes are a function of μ_{max}):

$$P = P_{max} + K(\mu - \mu_{max}) \qquad \mu_{max} < \mu_c$$

$$P = P_c + K_c(\mu - \mu_c) \qquad \mu_{max} \geq \mu_c$$

In this region the unloading bulk modulus varies from a minimum of 200 ksi to a maximum of 700 ksi, equal to the bulk modulus for unloading at void closure. A constant value of 60 ksi was used for the unloading shear modulus. K is a function given by:

$$K = K_0 + K_1 P_{max} \qquad \mu_{max} < \mu_c$$

where P_{max} is obtained from the loading hydrostat equations evaluated at μ_{max}. The constants, as determined from the given unload paths, are:

$$K_0 = .013789 \text{ Mb}$$

$$K_1 = .048263 \text{ Mb}$$

For $\mu \geq \mu_c$, unloading is assumed to be reversible and follows the load path.

Hydrostatic tension is limited by imposing a minimum value of pressure: $P_{min} = -100$ psi.

A.2.3 Failure Surface

A yield function $Y(P)$ was fit to the failure envelope suggested, where $Y = \sqrt{3J_2}$ at failure. The functions derived are:

$$Y = 1.7237\times10^{-5} + 2.2569P - 3.5270\times10^{4}P^{2}$$

$$-6.8946\times10^{-6} \le P \le 0$$

$$Y = 5.171\times10^{-5} - 1.4[illegible]0\times10^{9}(4.8263\times10^{-5}-P)^{3.159[illegible]}$$

$$0 < P \le 4.8263\times10^{-5}$$

$$Y = 5.171\times10^{-5} \qquad 4.8263\times10^{-5} < P \le 2.4131\times10^{-3}$$

$$Y = 5.171\times10^{-5} + .015385(P-2.4131\times10^{-3}) \qquad P > 2.4131\times10^{-3}$$

Here the units for Y and P are Mb.

A.2.4 Comparative Results

Plots of stress vs strain, stress-difference vs pressure, and pressure vs volumetric strain for uniaxial strain load-unload paths computed with the model, along with the WES curves, are shown in Figure 4 in the text, and in Figures A-5 and A-6 in this appendix.

A.3 STEEL

An existing equation of state for iron was employed.* Appropriate mechanical and strength properties for the steel alloy of the penetrator were then added to the model.

*M. H. Wagner, *Analytical Studies of Projectile Design and Performance*, Shock Hydrodynamics Report 7584-06, August 1971

The following properties were assumed:

Normal density, ρ_0:	7.84 gm/cm^3	(489 lb/ft^3)
Bulk modulus, K_0:	1.686 Mb	(2.445x10^7 psi)
Shear modulus, G:	.83 Mb	(1.204x10^7 psi)
Yield strength, Y:	.0034473 Mb	(50,000 psi)

The shear modulus was assumed to be constant. The bulk modulus varies through the equation of state. A conventional von Mises yield model was employed; i.e., states are elastic for $\sqrt{3J_2} < Y$ constant. Hydrostatic tension was limited by imposing a minimum value of pressure:

$$P_{min} = -\frac{1}{3}Y$$

With this condition, the tensile stress is limited to a value $-Y$.

The low-pressure (sub-transition) portion of the previously formulated equation of state of iron covers the range of interest and is given by:

$$P = a_1\mu(1-\tfrac{1}{2}\mu) + \gamma_0 e \qquad \mu<0$$

$$P = (a_1\mu + a_2\mu^2 + a_3\mu^3)(1-\tfrac{1}{2}\mu) + \gamma_0 e \qquad 0\leq\mu\leq\mu_1$$

The values of the constants are:

a_1 = 1.686 Mb	γ_0 = 1.81
a_2 = 7.1889 Mb	μ_1 = .06717
a_3 = 70.334 Mb	

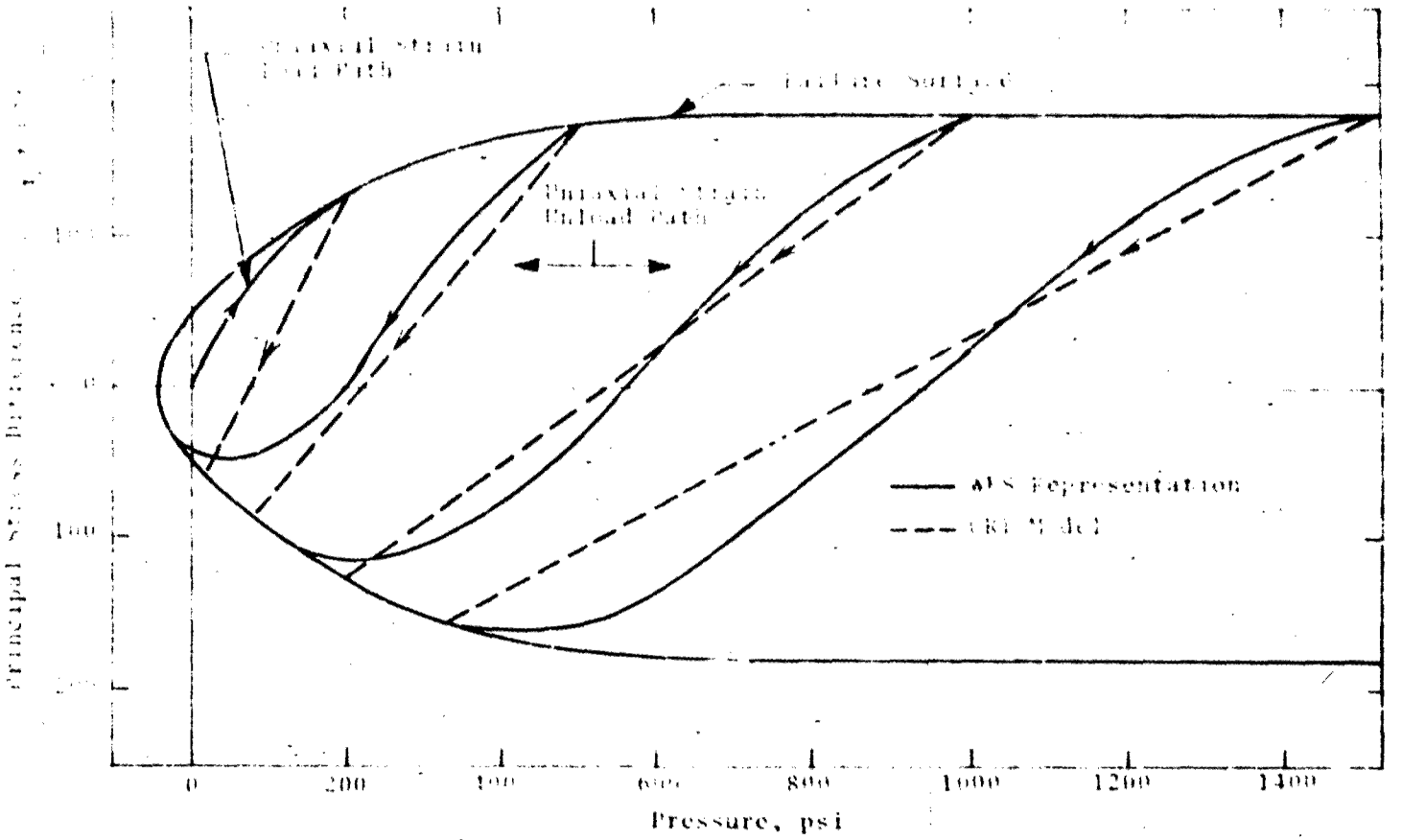

Figure A 1. Uniaxial Strain Stress Paths and Failure Surface for Layer 1

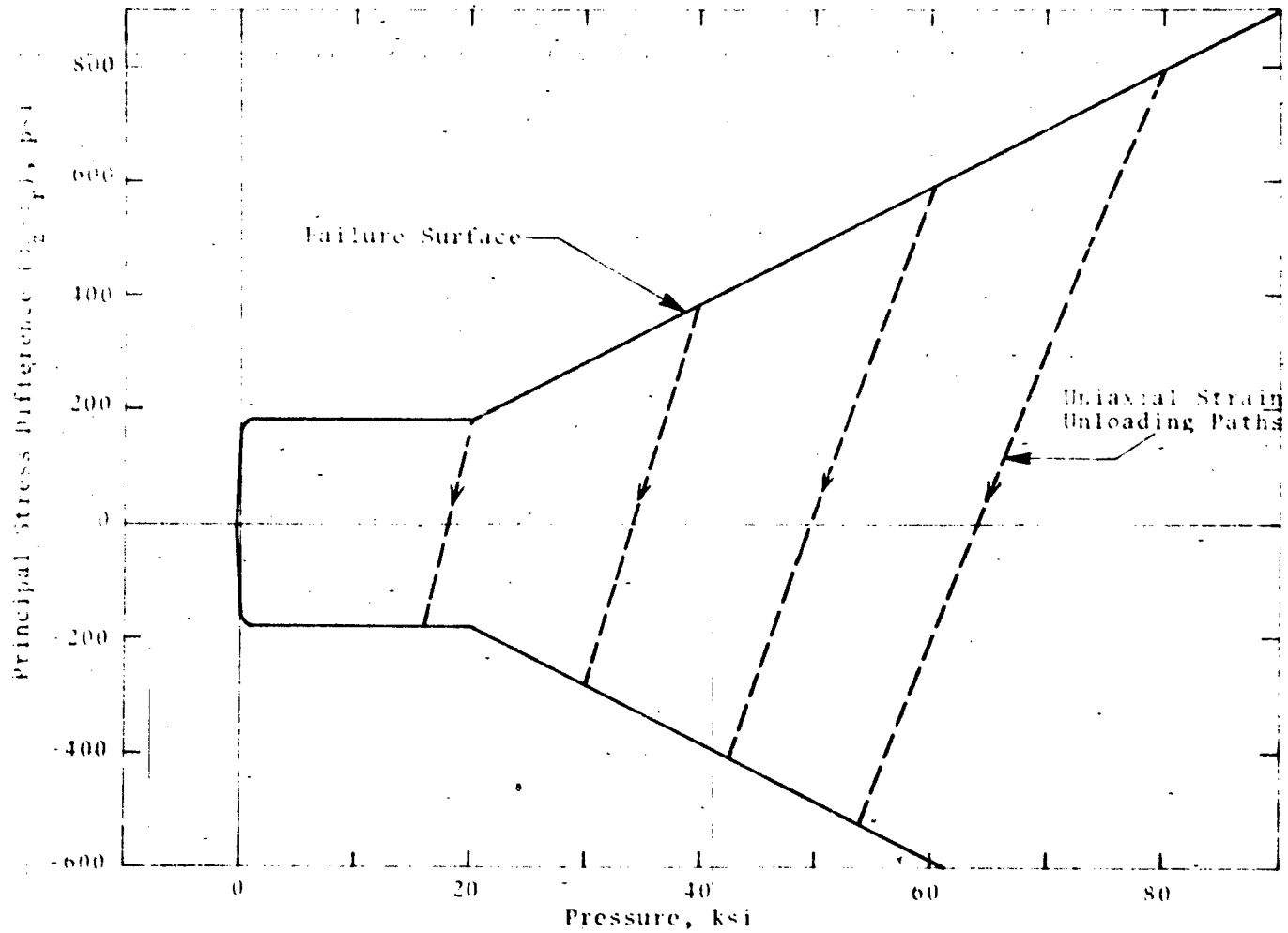

Figure A-2. Uniaxial Strain Unloading Paths and Failure Surface in High-Pressure Region for Layer 1

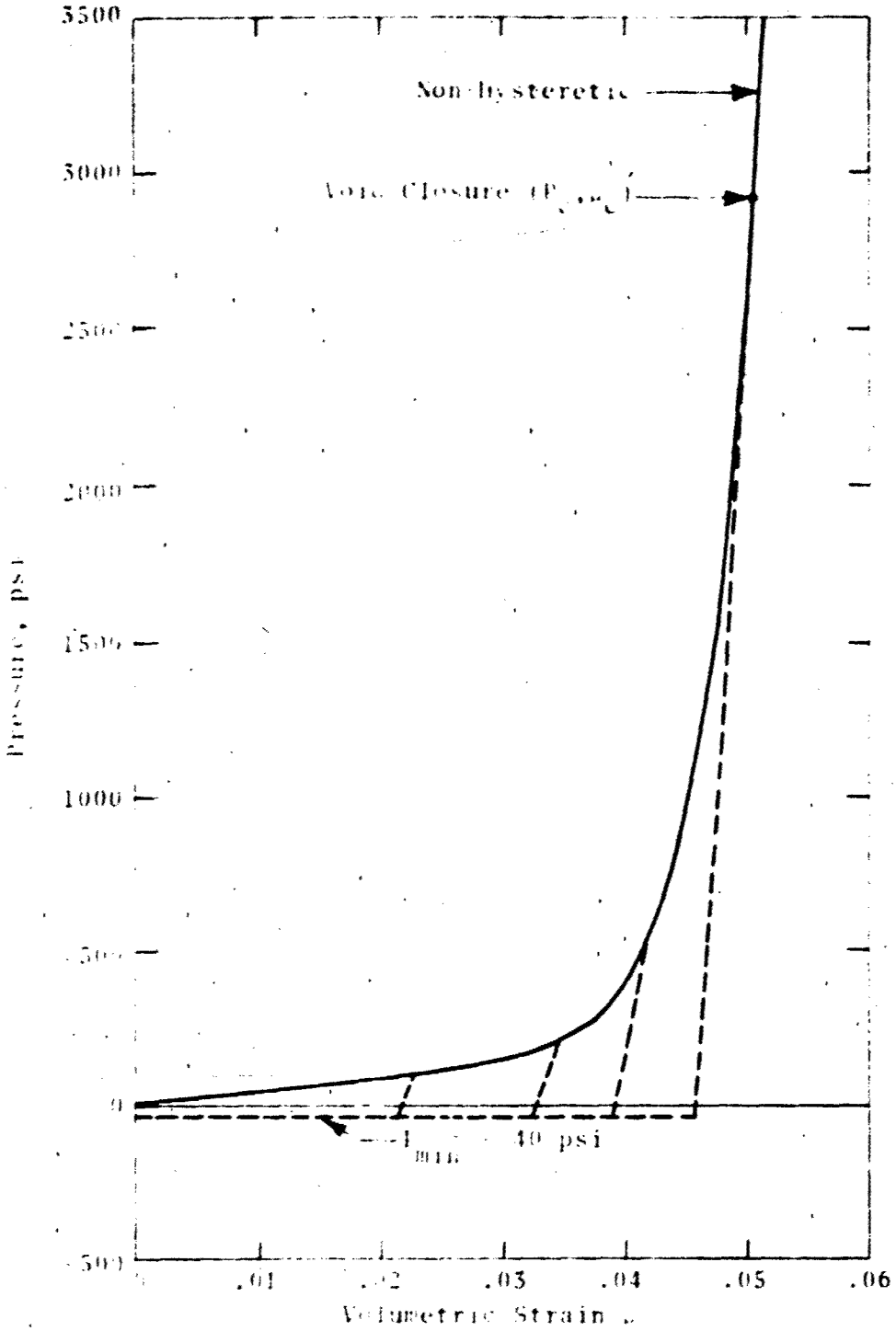

Figure A 5. Hydrostatic Load Unload Curves for Layer 1

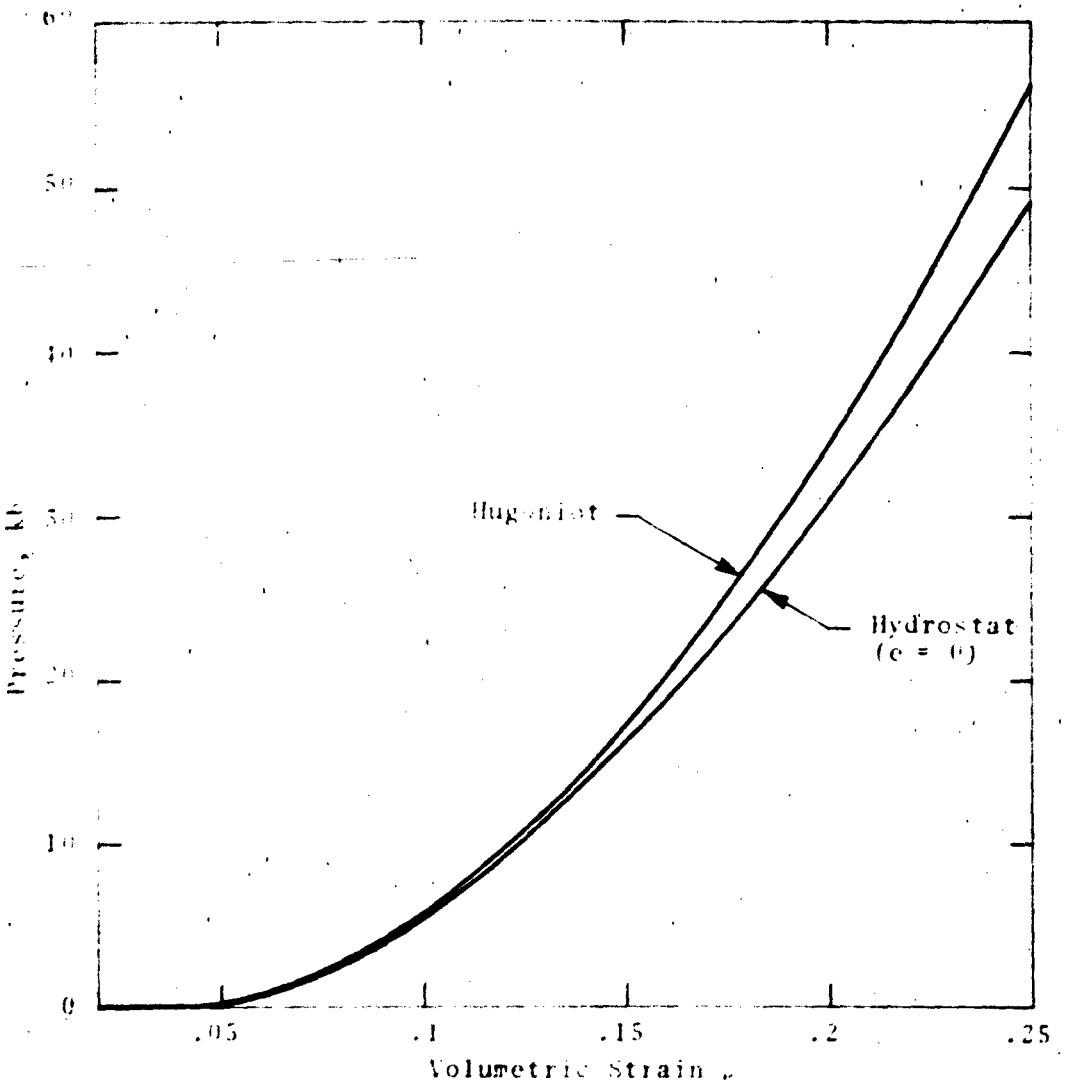

Figure A-4. Hugoniot and Loading Hydrostat for Layer 1

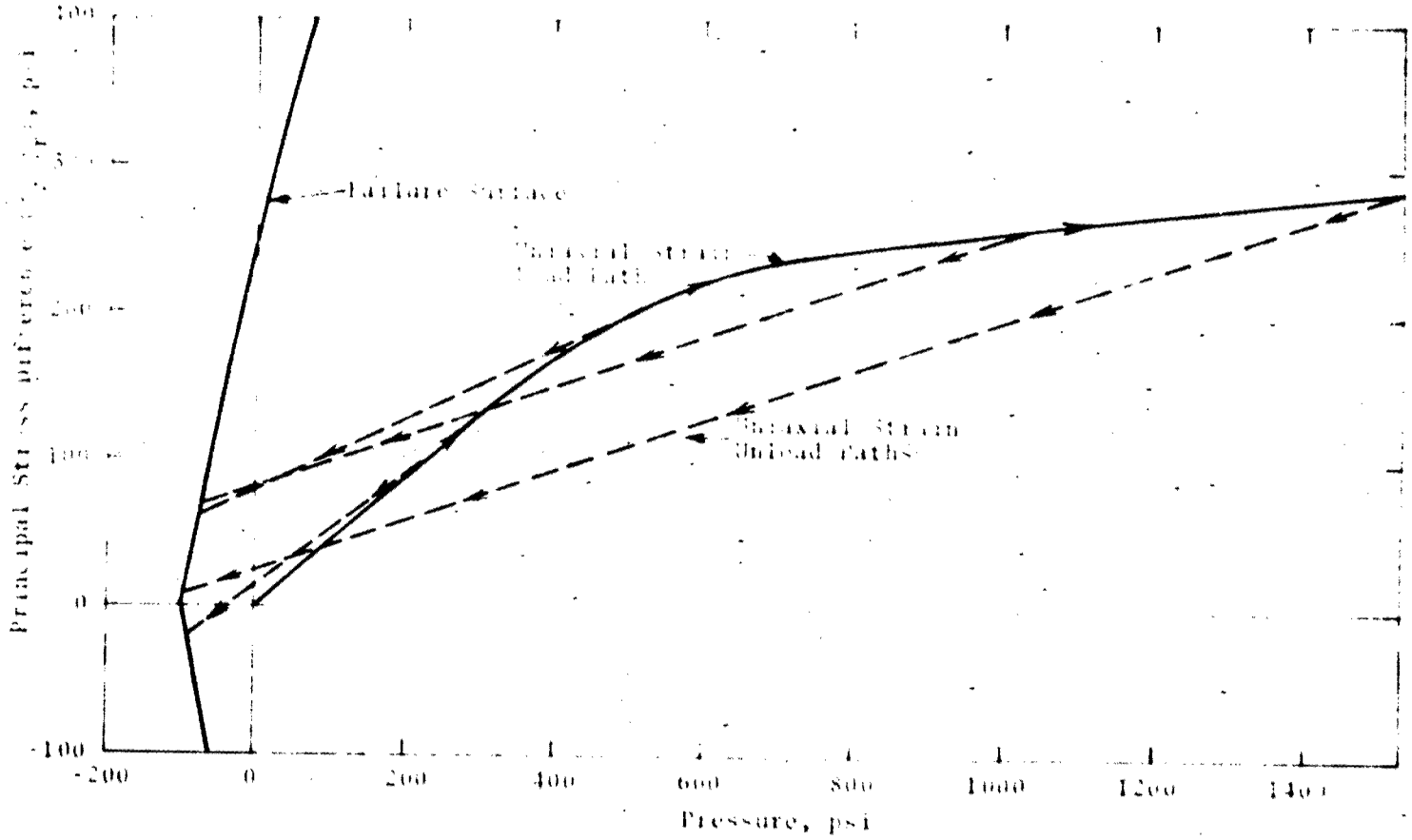

Figure A-5. Triaxial Strain Stress Paths for Layer 2

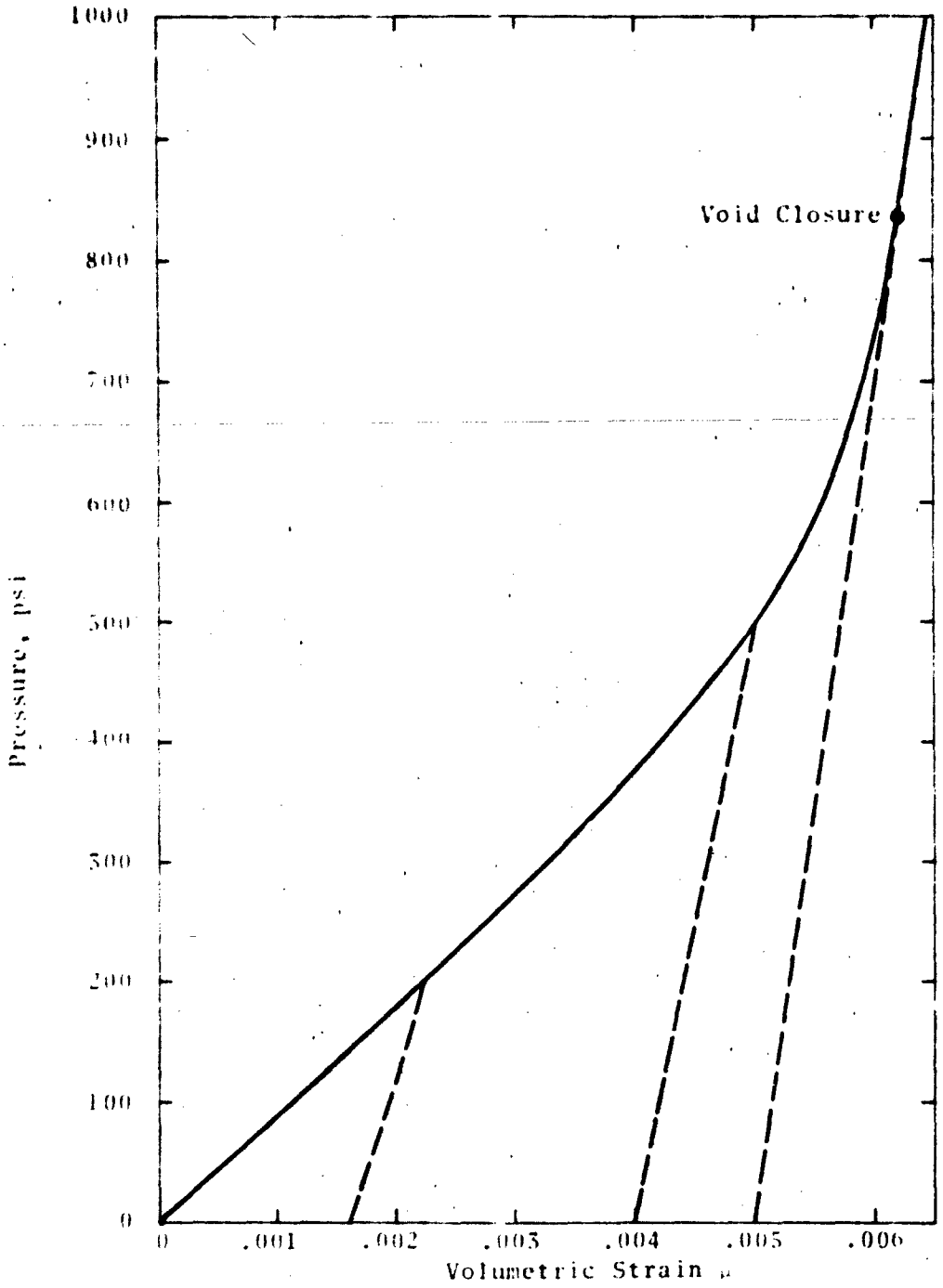

Figure A-6. Hydrostatic Load-Unload Curves for Layer 2

APPENDIX B

DISTORTION, VELOCITY, AND PRINCIPAL STRESS FIELD PLOTS - DEFORMABLE-BODY SOLUTION

A series of field plots of the computational grid, particle velocities, and principal stresses which illustrate the projectile and soil response during the deformable-body solution were prepared. These are shown for the following penetration depths and times.

Depth (in.)	Time (μ-sec)	Figure No. of Plot for: Distortion (Grid)	Velocity	Stress
.56	23.3	B-1	B-2	B-3
1.86	77.4	B-4		
3.07	128.1	B-5		
		B-6 (Rezone)		
5.04	210.1			B-7
6.33	263.9	B-8	B-9	B-10
		B-11 (Rezone)		
9.84	411.0	B-12	B-13	B-14
15.29	638.8	B-15	B-16	
18.06	754.7	B-17		
20.03	837.4	B-18	B-19	B-20

The velocity vector field plots show the direction and magnitude of the particle velocity at each lattice point in the computing grid.

In the stress field plots, the principal components of the stress tensor at each cell use the conventions:

The magnitude of the two principal stresses in the r-z plane are plotted in their corresponding principal directions. The third principal stress (in the azimuthal direction) is plotted along the line bisecting the other two principal directions. Vectors pointing to the right are compressive, to the left, tensile. An example of how a stress tensor is plotted is sketched below:

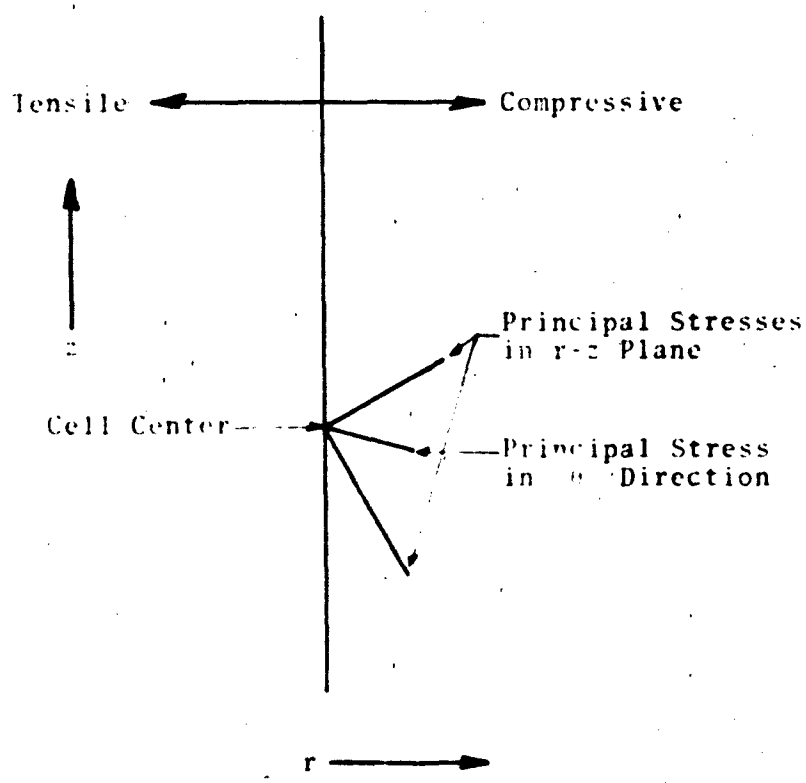

The first three figures of the grid (B-1, B-4, and B-5) show the initial entry of the penetrator into the top surface of the soil. A local rezone is required, as shown in Figure B-6, when the surface grid point contacts the penetrator surface (see Figure B-5).

In Figure B-7, the stress loading of the projectile nose after 5" penetration is seen. Note the strong vertical orientation of the stress vectors, due to the free surface at the periphery.

Figure B-11 shows another rezone which was performed to re orient the grid. A small portion of the distended soil that was flying off was also removed at this time.

Figures B 10 and B-14 show a buildup of radial and hoop tension along the lower end of the slug and a high vertical compressive stress in the thin section connecting the nose and the slug.

The detachment of the soil from the penetrator and hole formation may be seen in Figures B-17 and B-18.

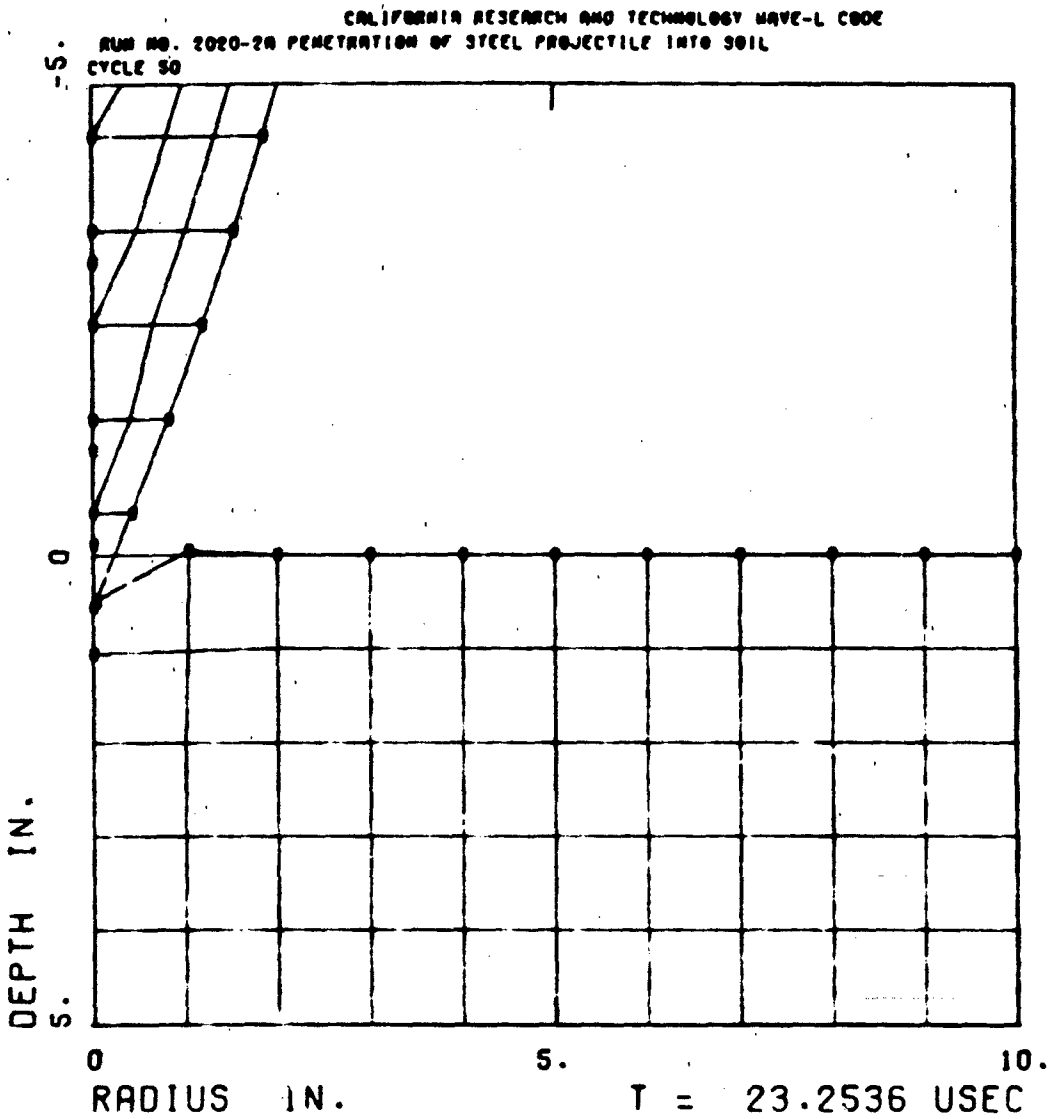

Figure 8-1. Grid Configuration with Projectile at .56 In. Depth

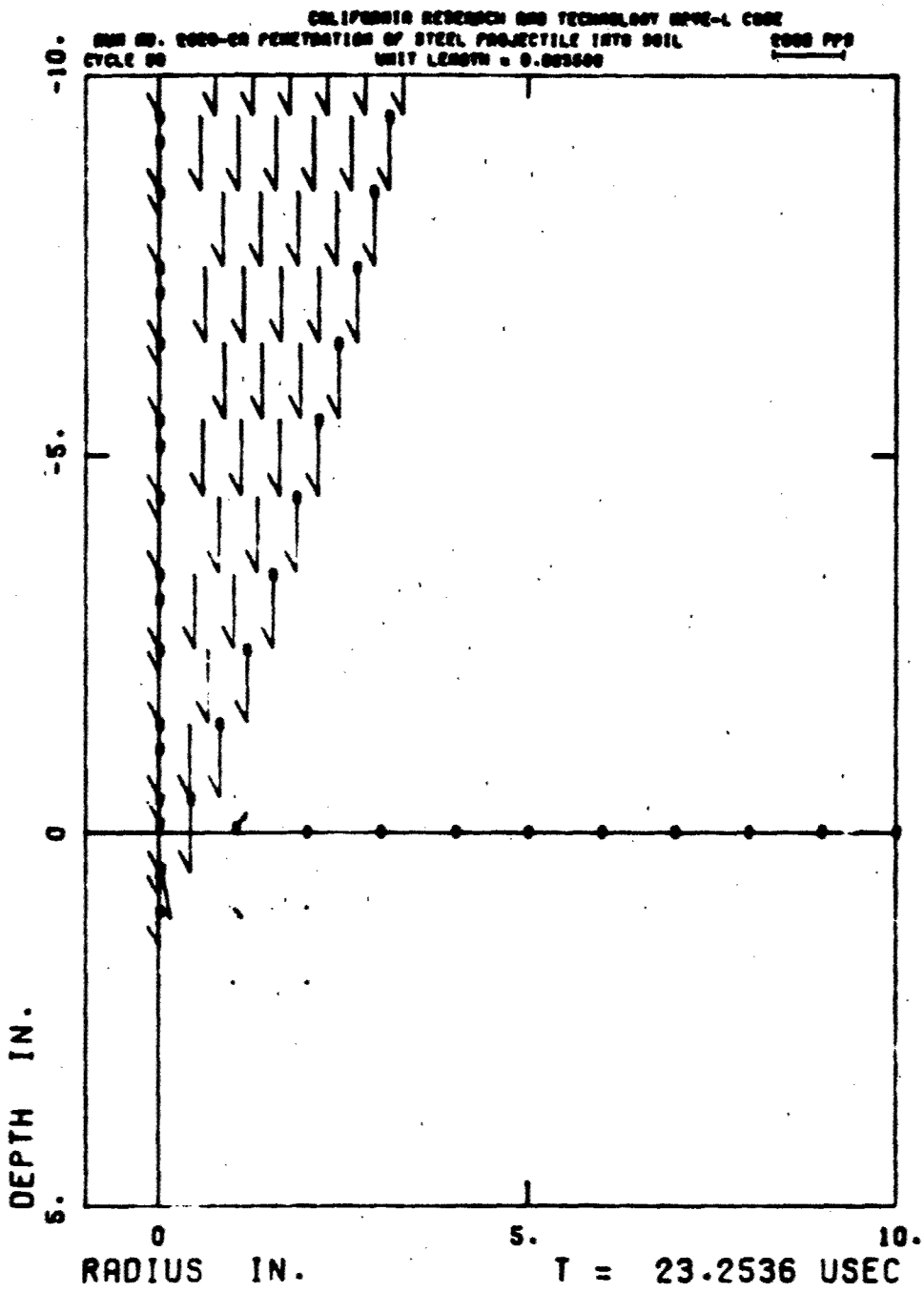

Figure B-2. Particle Velocity Field with Projectile at .56 in. Depth

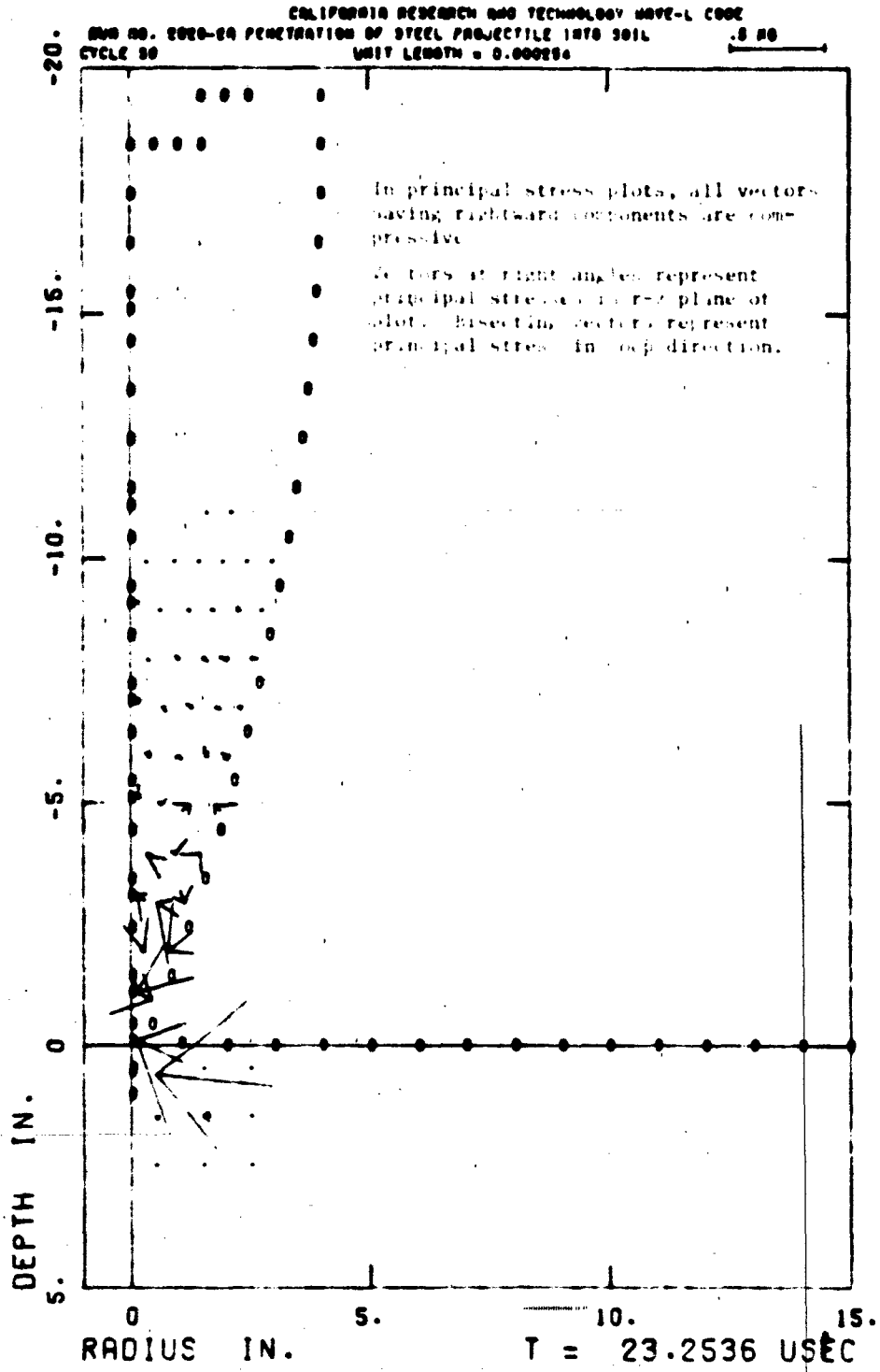

Figure [illegible]. Principal Stress Field with [illegible] at .56 in. Depth

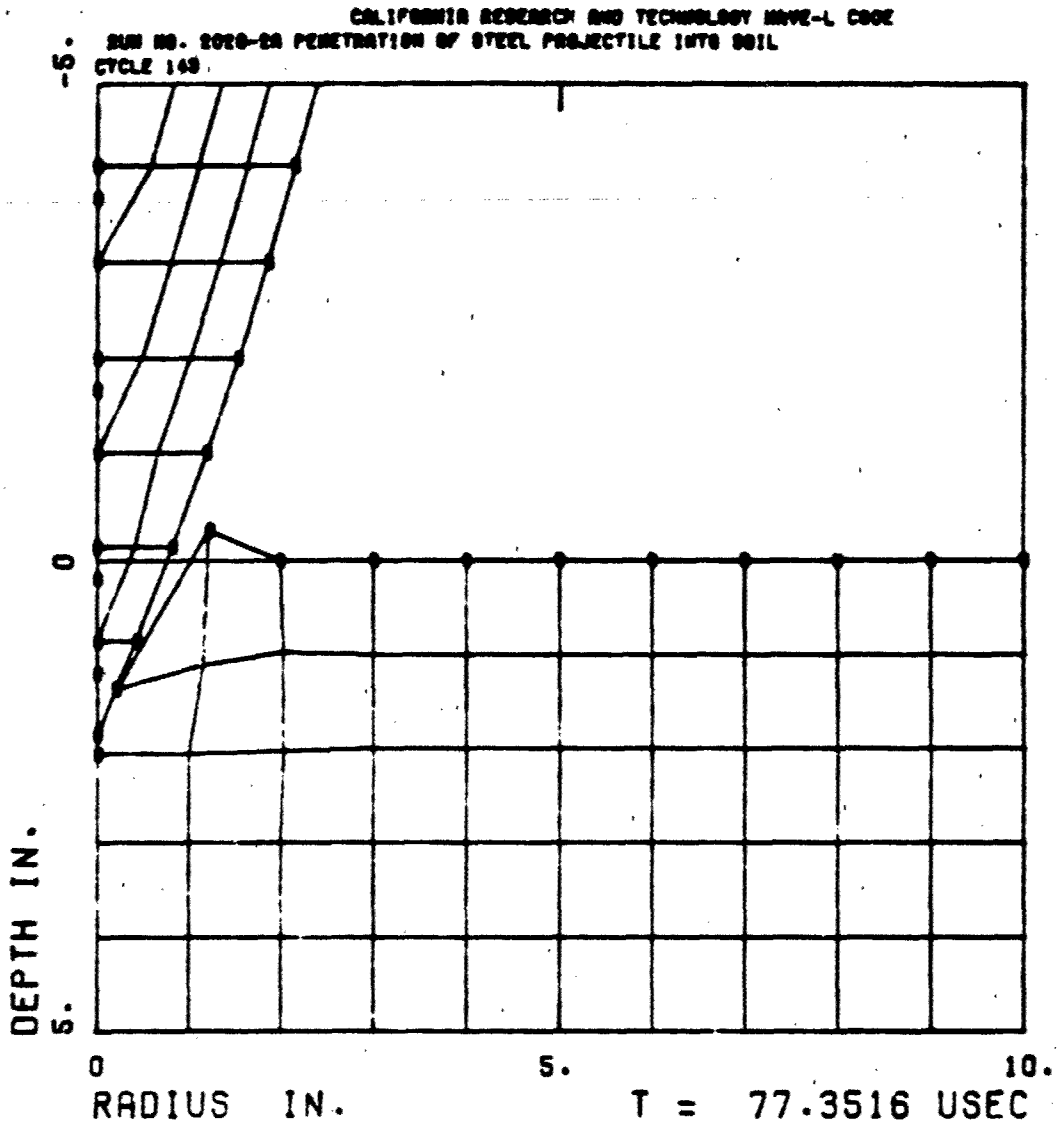

Figure 6-4. Grid Configuration with Projectile at 1.86 in. Depth

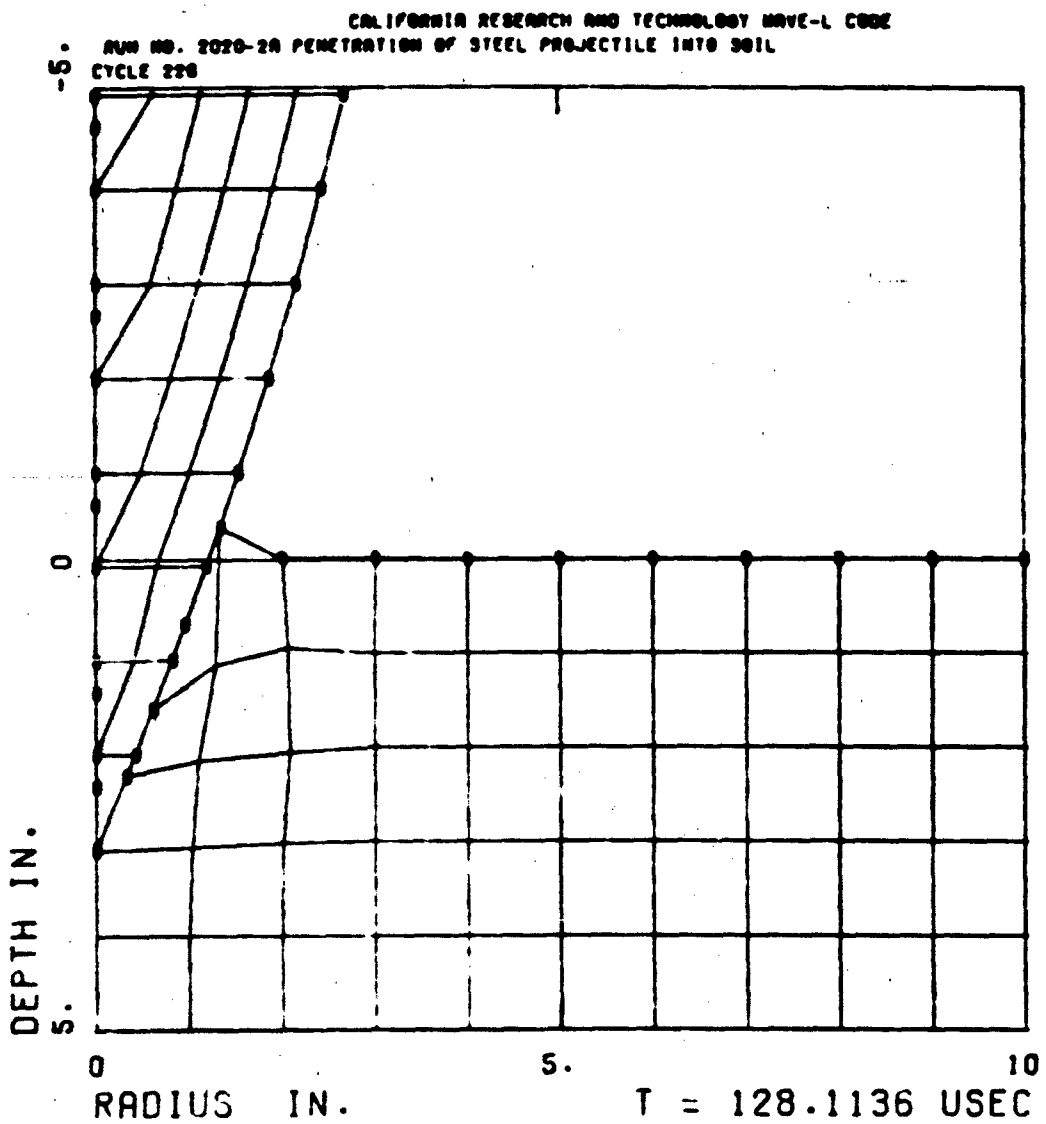

Figure B-[illegible] Grid Configuration with Projectile at 3.07 in. Depth

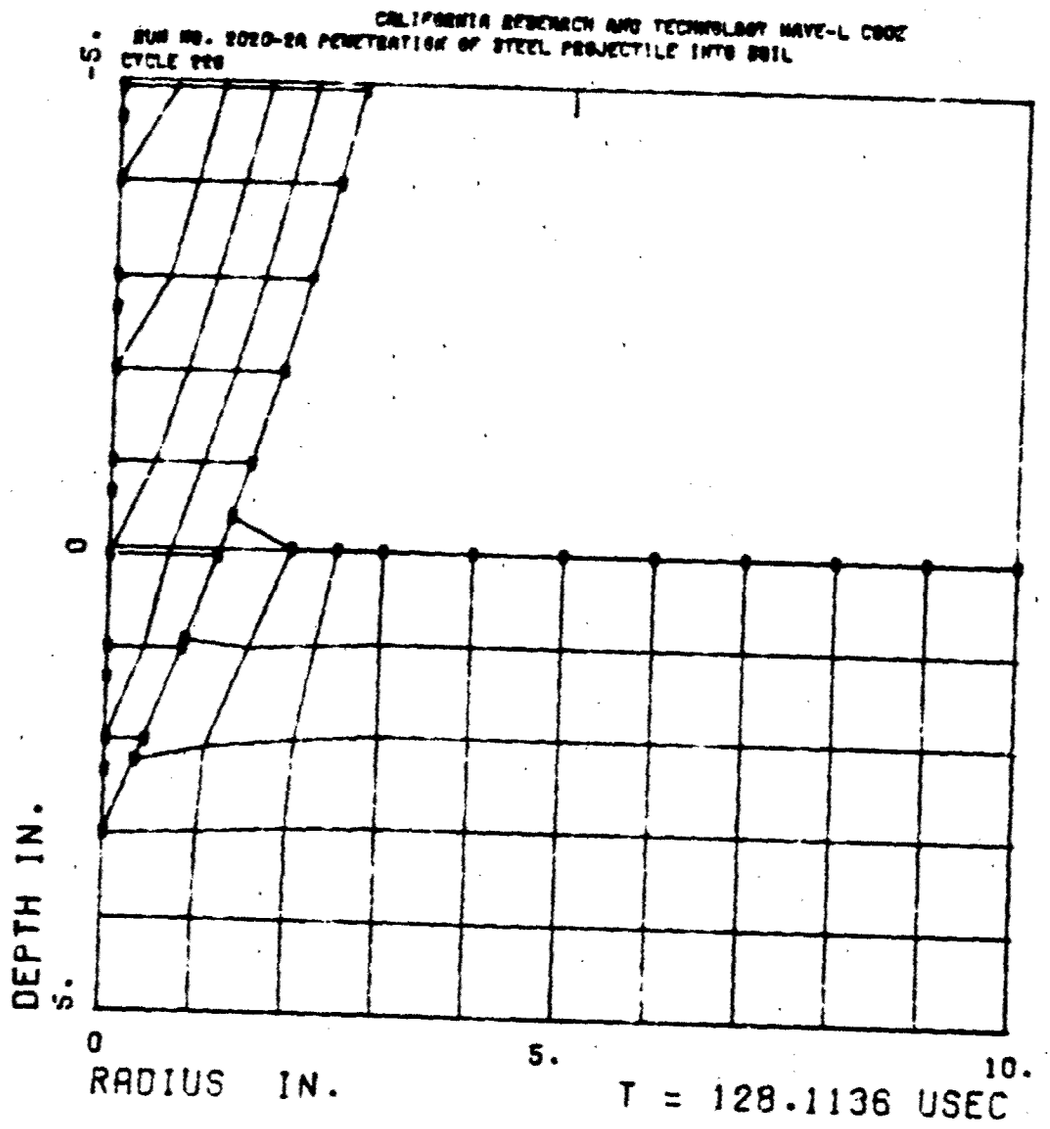

Figure [illegible]. [illegible] Configuration following [illegible]

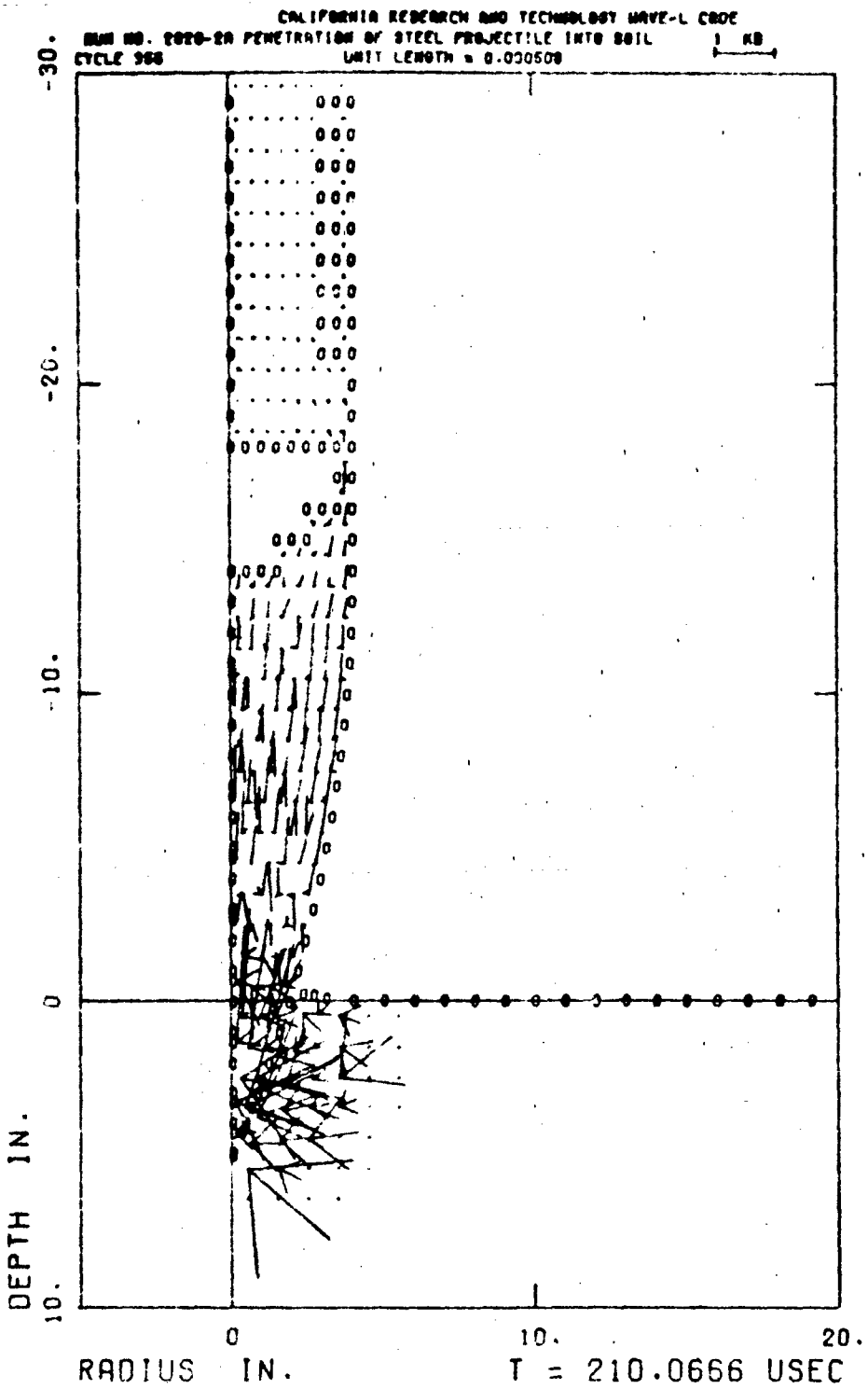

[illegible] at 5.04 in. Depth

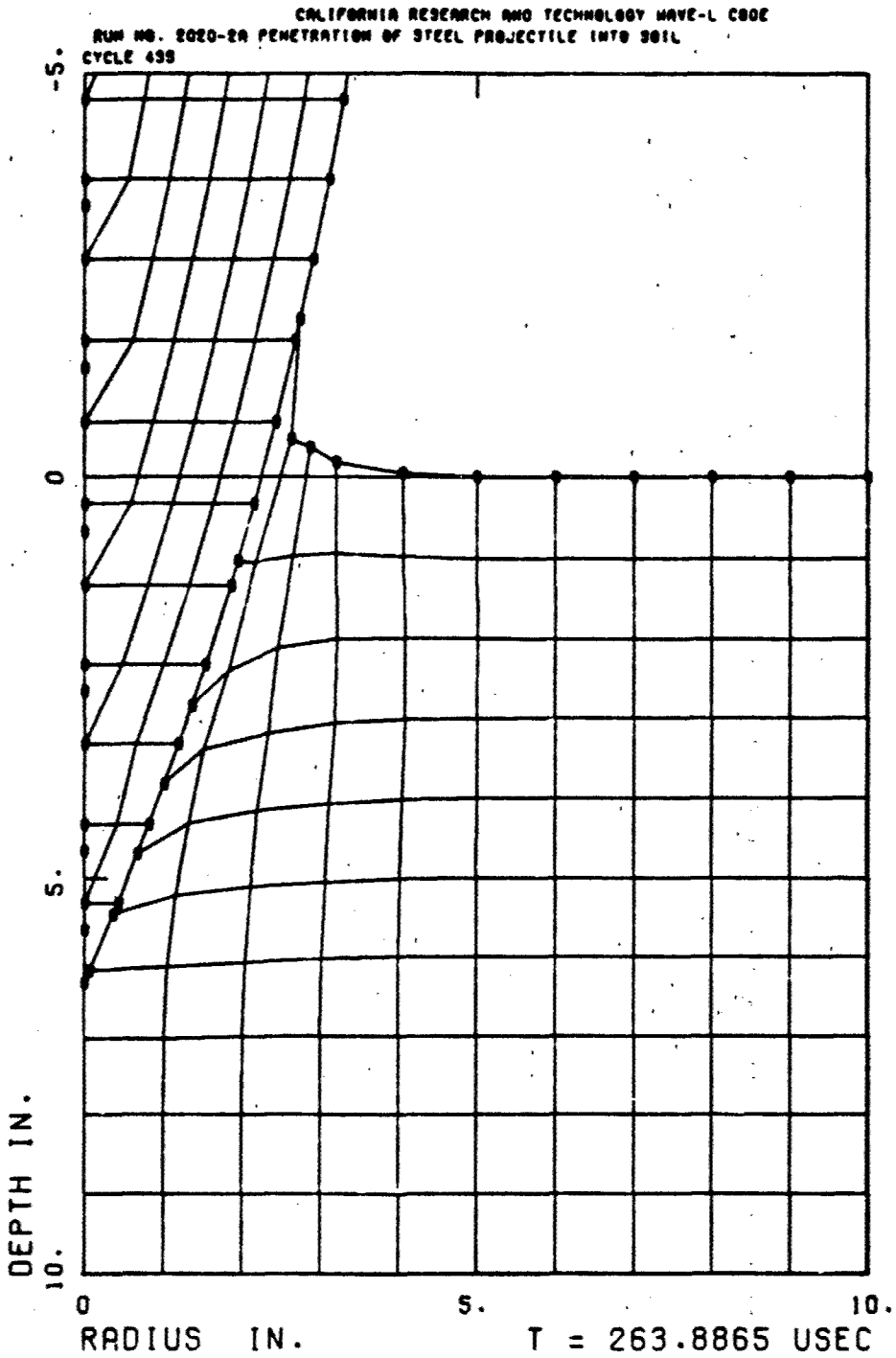

Figure B-8c. Grid Configuration with Projectile at 6.33 in. Depth

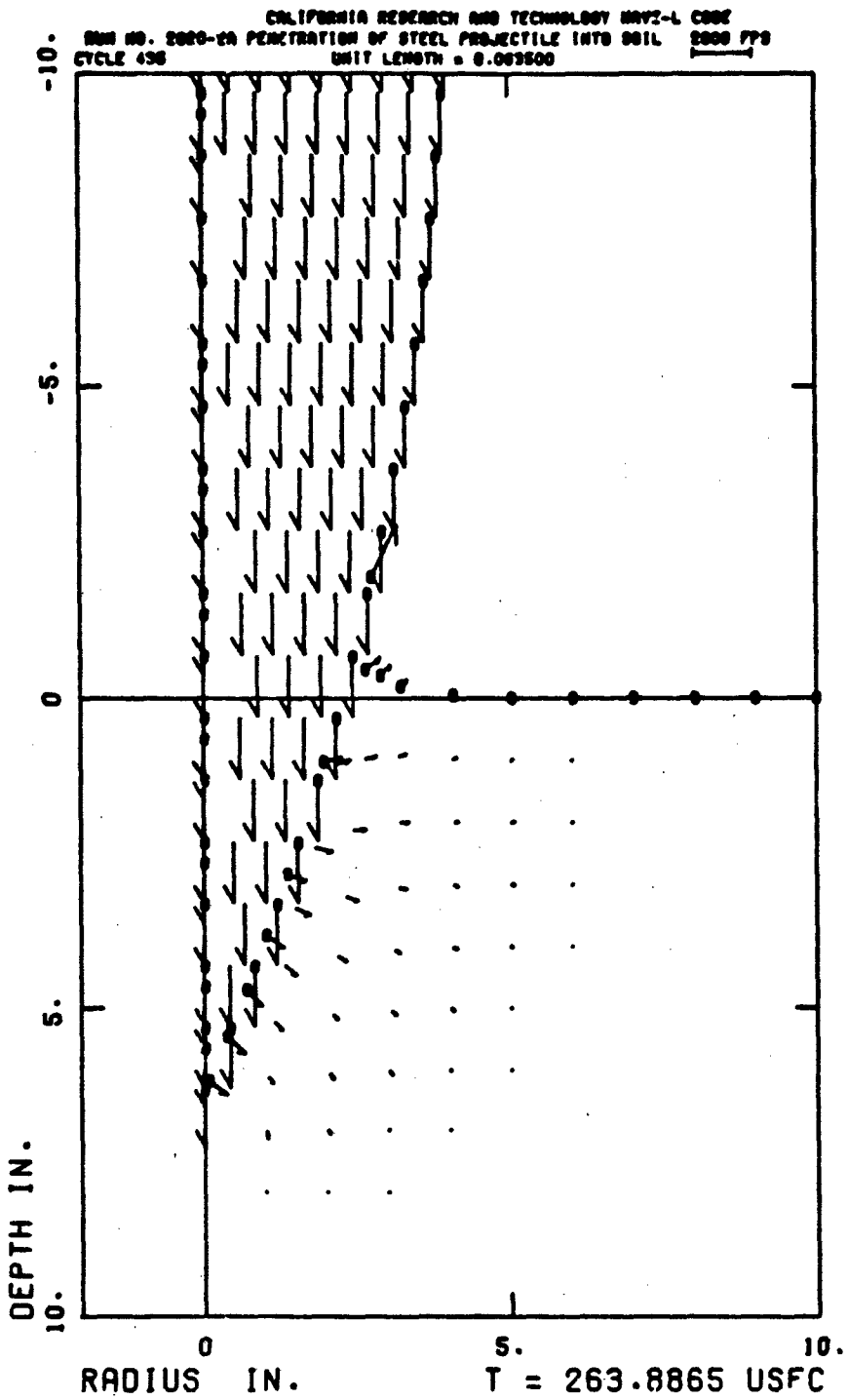

Figure B-9. Particle Velocity Field with Projectile at 6.33 in. Depth

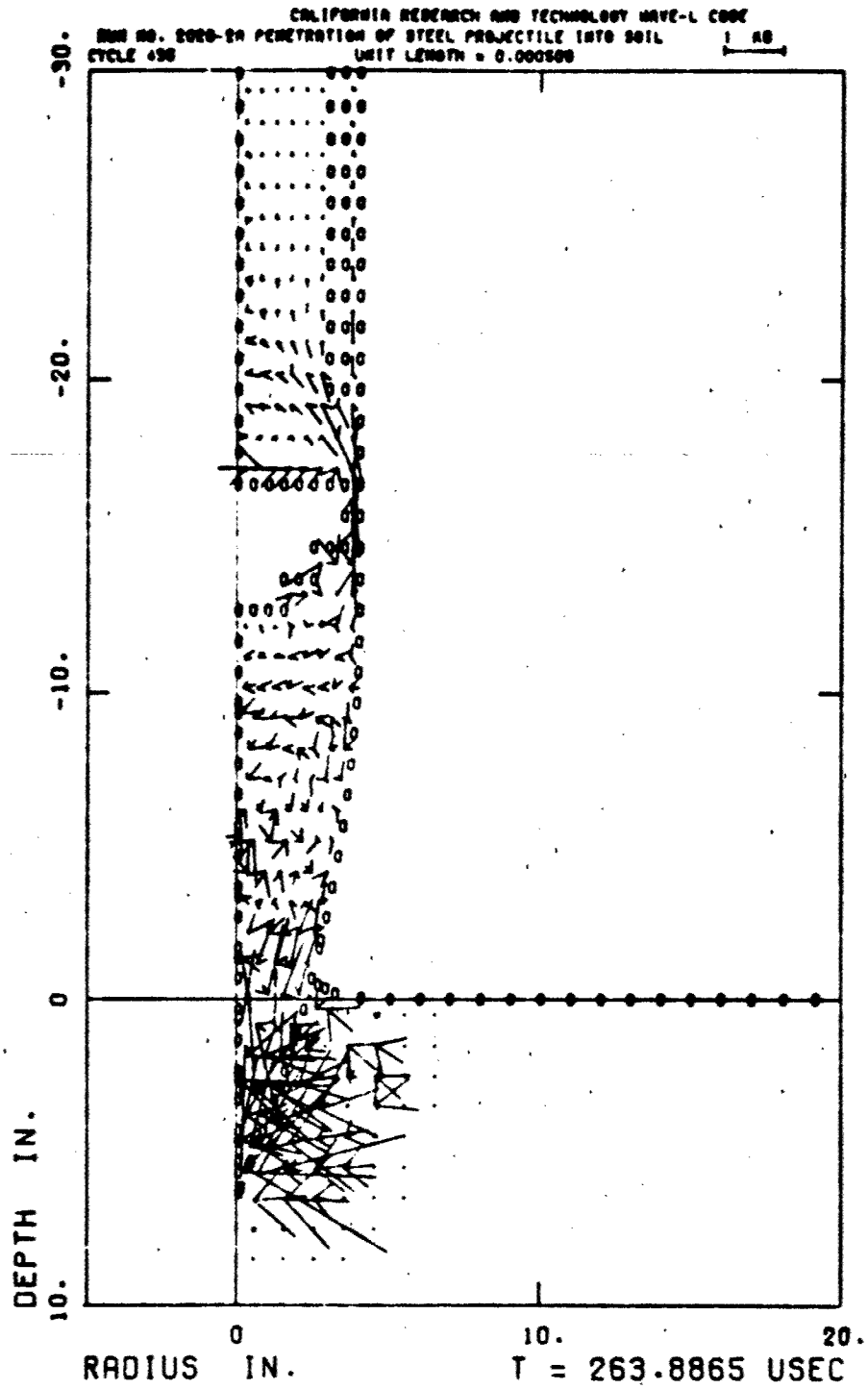

Figure 3-10. Principal Stress Field with Projectile at 6.33 in. Depth

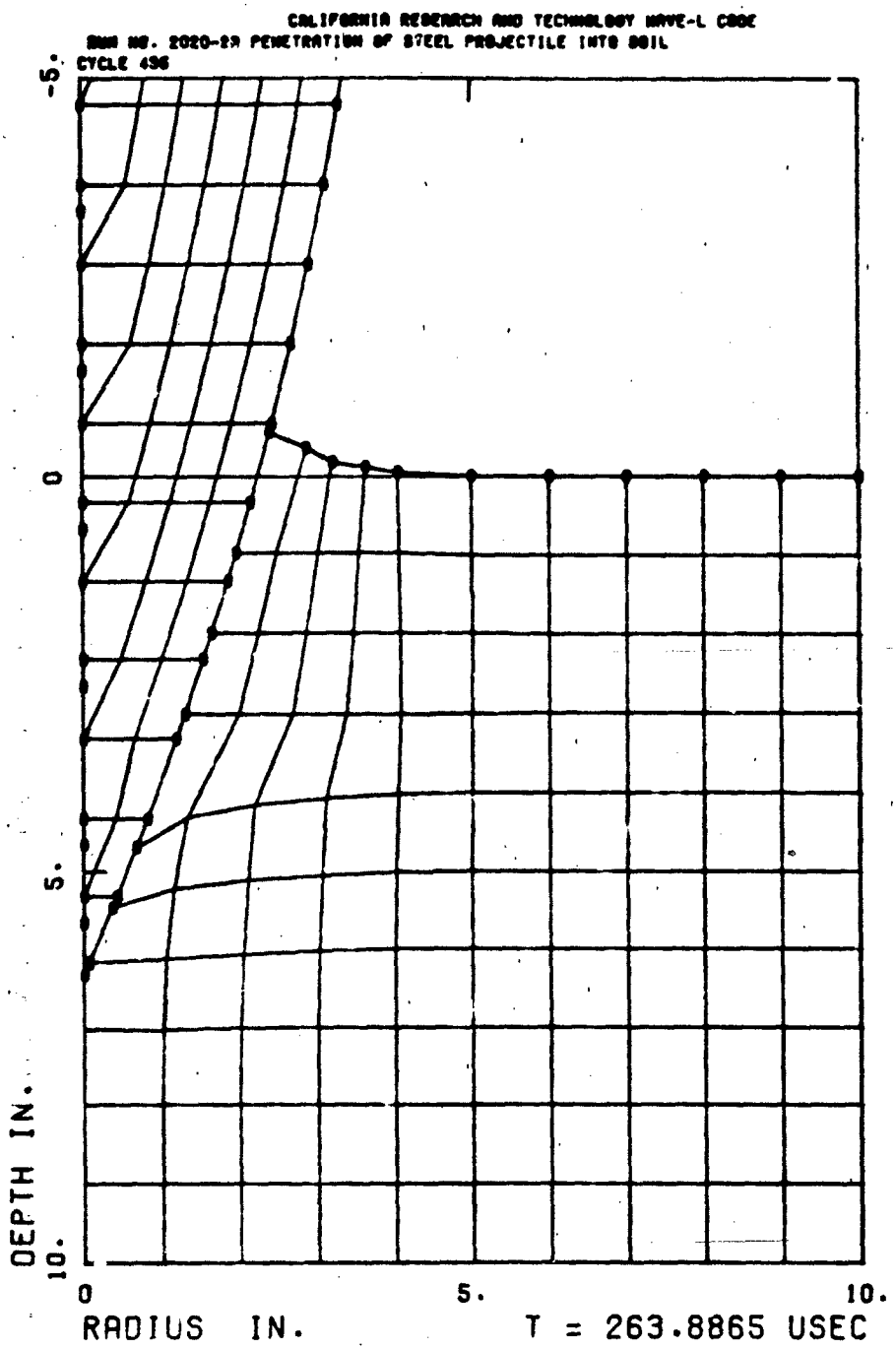

Figure 6-11. Grid Configuration Following Rezone

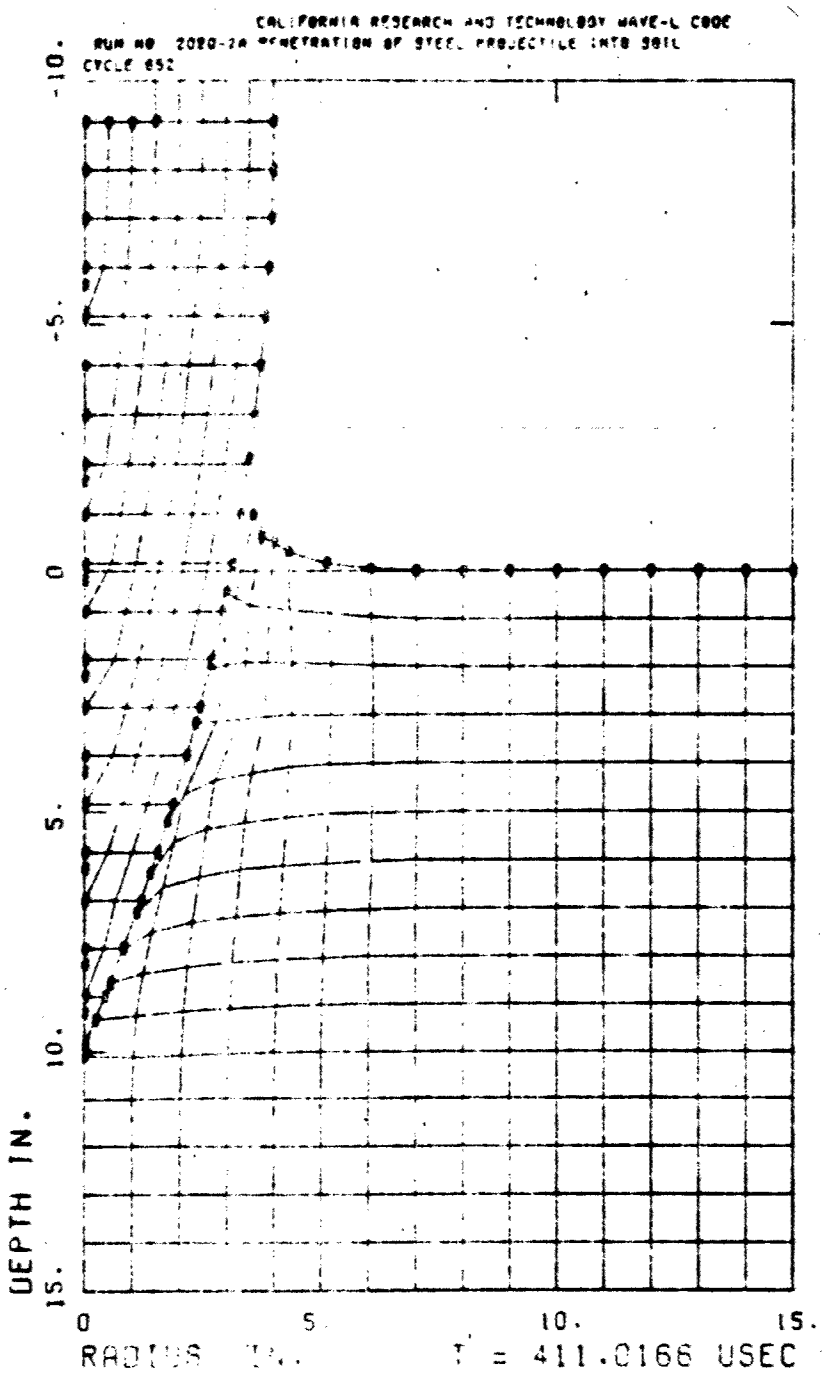

Figure [illegible] [illegible] at [illegible] in. depth

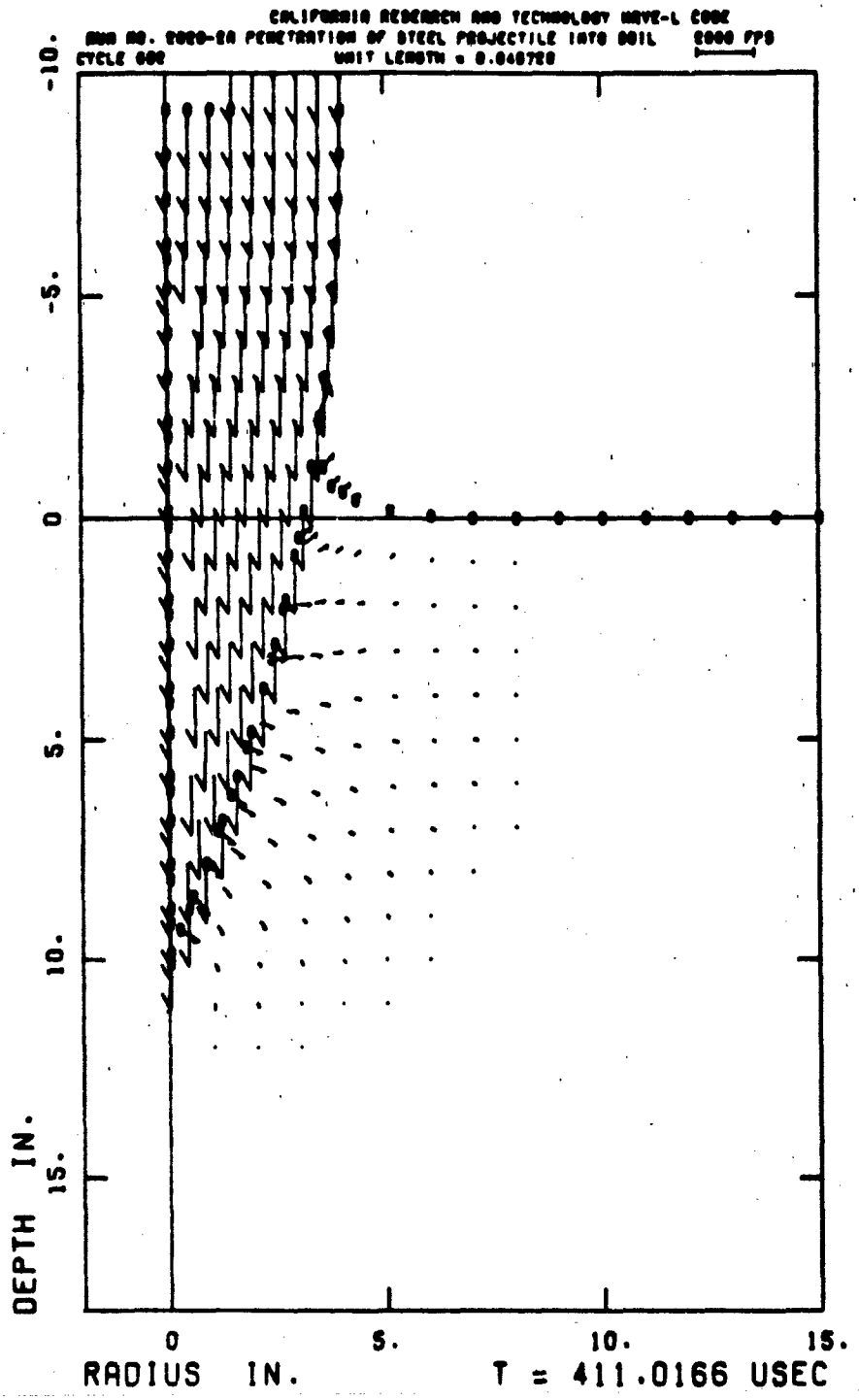

Figure 6-13. Particle Velocity Field with Projectile at 9.84 in. Depth

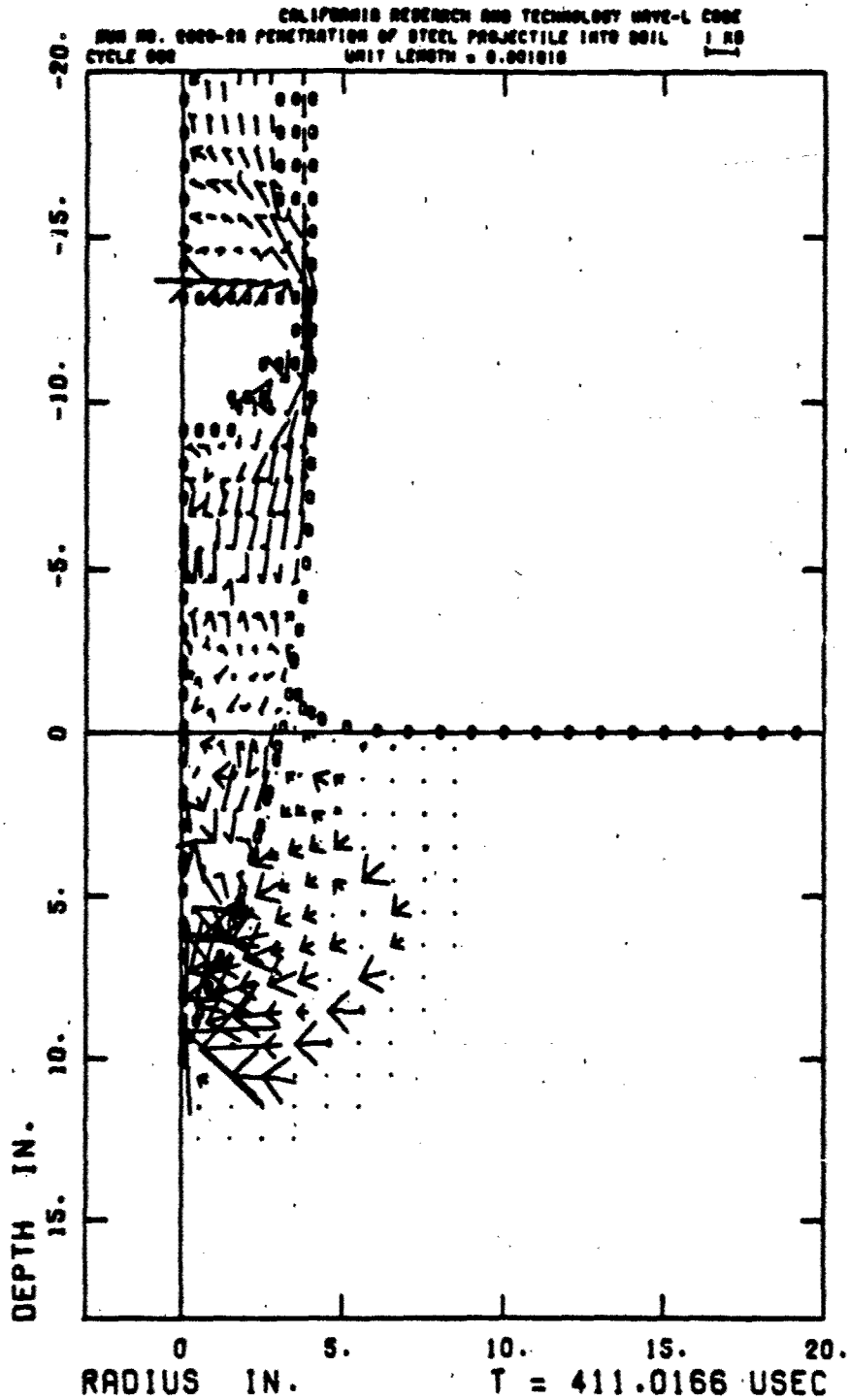

Figure B-14. Principal Stress Field with Projectile at 9.84 in. Depth

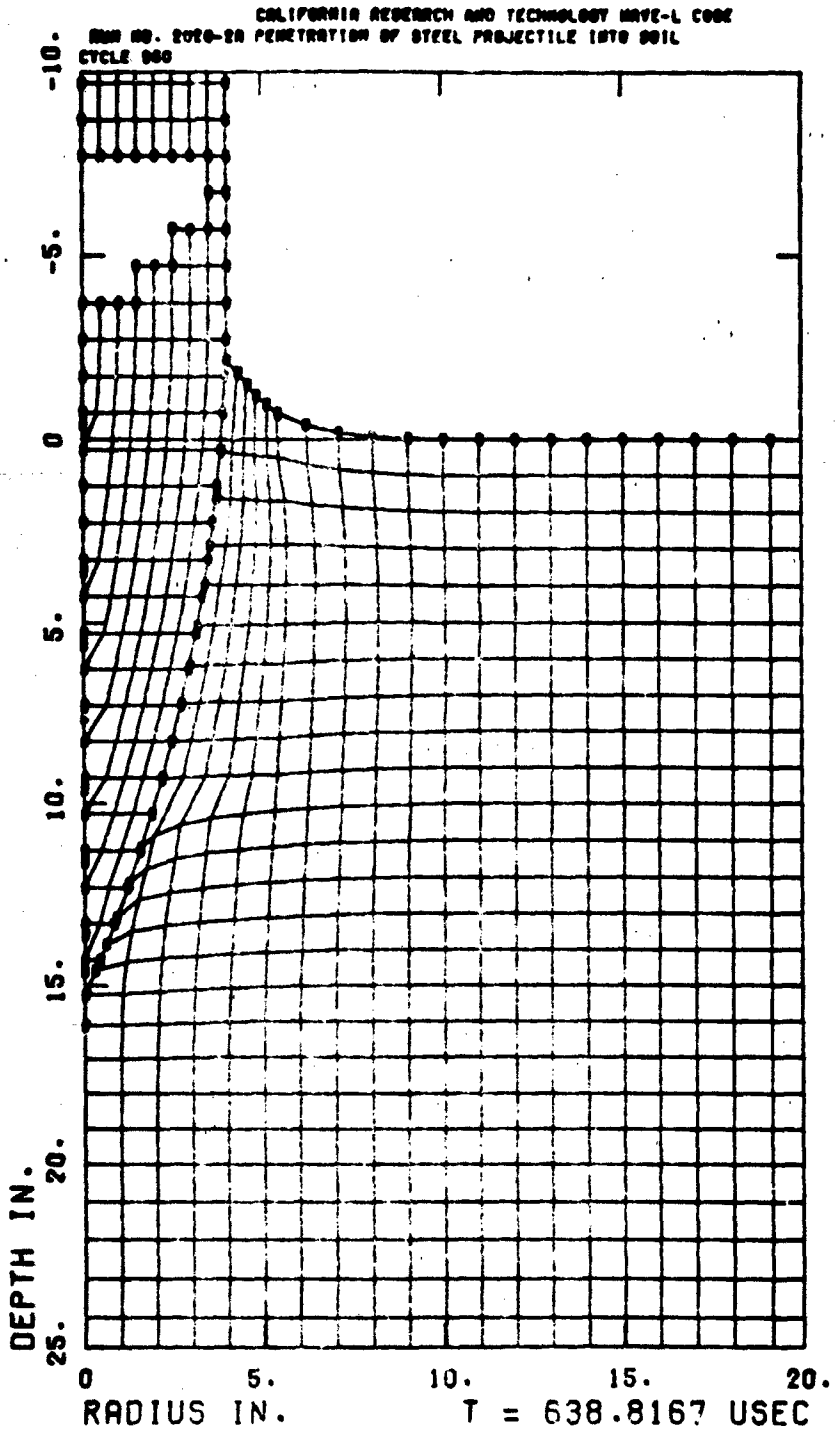

Figure [illegible]. [illegible] with [illegible] at 15.29 in. Depth

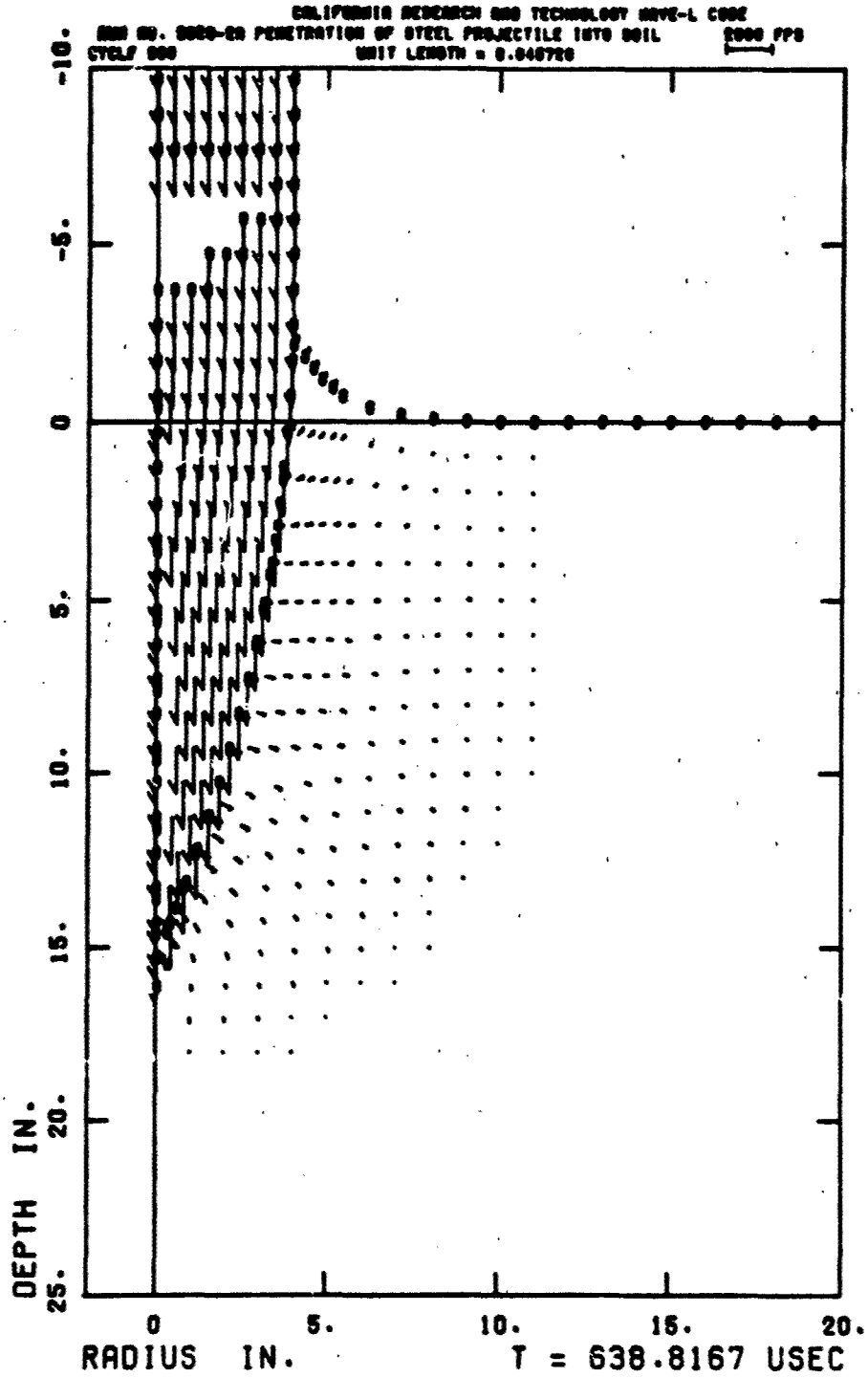

Figure 8-16. Particle Velocity Field with Projectile at 15.29 in. Depth

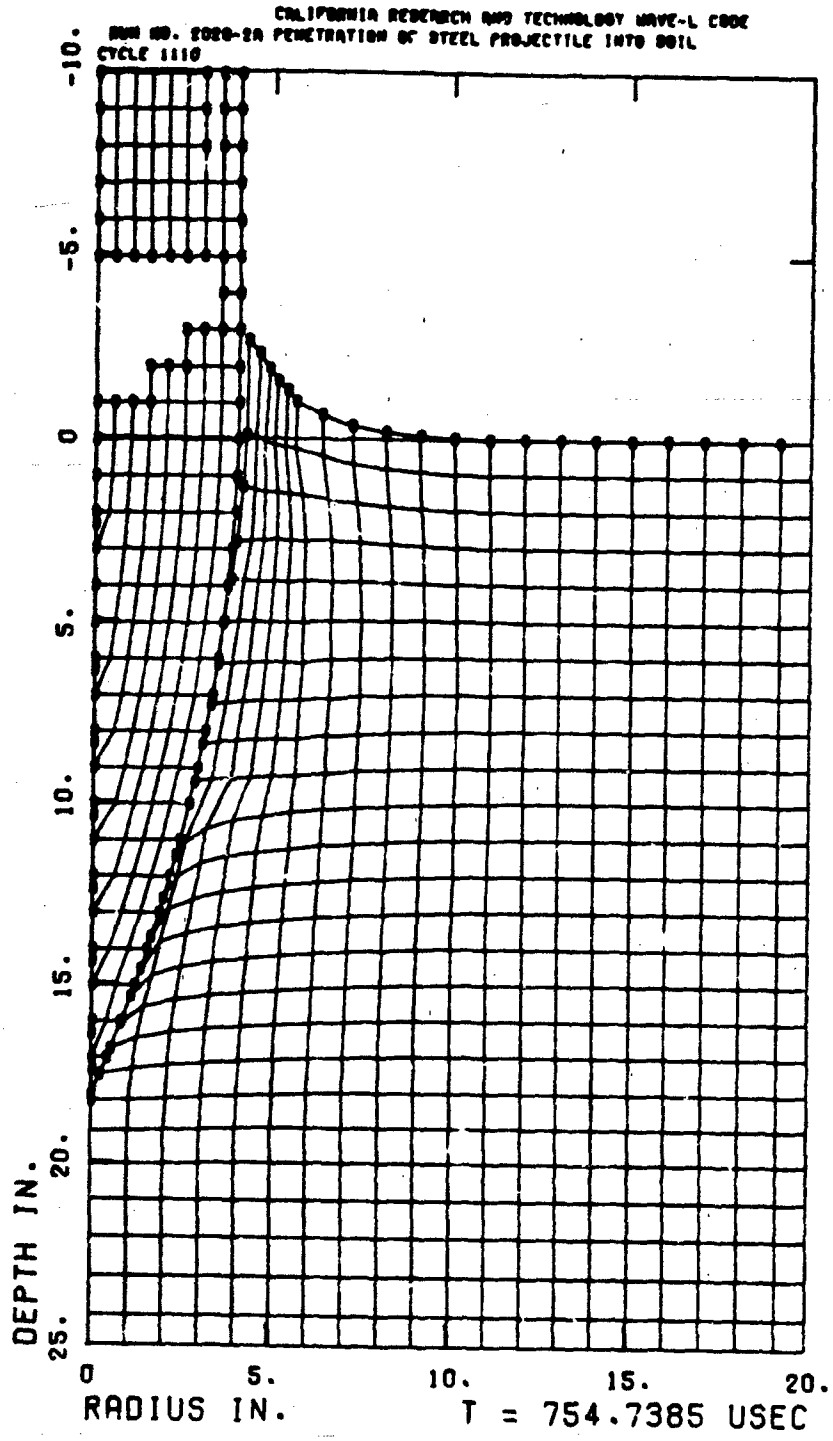

Figure B-17. Grid Configuration with Projectile at 18.06 in. Depth

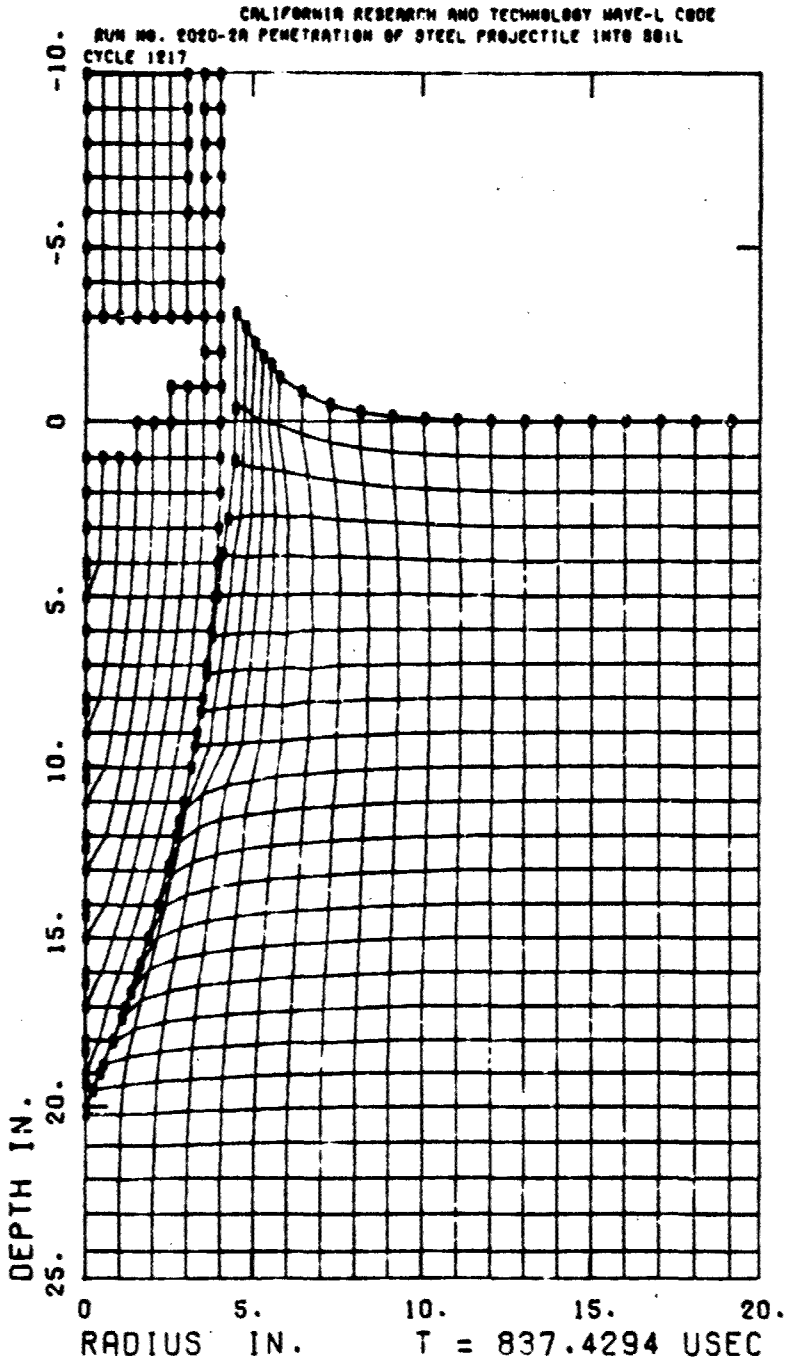

Figure B-18. Grid Configuration at End of Deformable-body Solution, Projectile at 20.03 in. Depth

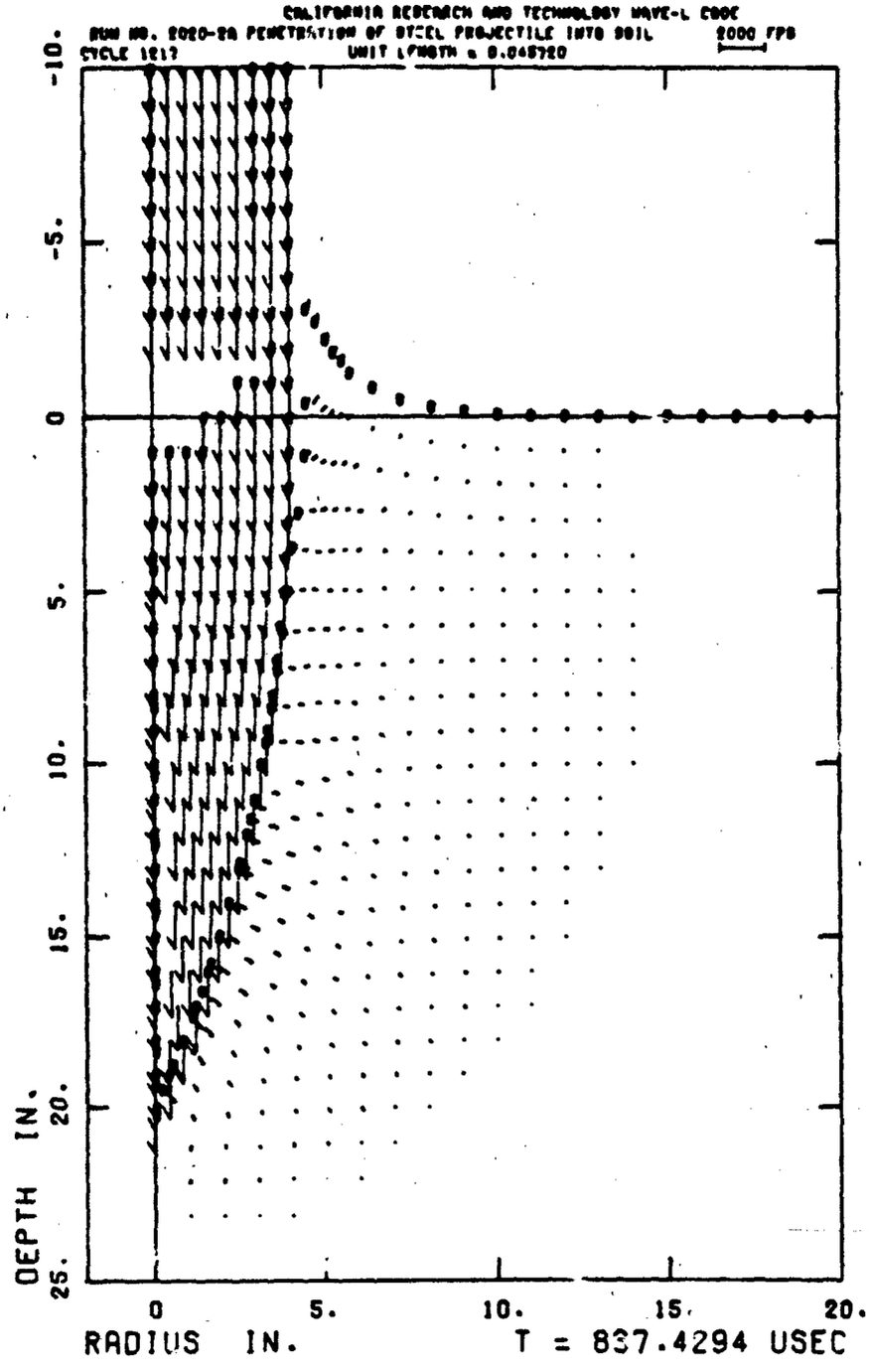

Figure B-19. Particle Velocity Field at End of Deformable-Body Solution, Projectile at 20 in. Depth

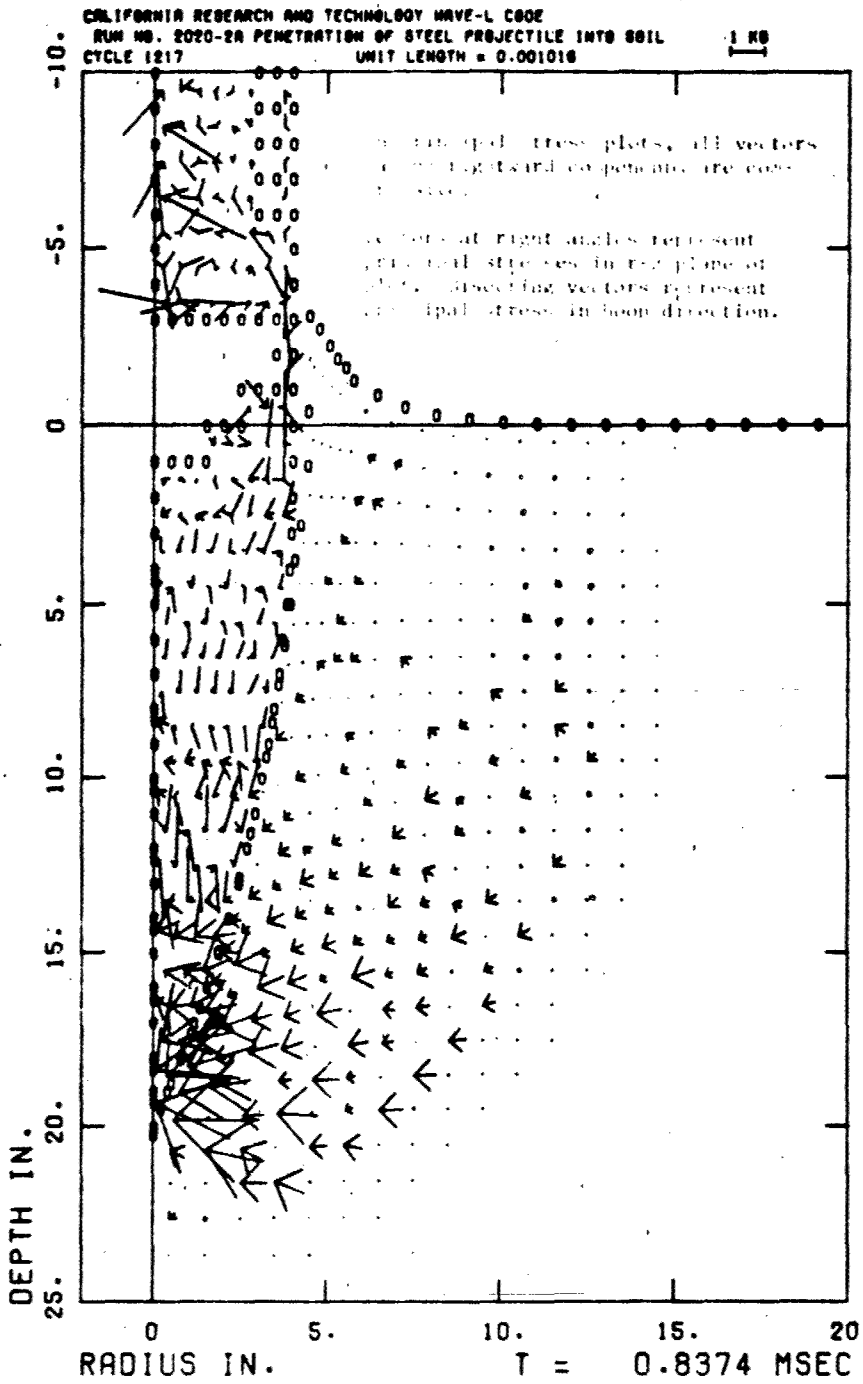

Figure B-20. Principal Stress Field at End of Deformable-Body Solution, Projectile at 20 in. Depth

APPENDIX C

DISTORTION, VELOCITY, AND PRINCIPAL STRESS FIELD PLOTS - RIGID-BODY SOLUTION

A series of field plots of the computational grid, particle velocities, and principal stresses which illustrate the soil response during the rigid-body solution were prepared. These are shown for the following penetration depth and times:

Depth (ft)	Time (msec)	Figure No. of Plot for: Distortion (Grid)	Velocity	Stress
.34	.17	C-1	C-2	C-3
.84	.42	C-4	C-5	C-6
1.67	.84	C-7	C-8	C-9
5.00	2.52	C-10	C-11	C-11
10.00	5.08	C-13	C-14	C-15
15.00	7.69	C-16	C-17	C-18
16.92	8.70	C-19	C-20	C-21
22.31	11.58	C-22	C-23	C-24

The plots of the grid also show which material is currently failing; i.e., is on the yield surface. This is denoted by cells containing an x or + , with x indicating a compressive pressure, $P \geq 0$, and + indicating hydrostatic tension, $P < 0$.

The velocity vector field plots show the direction and magnitude of the particle velocity at each lattice point in

the computing grid. For clarity in viewing the soil response, the velocity vectors of the projectile are not shown.

The plotting convention for the principal stress field plots is the same as that used in the deformable-body solution (Appendix B).

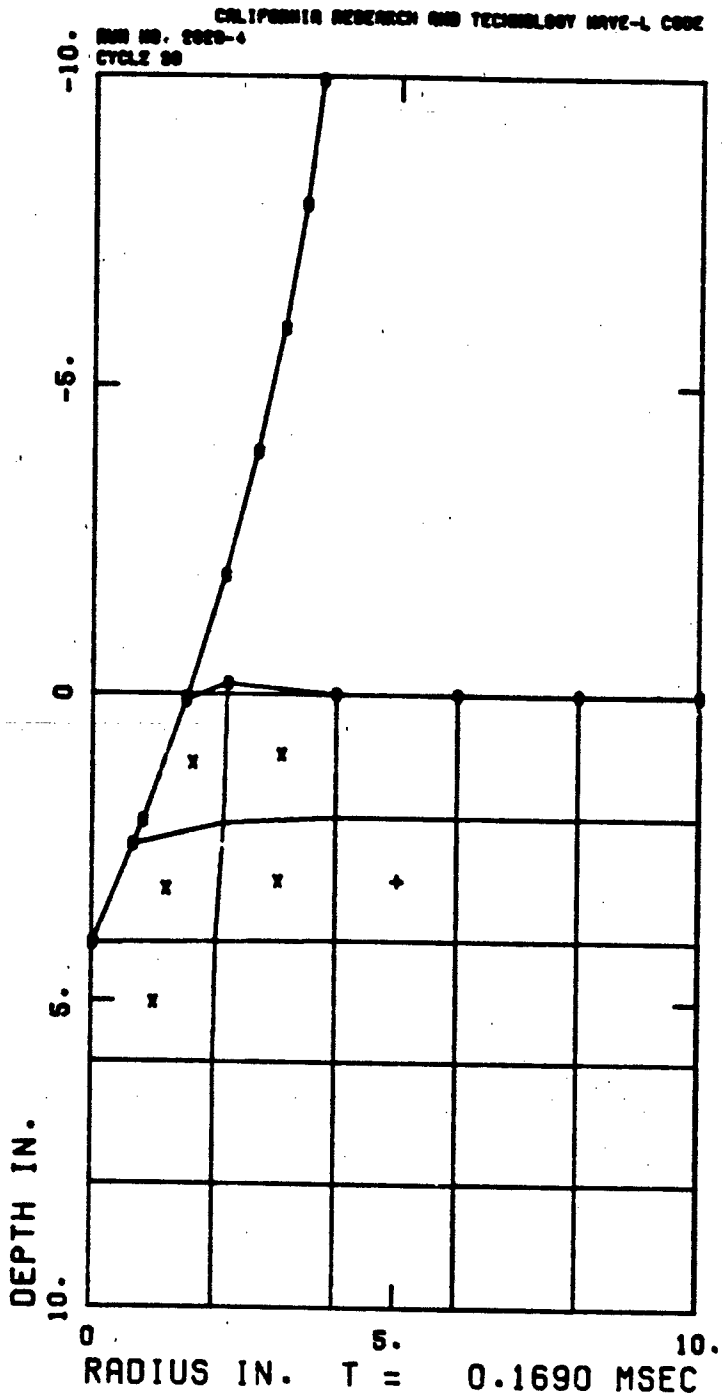

Figure C-1. Grid Configuration with Projectile at 4 in. Depth

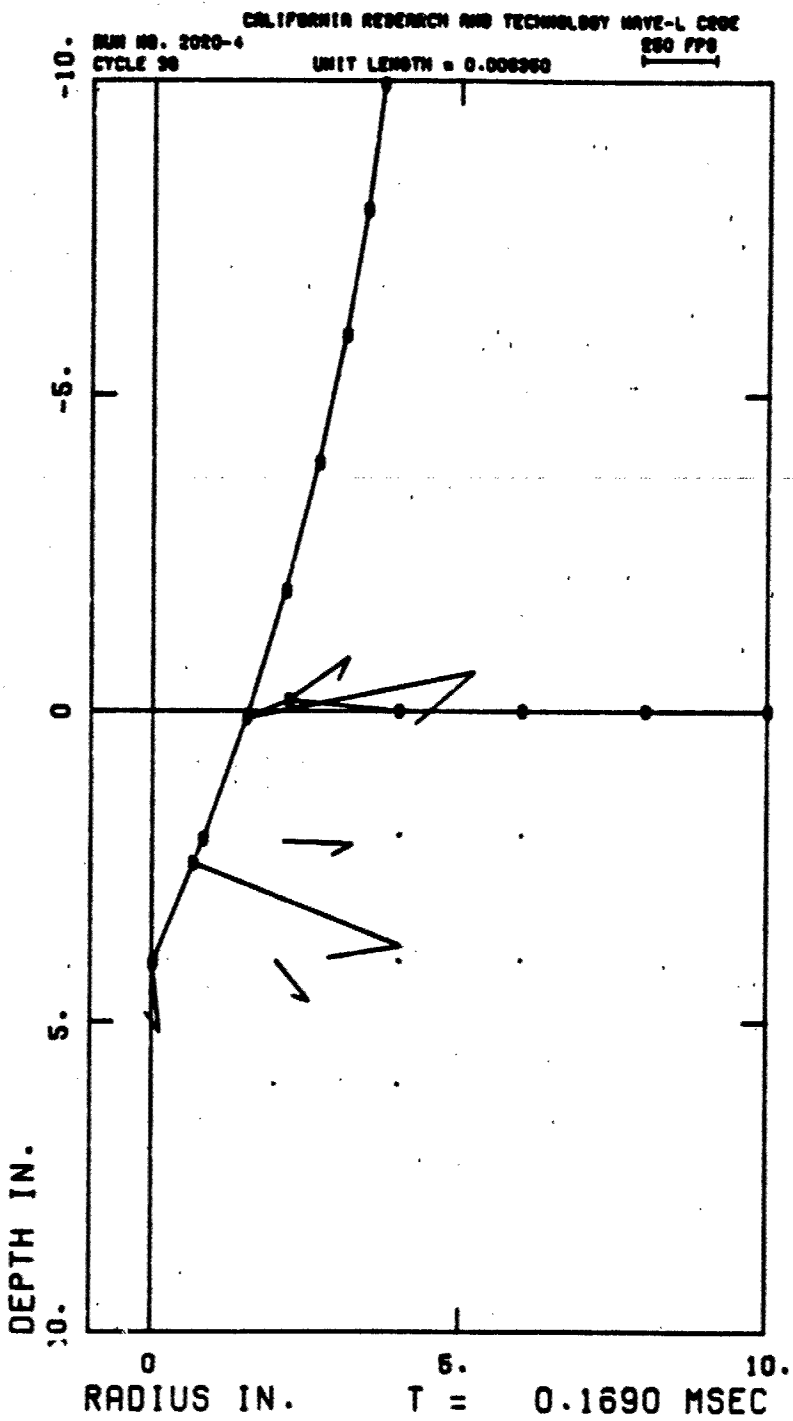

Figure C-2. Particle Velocity Field with Projectile at 4 in. Depth

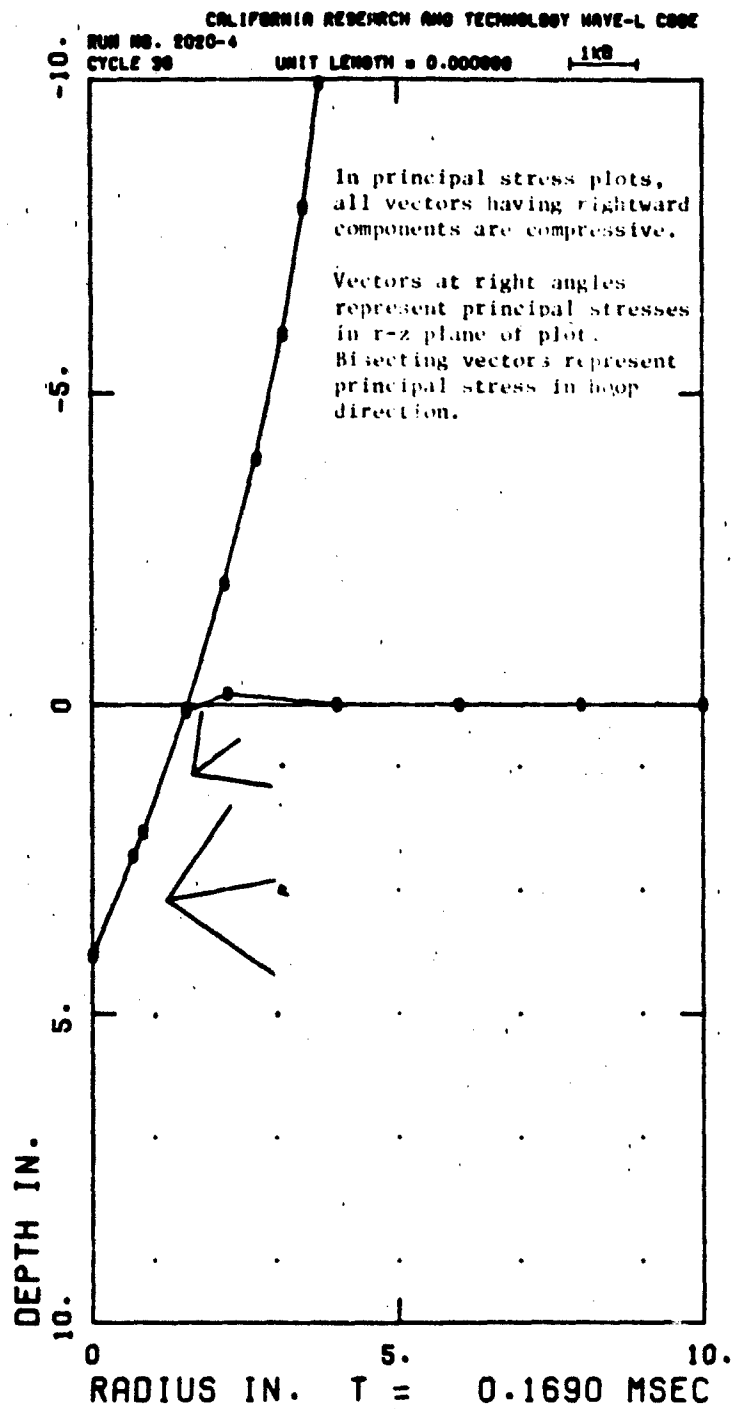

Figure C-3. Principal Stress Field with Projectile at 4 in. Depth

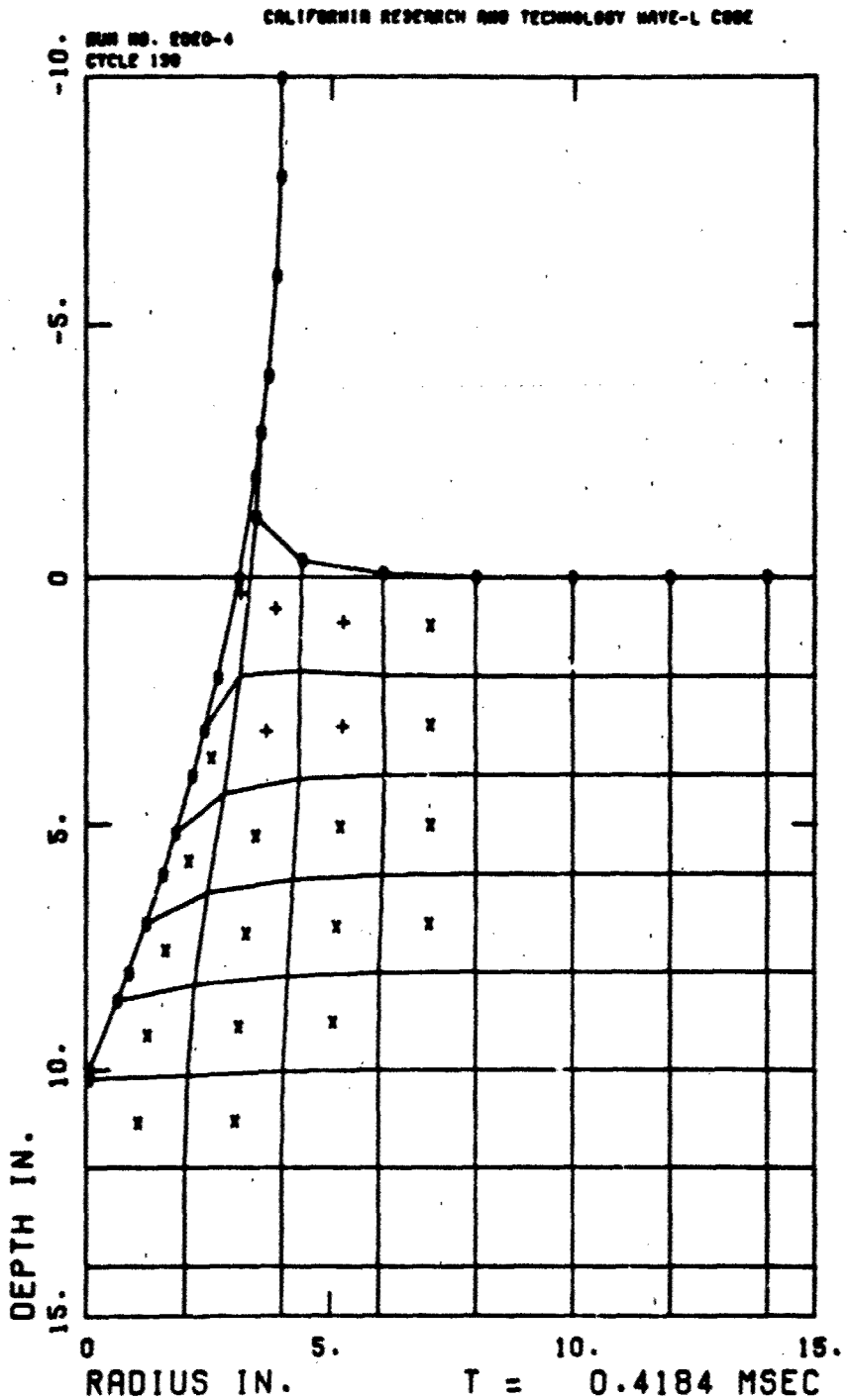

Figure C-4. Grid Configuration with Projectile at 10 in. Depth

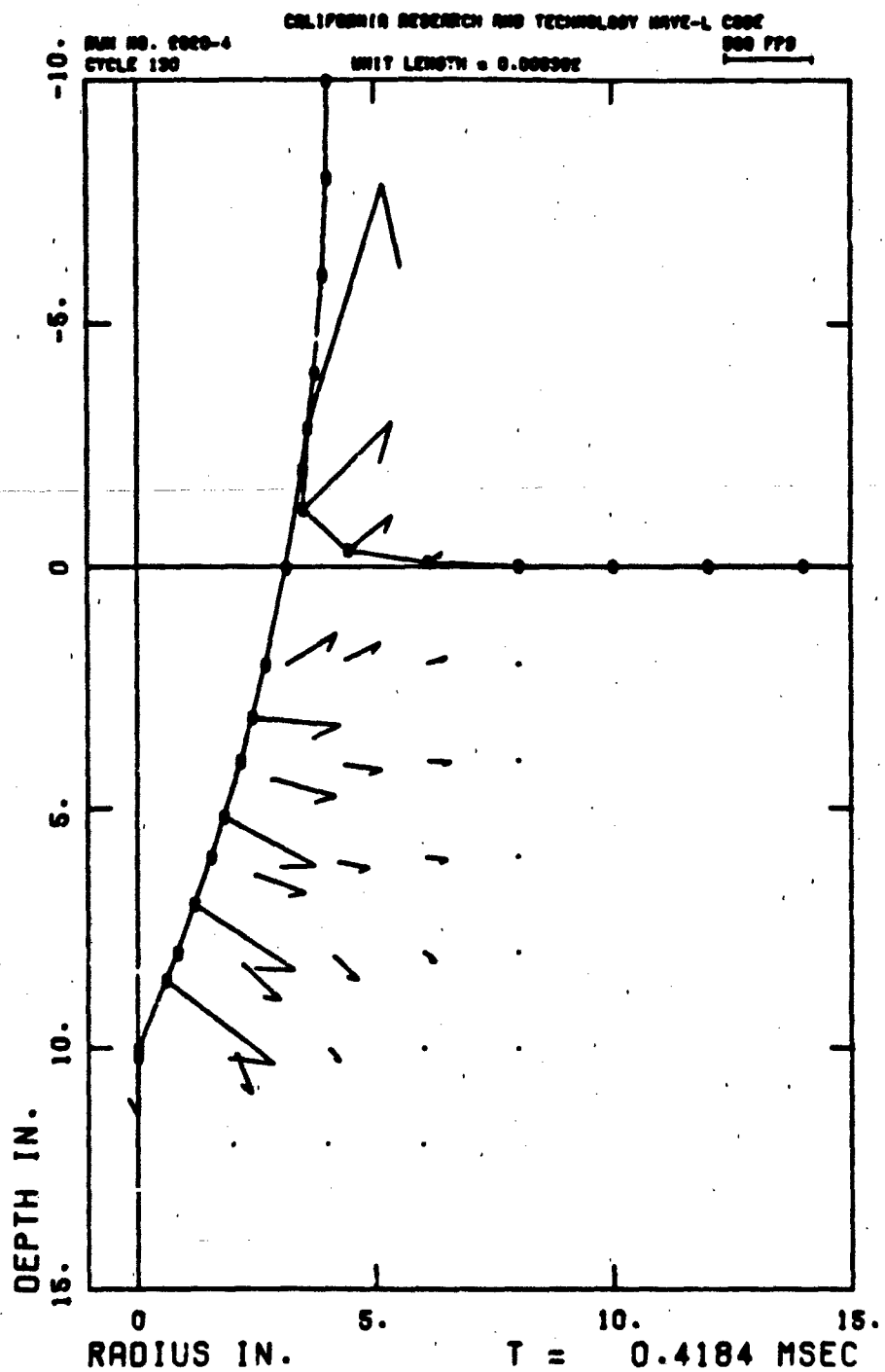

Figure C-5. Particle Velocity Field with Projectile at 10 in. Depth

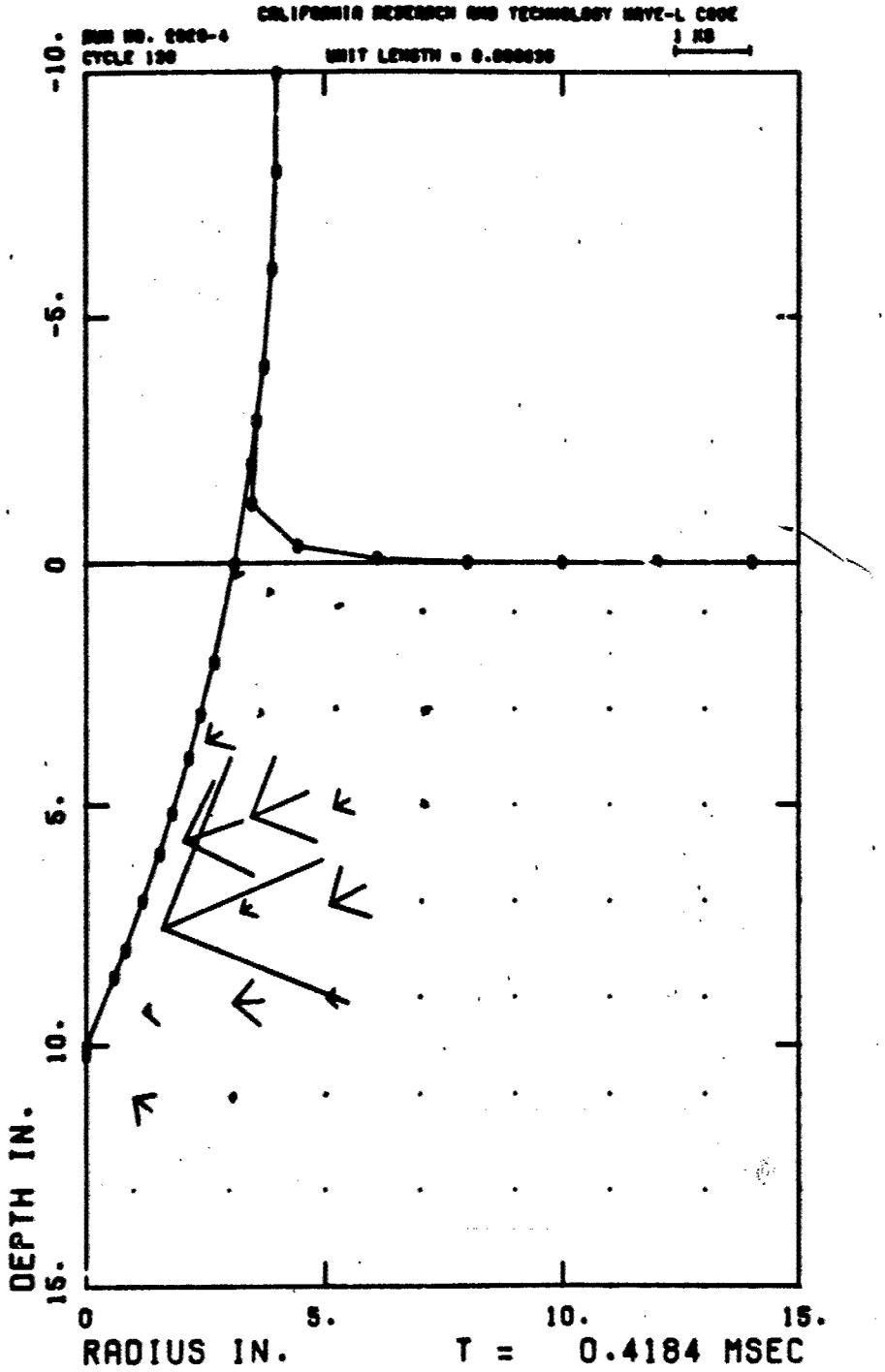

Figure C-6. Principal Stress Field with Projectile at 10 in. Depth

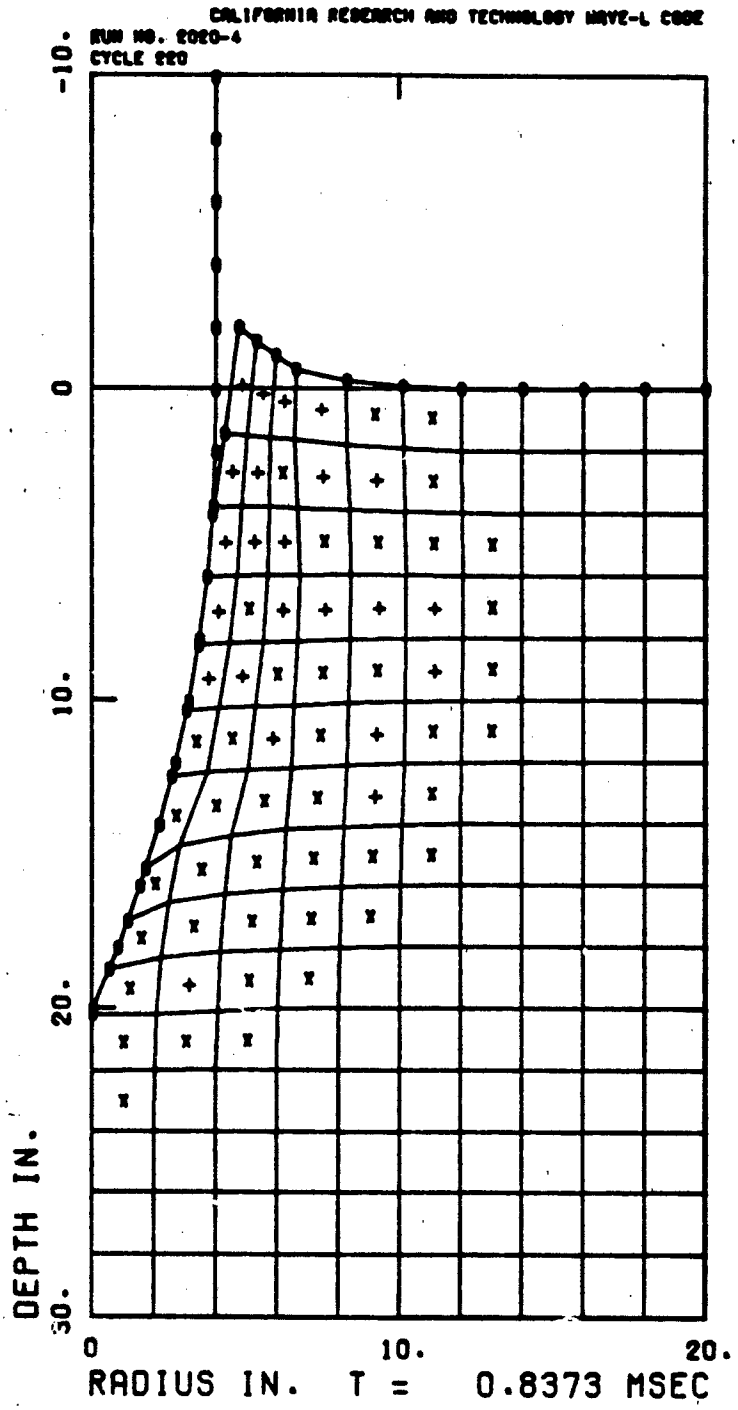

Figure C-7. Grid Configuration with Projectile at 20 in. Depth

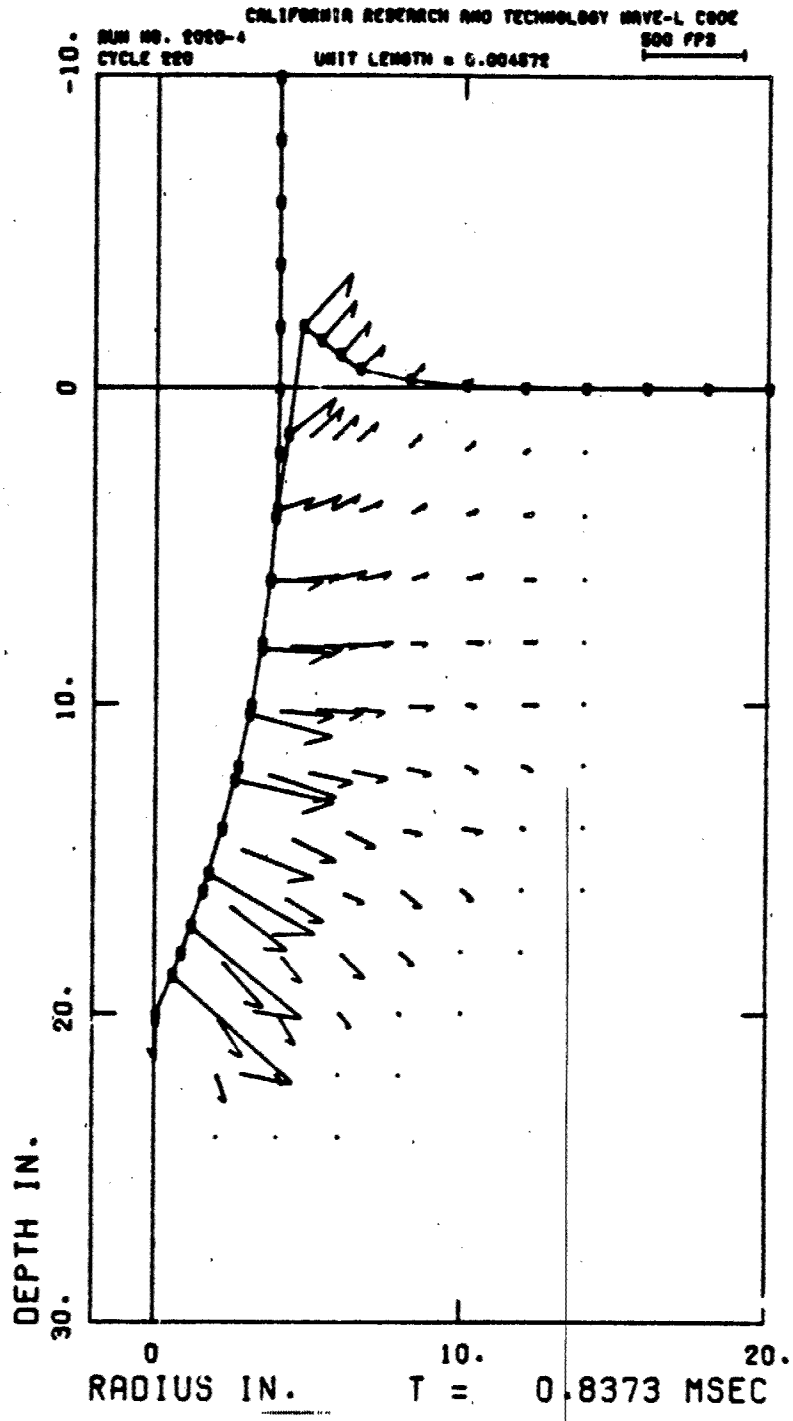

Figure C-8. Particle Velocity Field with Projectile at 20 in. Depth

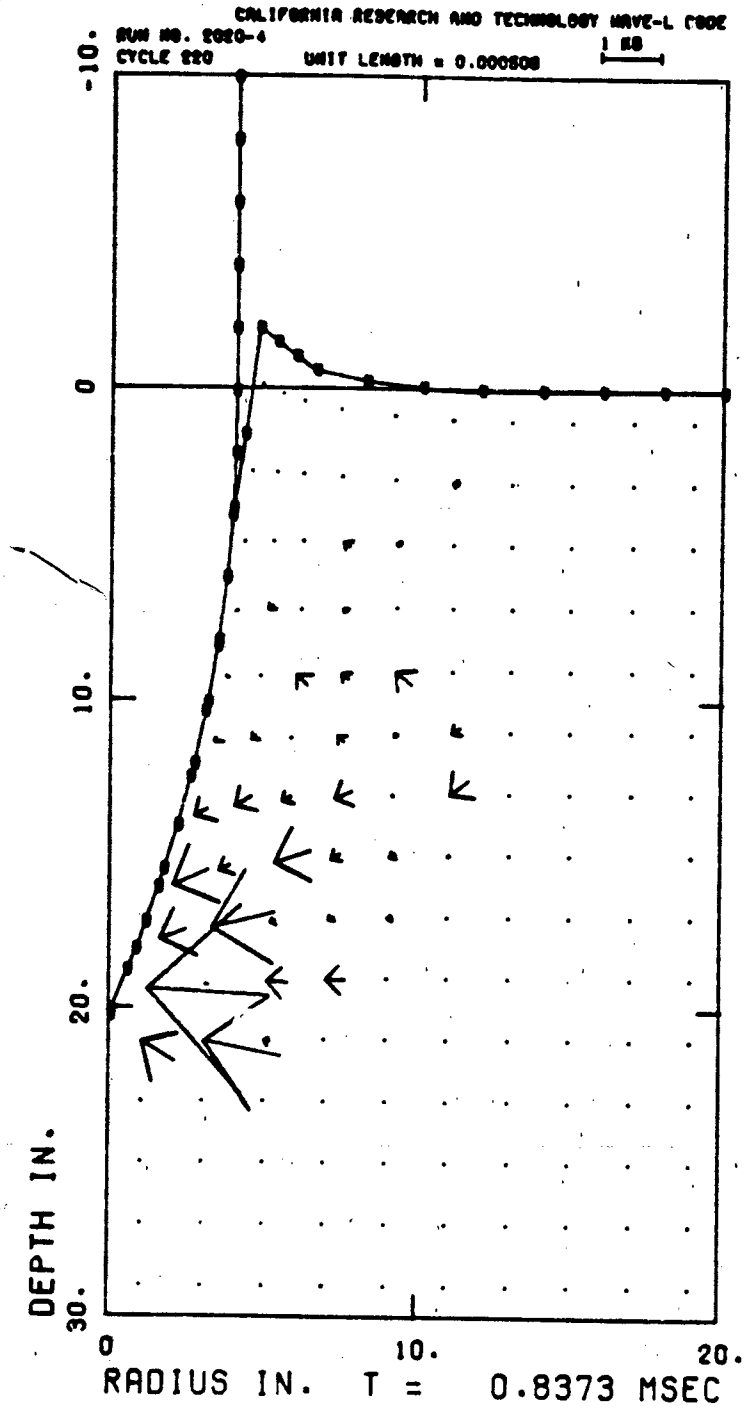

Figure C-9. Principal Stress Field with Projectile at 20 in. Depth

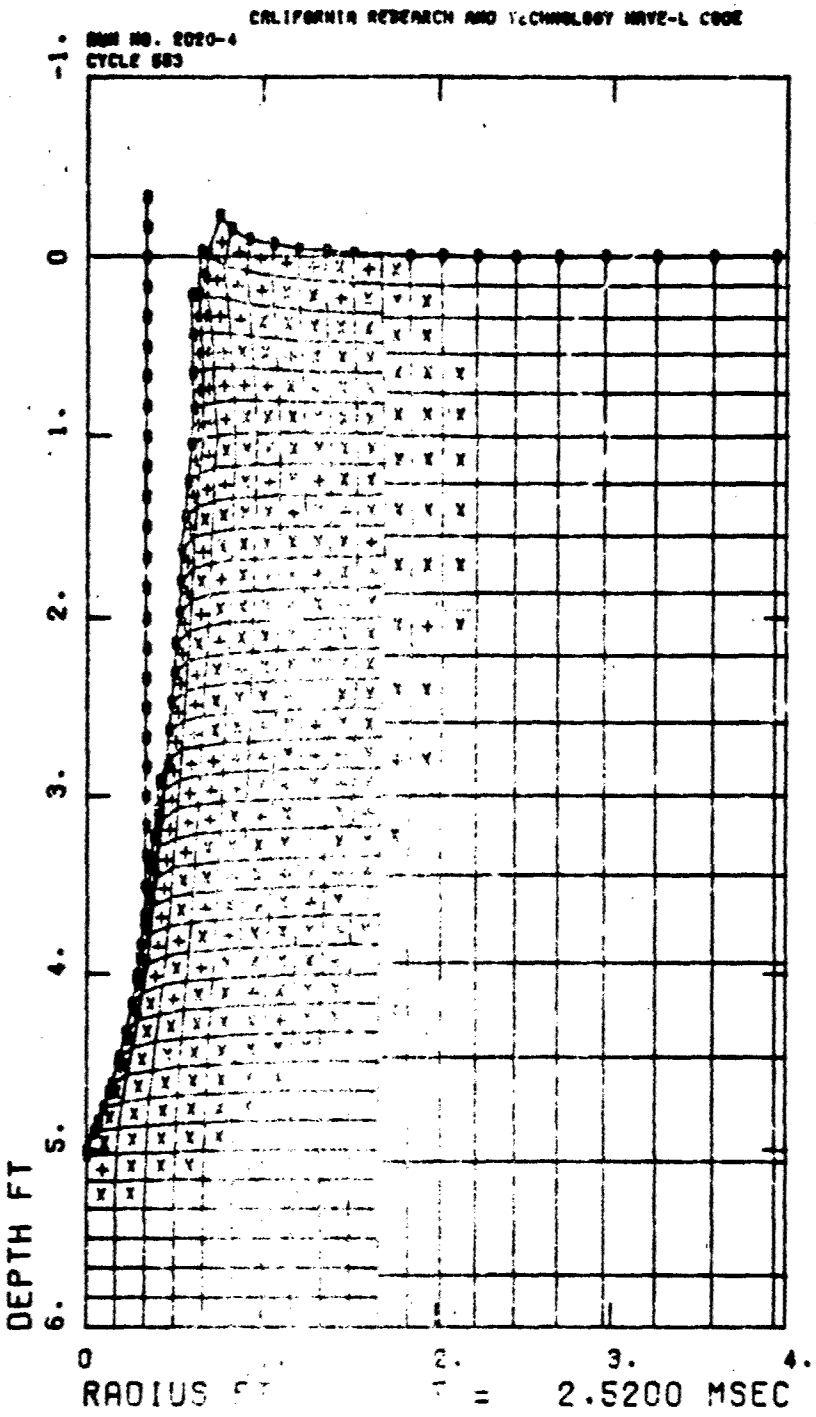

Figure [illegible] Depth

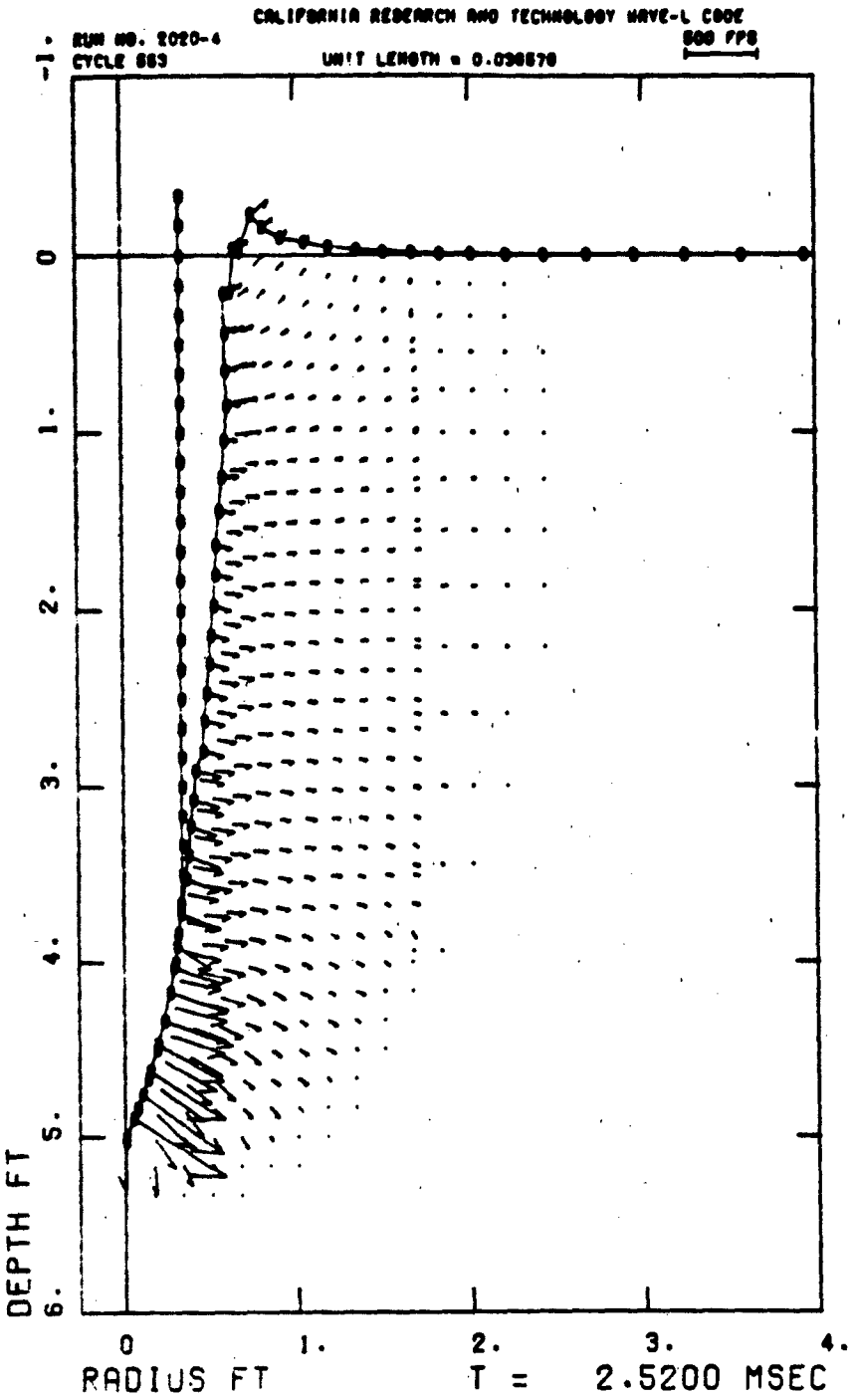

Figure -11. Particle Velocity Field with Projectile at 5 ft Depth

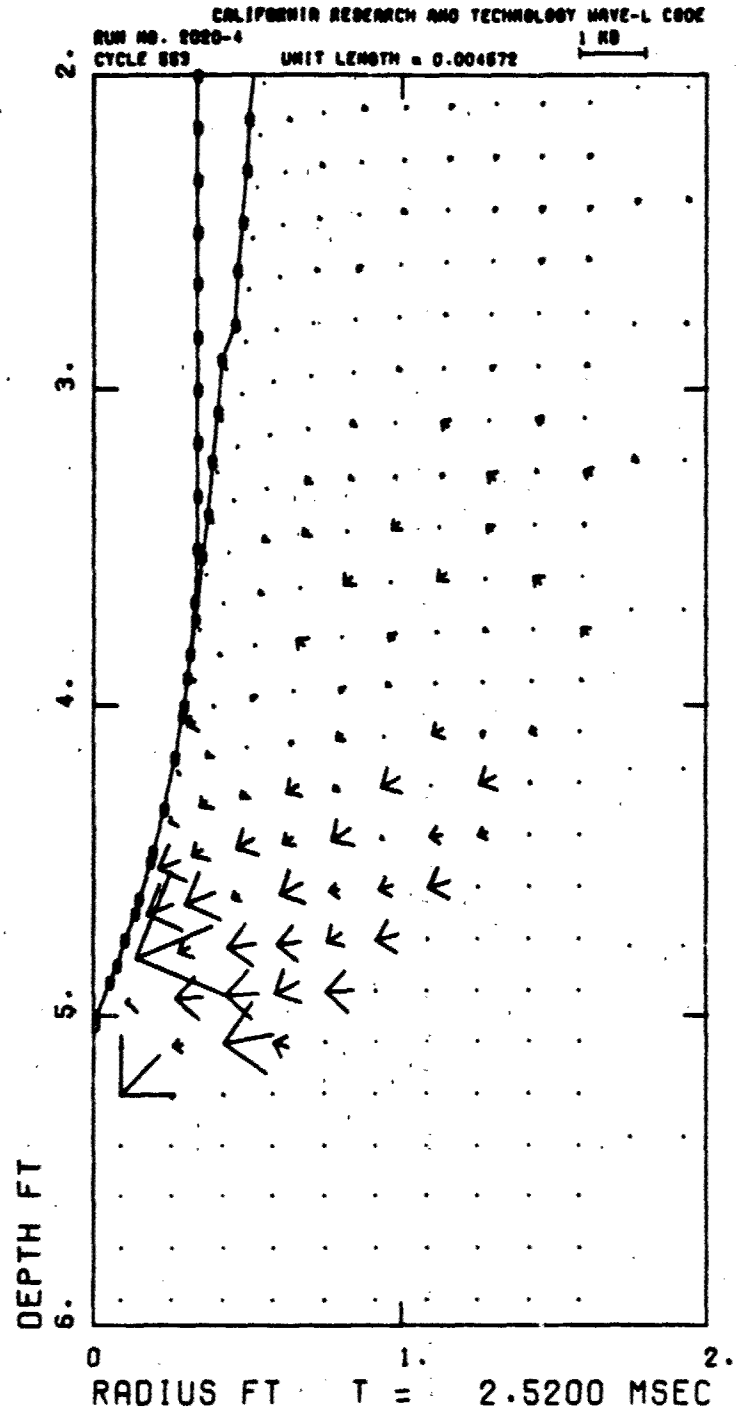

Figure C-12. Principal Stress Field with Projectile at 5 ft Depth

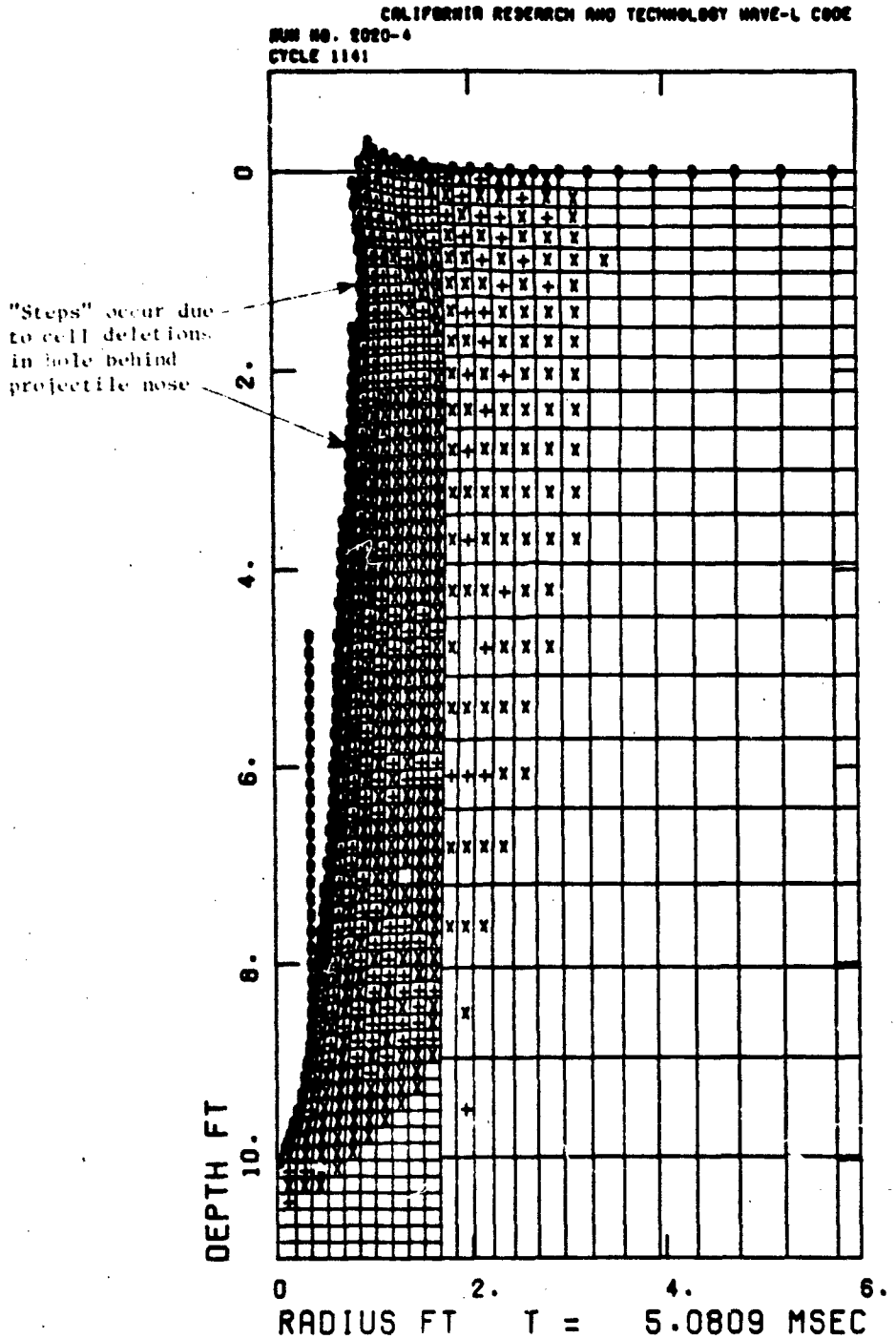

Figure C-13. Grid Configuration with Projectile at 10 ft. Depth

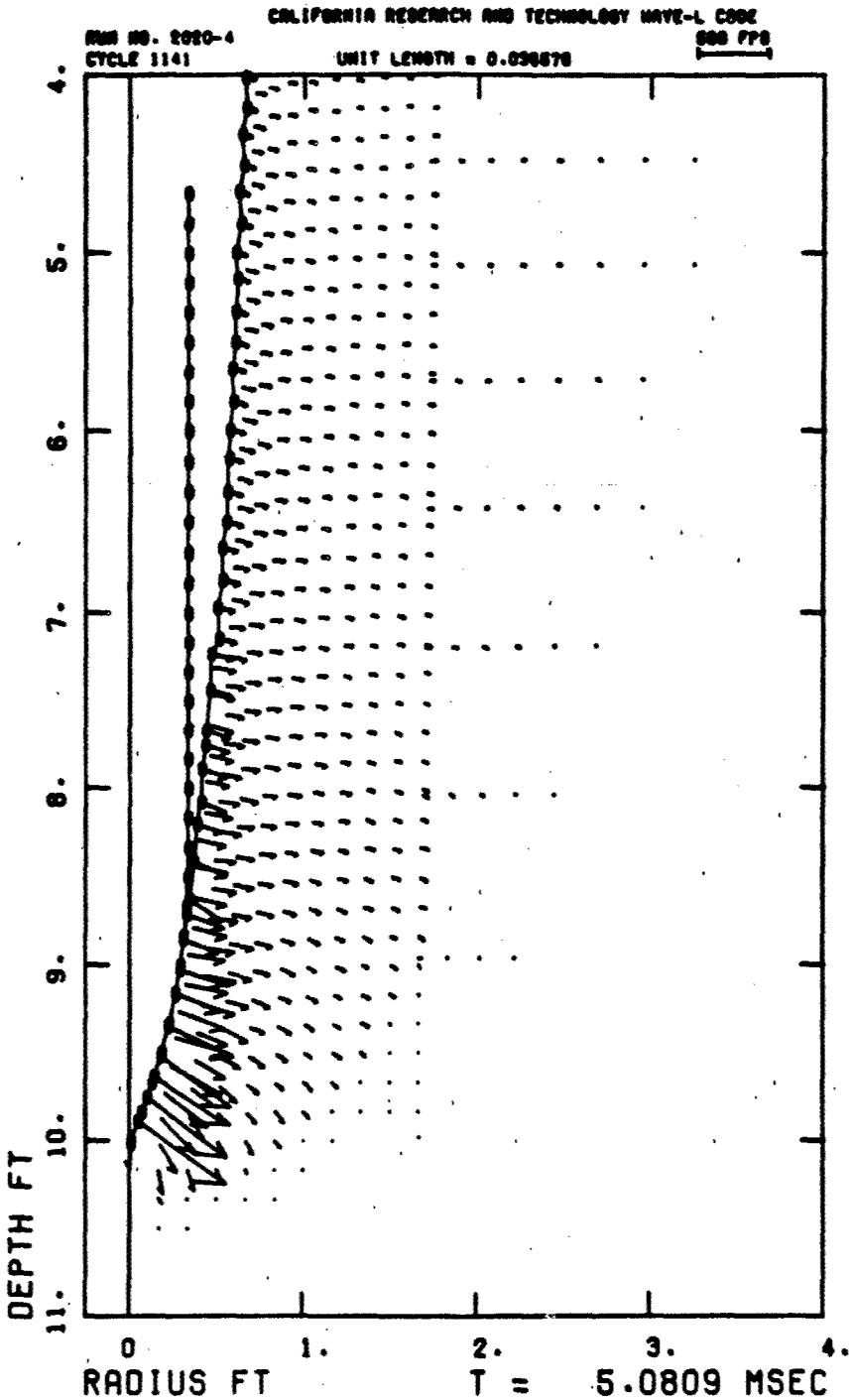

Figure C-14. Particle Velocity Field with Projectile at 10 ft. Depth

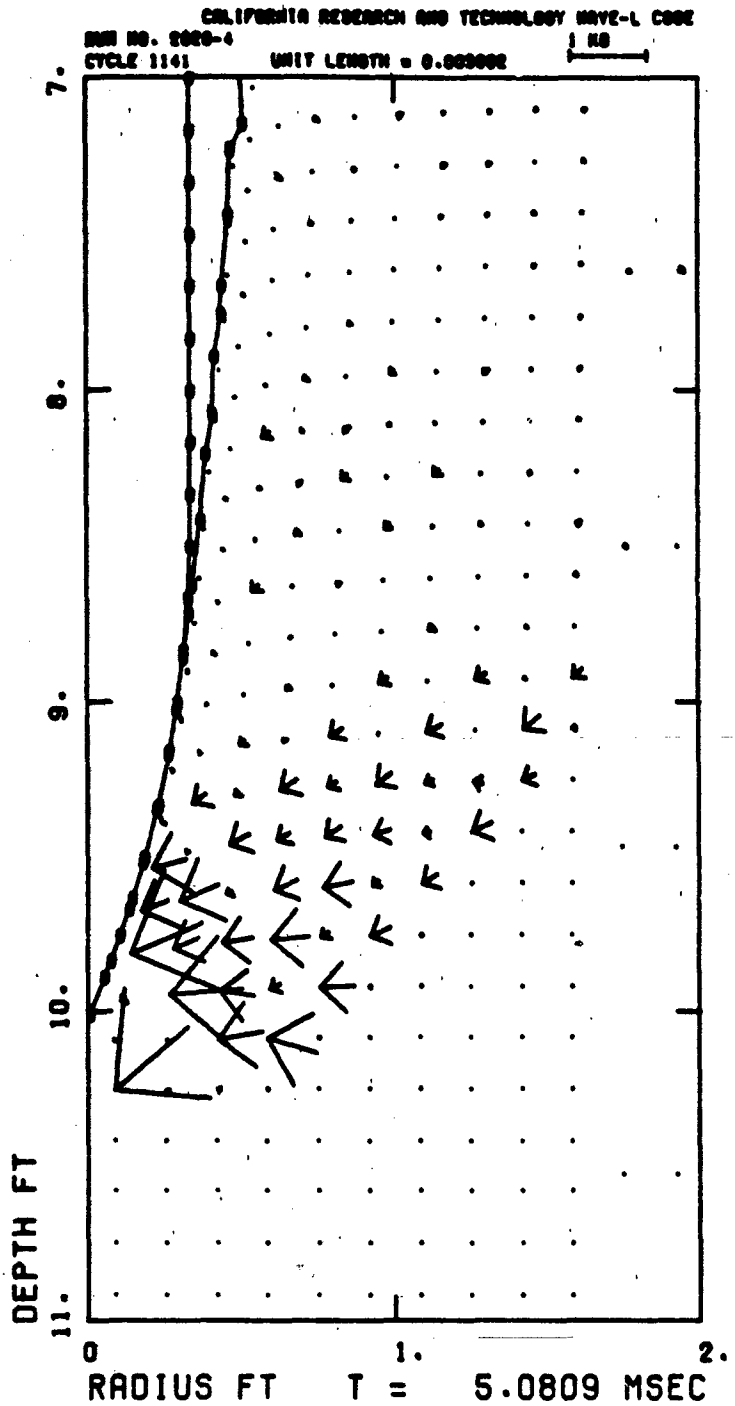

Figure C-15. Principal Stress Field with Projectile at 10 ft. Depth

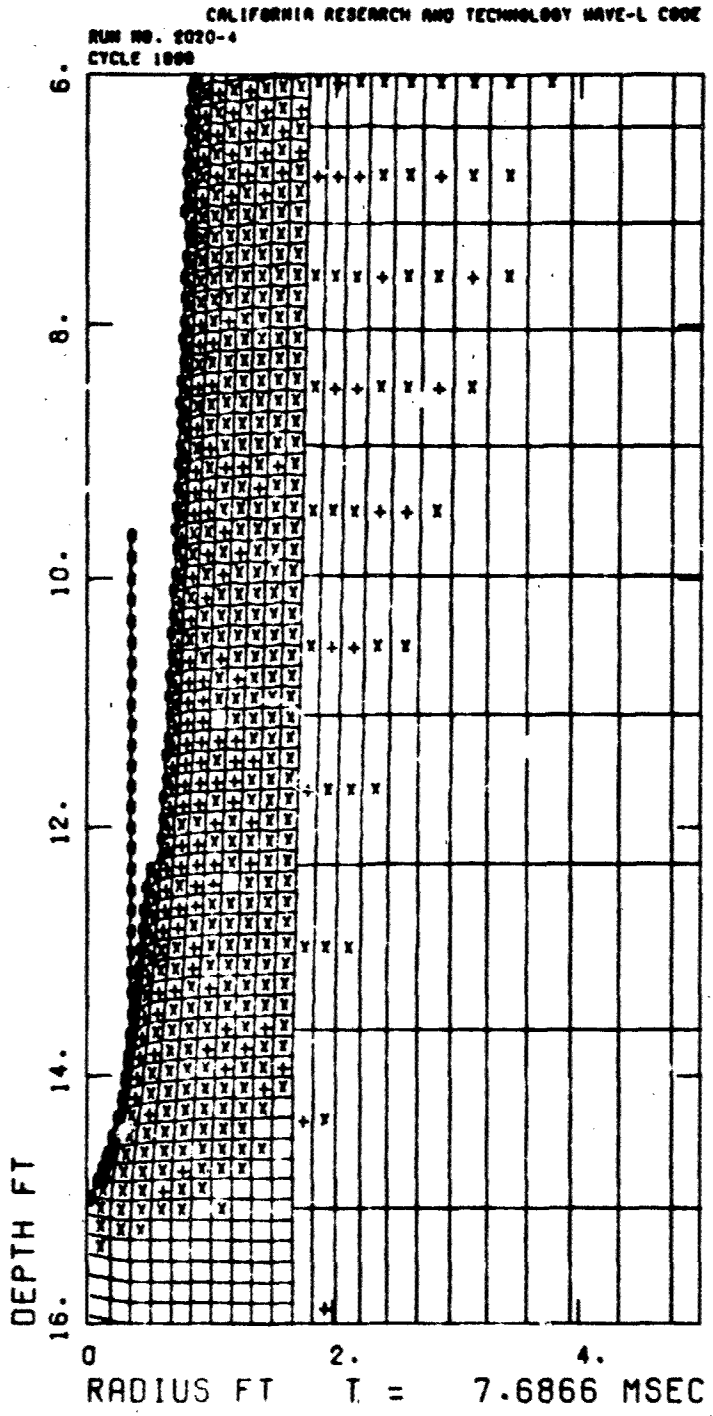

Figure 4-16. Grid Configuration with Projectile at 15 ft Depth

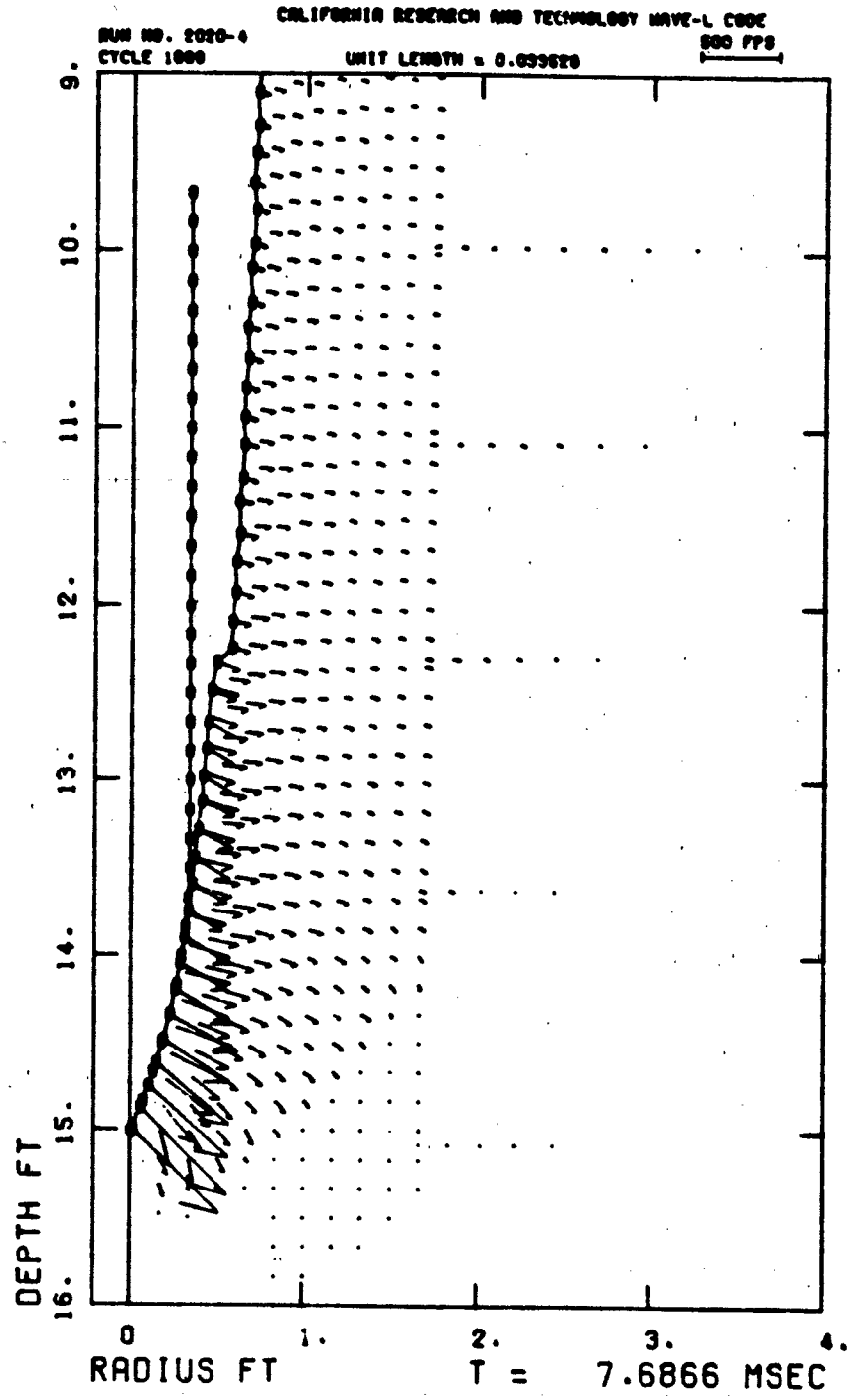

Figure C-17. Particle Velocity Field with Projectile at 15 ft Depth

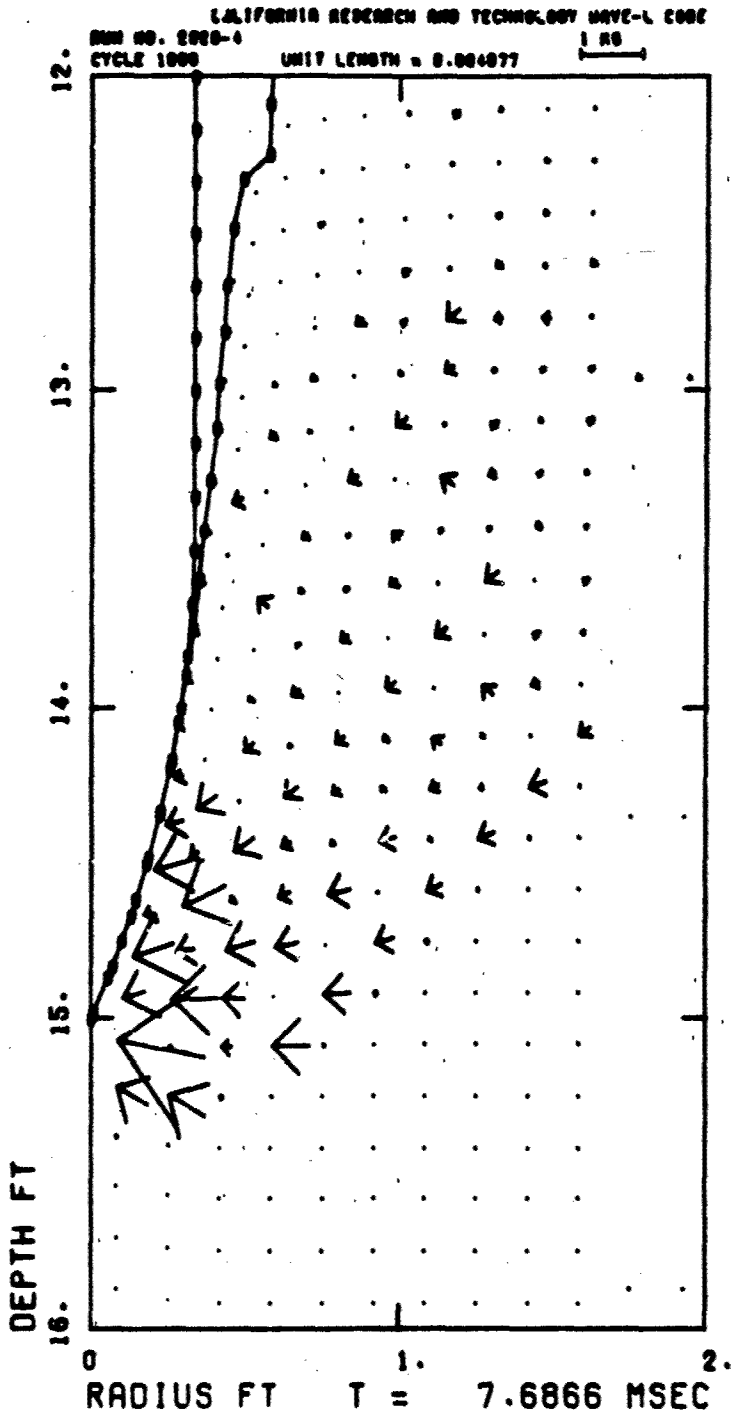

Figure 4-18. Principal Stress Field with Projectile at 15 ft. Depth

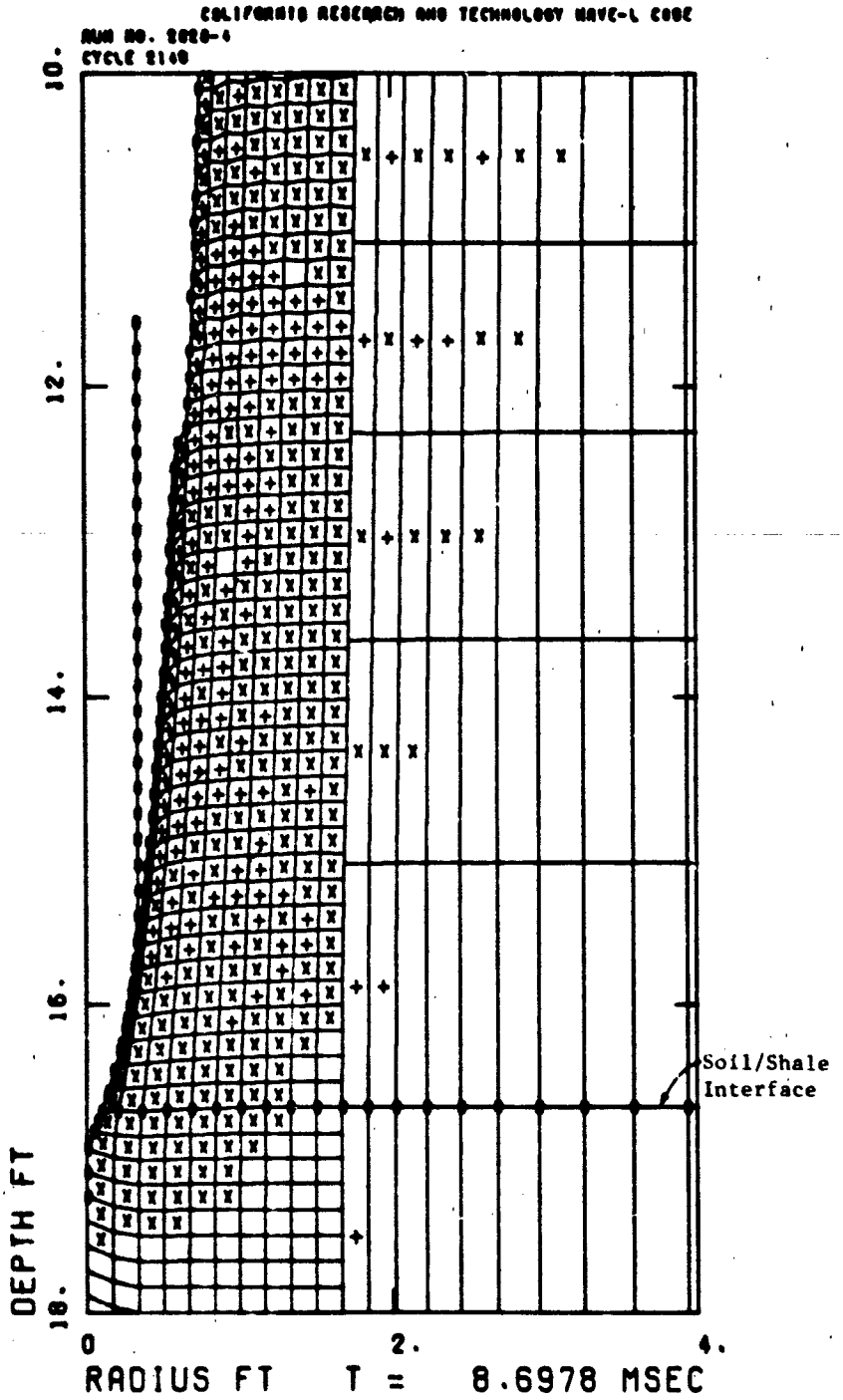

Figure C-10. Grid Configuration with Projectile at 16.9 ft Depth

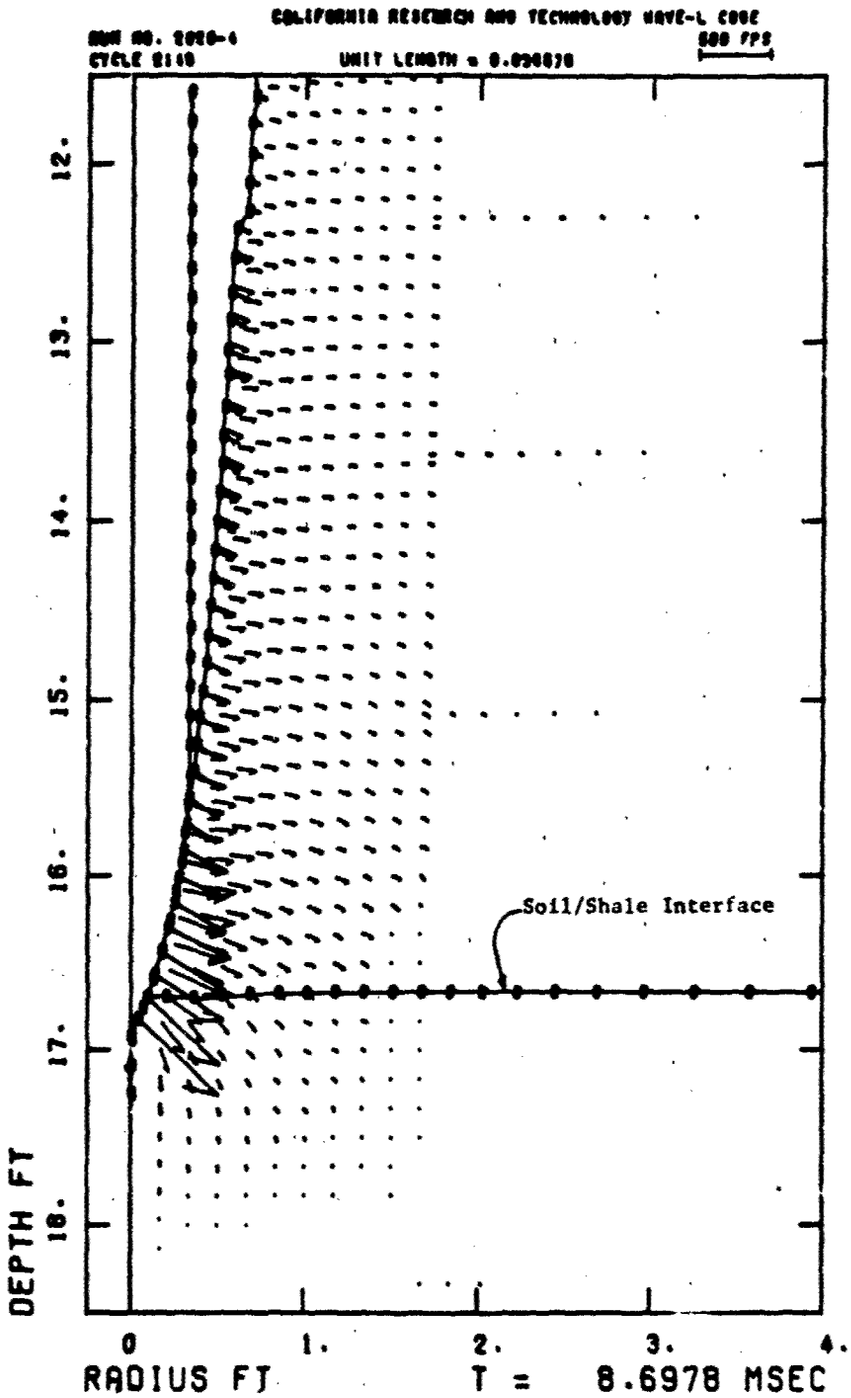

Figure C-20. Particle Velocity Field with Projectile at 16.9 ft Depth

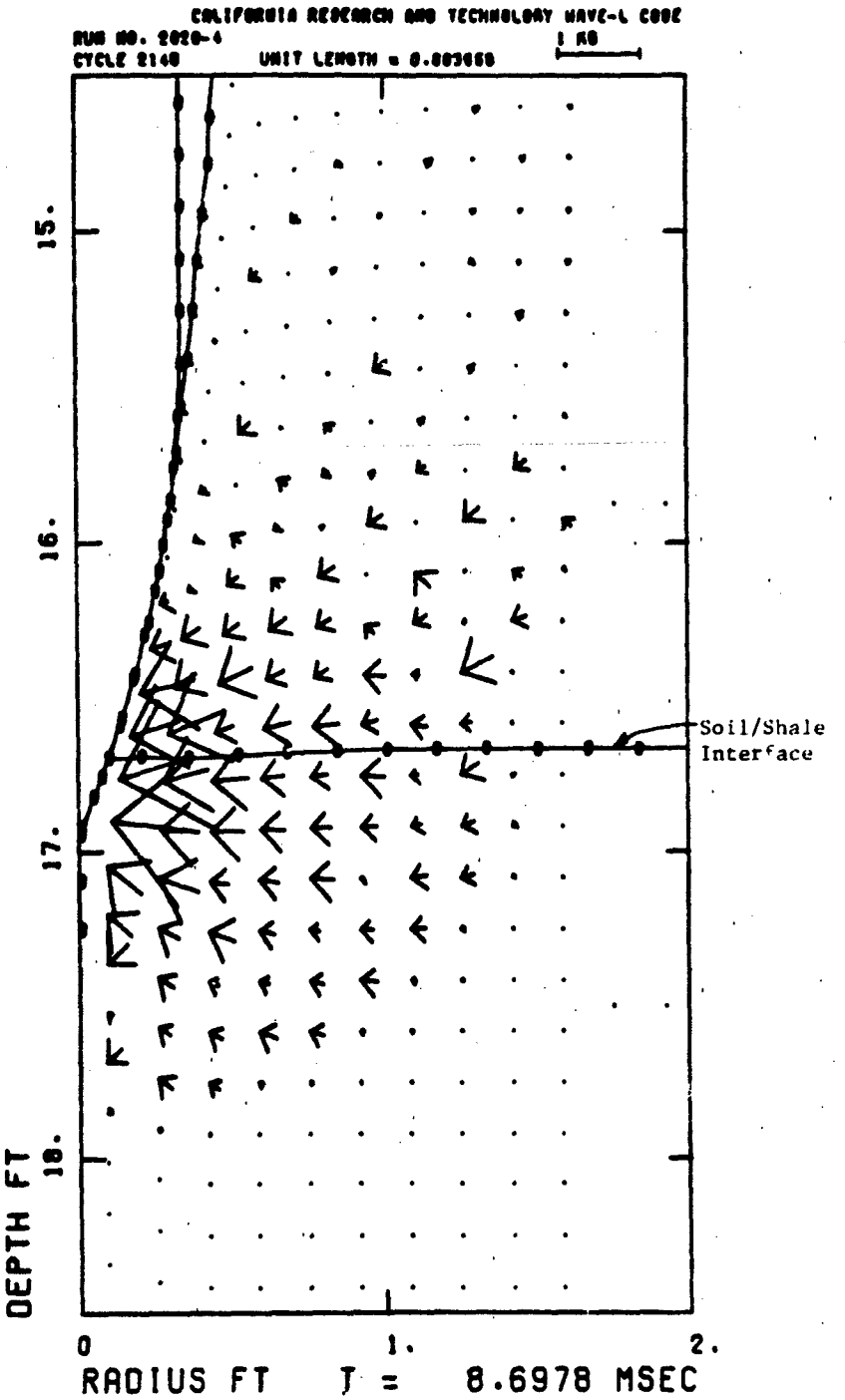

Figure C-21. Principal Stress Field with Projectile at 16.9 ft Depth

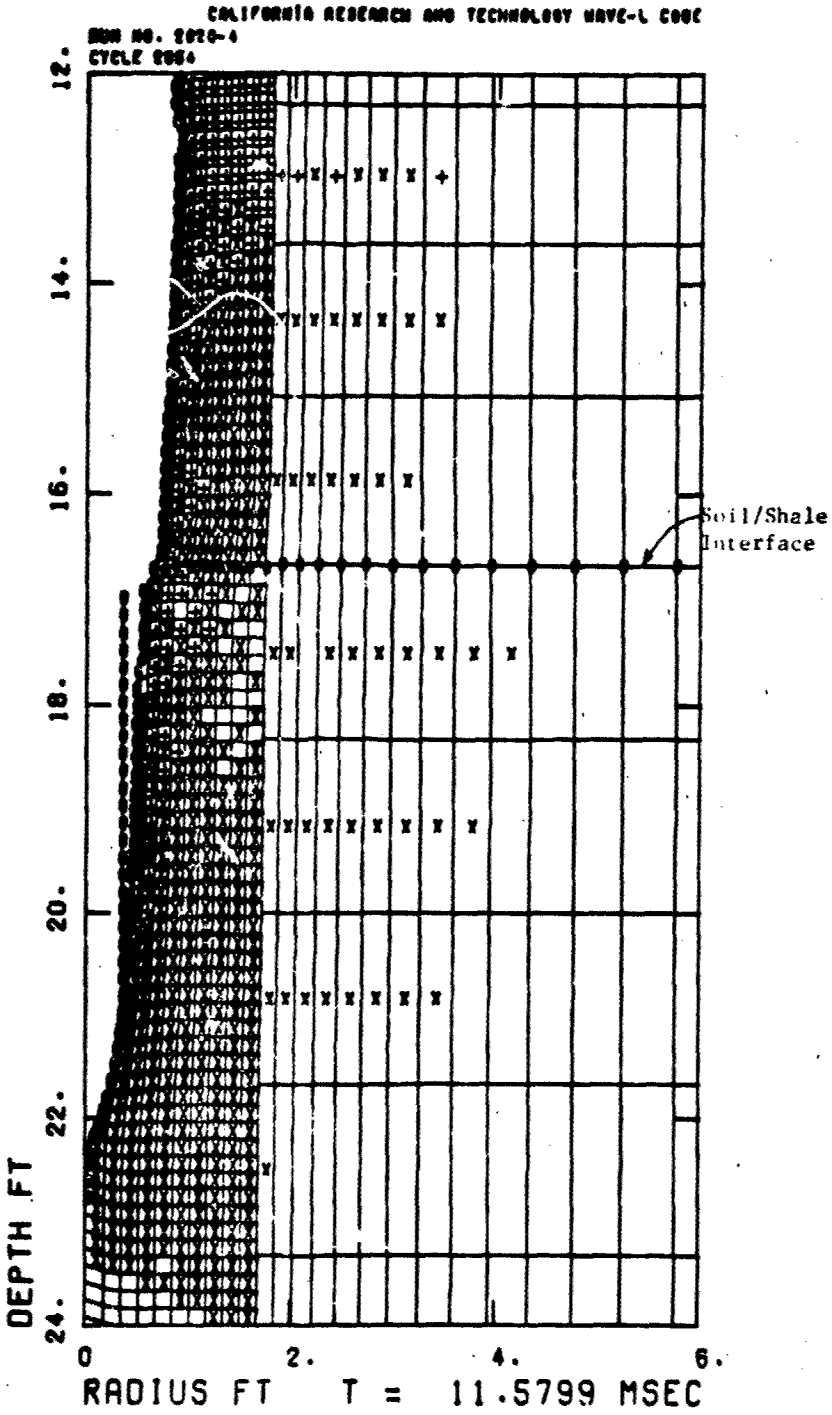

Figure C-22. Grid Configuration at End of Rigid-Body Solution, Projectile at 22.3 ft Depth

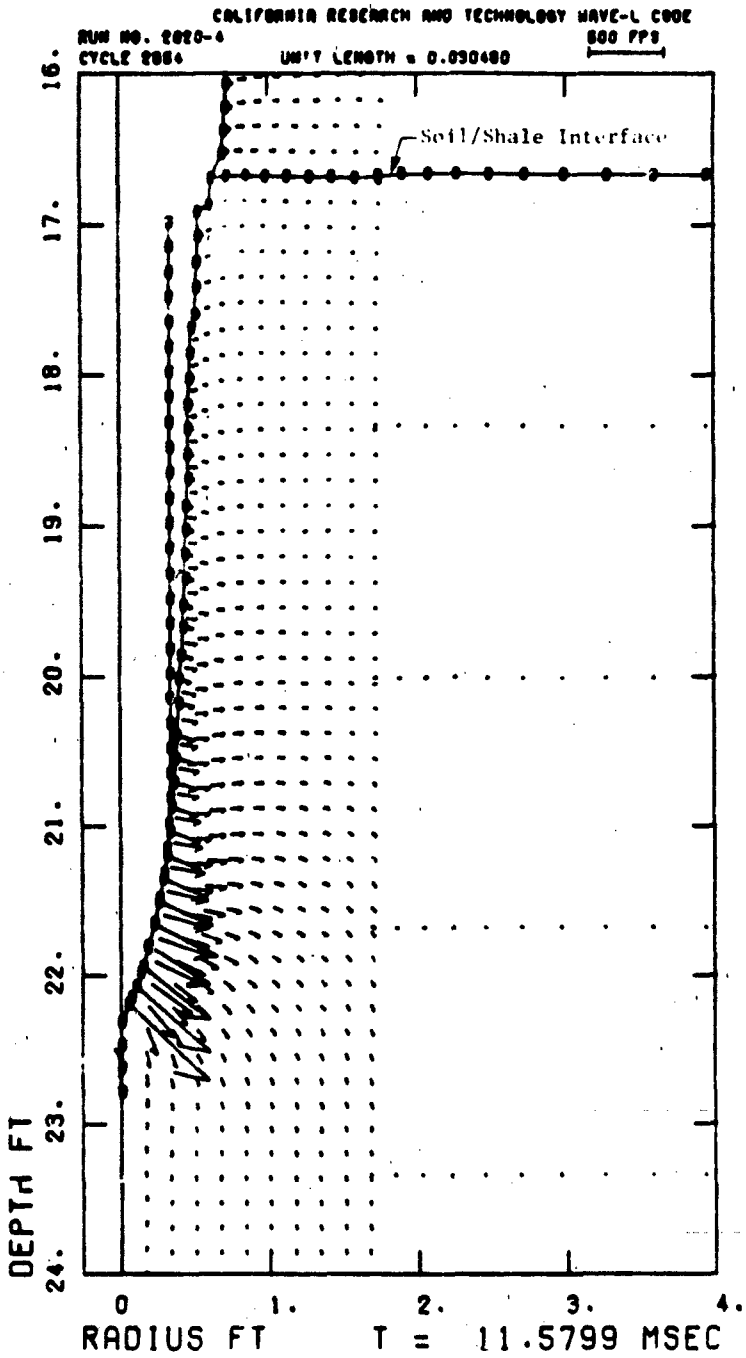

Figure C-23. Particle Velocity Field at End of Rigid-Body Solution, Projectile at 22.3 ft Depth

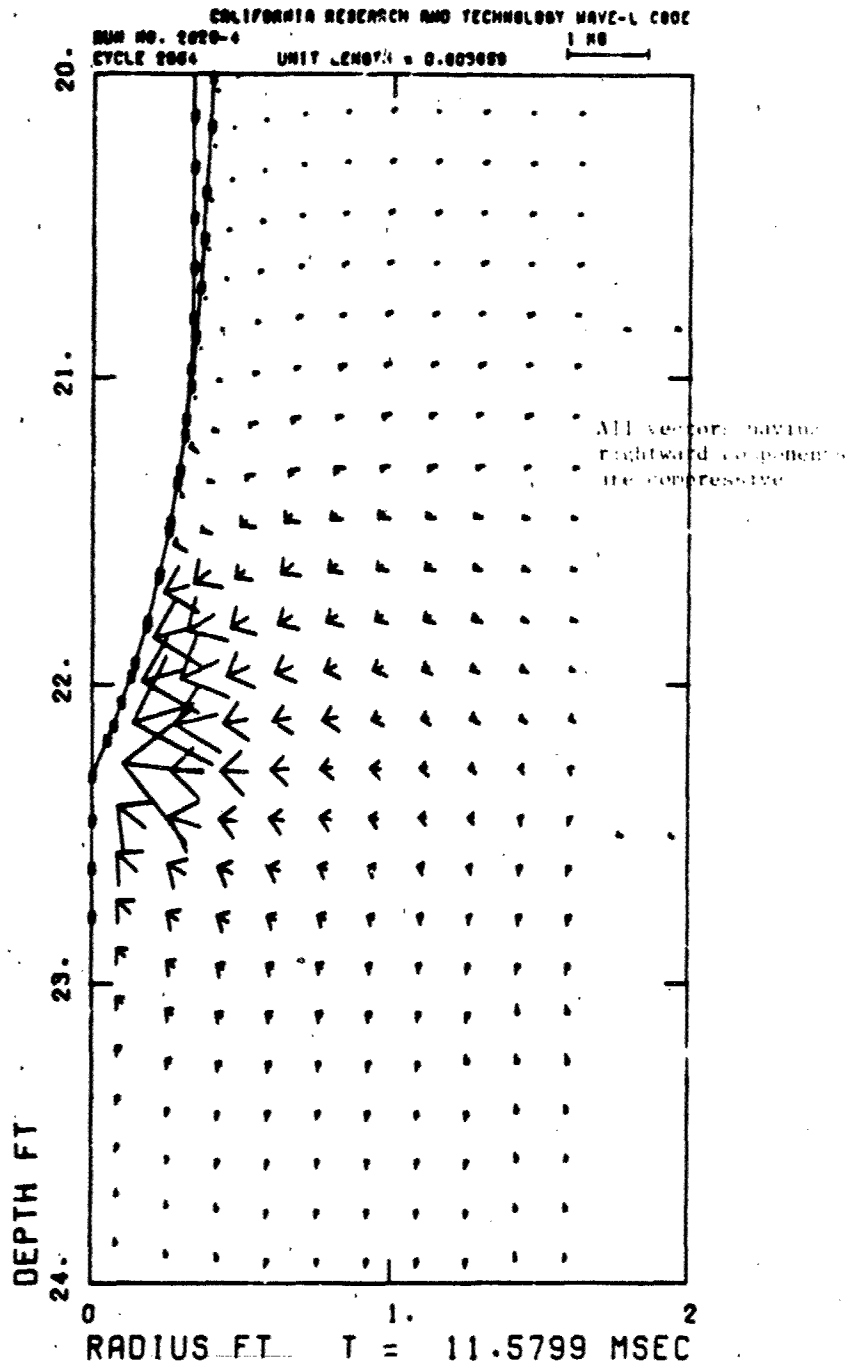

Figure C-24. Principal Stress Field at End of Rigid-Body Solution, Projectile at 22.3 ft Depth

END
DATE
FILMED
10-10-75
NTIS